MODELING THE DURABILITY OF STRUCTURAL COMPONENTS IN AEROSPACE AND MEDICAL INDUSTRIES

by

Sameer Shaik

A dissertation submitted to the faculty of
The University of North Carolina at Charlotte
in partial fulfillment of the requirements
for the degree of Doctor of Philosophy in
Mechanical Engineering

Charlotte

2009

Approved by:

Dr. Kingshuk Bose

Dr. Harish P. Cherukuri

Dr. Shen-En Chen

Dr. David Boyajian

ABSTRACT

SAMEER SHAIK: Modeling the durability of structural components in aerospace and medical industries. (Under the direction of DR. KINGSHUK BOSE)

This dissertation presents applications of the finite element method in studying the durability of components used in aerospace (composites) and medical (hip implants) industries. In the first part of the dissertation the response of a fiber-reinforced composite material, subjected to loads that activate a number of micromechanisms of failure, is investigated in details. A composite material is heterogeneous in nature and generally exhibits local failures before final catastrophic failure at the structural level. The failure mechanisms in this class of materials generally span a number of length scales. Thus, local failure occurs at the micro-level in the form of fiber fracture, fiber buckling, matrix cracking, fiber-matrix debonding, and radial cracks at fiber-matrix interface. At the laminate level, failure occurs in the form of (i) intralaminar cracks in planes parallel and perpendicular to the fiber direction, and (ii) interlaminar cracks between two plies of a laminate; the latter resulting in delamination of the plies. A number of experimental studies aimed at understanding the failure mechanisms under different loading conditions have been reported in the literature. Simultaneously, various analytical and numerical models have also been developed to predict the different failure mechanisms. Such models match experimental data to varying degrees of accuracy. It is generally very difficult to consider all the different failure mechanisms that are observed in experiments, in a single numerical model. This area of research is still in progress. In this study, we focus on simultaneously capturing two major modes of failure that occur in fiber reinforced composites subjected to tensile loading. These are the *splitting* (intralaminar) and the *delamination* (interlaminar) modes of failure, respectively. Experimental observations suggest that these failure mechanisms typically occur in conjunction. The objective of this study is to model these experimental observations using tools available in the commercial finite element code, ABAQUS. Two different failure criteria, following the work by

Hashin and Linde, respectively, are utilized to predict the intralaminar failure mechanisms. The interlaminar failure mechanisms, on the other hand, are modeled using cohesive elements that are based on a traction-separation law used to characterize the constitutive response of the interfaces between the plies. The predictions based on the numerical simulations are compared to experiments and other available data from the literature, and provide useful insights towards the combined modeling of the above-mentioned failure modes.

In the second part of this dissertation an artificial hip implant is investigated from a durability point of view. The advent of artificial hip implants has restored mobility to a lot of patients in recent years, and total hip replacement surgeries are being performed routinely over the past few decades. In 2005 approximately 208,600 surgeries were performed and it is estimated to increase by approximately 174% by 2030. Given such a trend, it is important to ensure that the implant performs as flawlessly as possible, and as closely as possible to the real hip joint. This has led to studies seeking a detailed understanding of the mechanistic and biological aspects of hip implants. In this work, we develop a finite element model of the implant including the femoral ball, and analyze its mechanical response under a single stance phase of gait. The long term durability is investigated based on the computed stresses. In addition, the responses of two-dimensional models are compared to that of a corresponding three-dimensional model, with the aim of determining the applicability of simpler two-dimensional models towards making accurate predictions of the stress and deformation states in the implant. Some other aspects that are also investigated include: (i) the variations of the stress distribution in the implant with femoral ball size, (ii) the nature of the contact interactions between the femoral ball and the implant, and (iii) the influence of the details of the loading and the boundary conditions on the response of the implant. An analytical model is developed to validate the results from the two-dimensional model. The results suggest that the stresses in the neck region of the femoral stem are higher when a smaller sized femoral ball is used. However, the stresses in the region of contact between the ball and the stem appear to be higher for a larger sized femoral ball.

DEDICATION

This dissertation is dedicated to my parents Shaik Abdul Hakeem and Shameem Begum, and brother Shaik Akram Naseer.

ACKNOWLEDGEMENTS

I would like to express my deepest gratitude to my advisor Dr. Kingshuk Bose for his invaluable support, guidance, motivation and time throughout this dissertation. He has helped me develop a good engineering sense of how to approach and solve complex practical problems. His unique teaching style helped me easily understand some of the difficult technical concepts that I came across during my course work and research. It has been an immense pleasure and a great privilege to work with him. I am truly indebted to Dr. Harish P. Cherukuri who was my master's thesis advisor and is a committee member of this dissertation. I would like to thank him for his valuable suggestions in my research, specifically the hip implant project. I am very fortunate to have him as a mentor and a friend throughout my graduate studies at UNC Charlotte. His guidance, support, and encouragement have helped me in all aspects of life. I would also like to thank Dr. Shen-En Chen and Dr. David Boyajian for their willingness to serve as members of this dissertation committee and for their important suggestions in my research. I am thankful to Dr. Jayaraman Raja and Dr. Robin Coger for their valuable advise on my future career.

I am grateful to the Graduate School for awarding me the GASP scholarship that offered full tuition and health insurance coverage during my Ph.D. program. I am thankful to the Department of Mechanical Engineering and Engineering Science for providing me with the necessary financial support throughout my graduate studies. I would like to thank all the faculty and staff members of the department for their kind support and wishes.

I would like to extend my appreciation to my fellow graduate colleagues for their cooperation and help. A special thanks to Sameer Shetty and Sneha Kumar for all their help and moral support, especially during the final stages of this work. I would like to thank Dr. Gautham P. Das and Nawaz Maditheti for the support they have lent me during my graduate studies. I am thankful to all my friends who have wished me well in life.

Most important of all, none of this would have been possible without the inspiration

and blessings from my family members specially my parents and my brother. I am honored to have the support of such a loving family.

TABLE OF CONTENTS

LIST OF FIGURES

LIST OF TABLES

CHAPTER 1: INTRODUCTION

Finite element methods (henceforth abbreviated FEM), also known as finite element analysis (henceforth abbreviated FEA), are currently being used extensively in engineering analysis and design. FEM is useful virtually in every engineering field such as aeronautical, automotive, civil, electrical, and mechanical. While the preceding fields represent the core areas in which FEM was first implemented, over the years FEM has found applications in other branches of science and engineering, such as bio-engineering, fluid mechanics and electromagnetism.

The finite element solution of an engineering problem is essentially the solution to a set of algebraic equations that represent the physical problem [4]. These algebraic equations result from discretization techniques applied to the governing partial differential equations and the associated boundary/initial conditions. The rapid advent of computers have made this method more effective and increased its applicability. FEM originated through the contribution of three separate group of researchers: mathematicians [18], physicists [79] and engineers [3]. Engineers from the civil and aerospace industries [3], [84] and [17] were responsible for the real development of FEM. The term *finite element* was first framed in the paper by Clough [17] in the early 1960's.

Most physical problems can be described by mathematical models by making use of certain idealizations and assumptions regarding the physics. Typically, the governing equations are partial differential equations (henceforth abbreviated PDE). The complete description of the problem also requires a set of boundary/initial conditions to complement the differential equations. The FEM is a numerical procedure that finds an approximate solution to the mathematical model that describes the physical problem. The process involves discretizing (dividing) the geometry into *finite elements* that are connected by points called *nodes*. The solution to the mathematical model is first obtained at each node, and then interpolated within each element. The

method is particularly useful for solving problems of practical interest because classical analytical methods such as the separation of variables cannot be utilized to solve PDE for complicated geometry and boundary/initial conditions, and discontinuous physical properties within the domain. Numerical techniques such as finite difference methods can be used to solve PDE, but are not as versatile as the FEM. Since the FEM provides a solution to the mathematical model only, it is essential to formulate the mathematical model as close as possible to the actual physical problem.

The typical steps of a finite element analysis are shown in Figure 1.1. The first step is the selection of an appropriate mathematical model to represent the physical problem. The mathematical model includes some of the assumptions made with respect to the geometry, material property, loading, and boundary conditions. The next step in the solution process involves making choices regarding the details of the discretization process required to convert the continuous problem to a discrete one. Typical examples include the element type used to discretize the geometry of the model, and, for transient problems, the time integration scheme needed to find the temporal variation of the solution. Typically, the finite element solution would depend on these choices. Once a solution is obtained, it is necessary to verify its accuracy. Generally, this is done by checking whether the solution has converged with respect to the discretization, and can be accomplished by obtaining another solution with a higher number of unknown parameters (more elements and nodes in practical terms). If the two solutions are reasonably close, the solution is said to have converged. Once the desired solution is achieved, the results must be analyzed to determine whether such results represent the solution to the actual physical problem. Based on the conclusions, it may be necessary to reevaluate the mathematical model and make changes to it. In that case, the FEM may be applied to obtain a new set of solutions to the revised mathematical model, and the process of reconstructing the mathematical model, applying the FEM, and interpreting the results may be repeated as many times as needed. It is generally accepted that this process is more cost-effective than the more conventional approach of evaluating designs experimentally through repeated fabrication and testing of parts and products. In particular, it is much easier to carry

out "what if" kinds of studies to evaluate the effects of small changes in design on the performance of the final product. One of the biggest benefits of FEA is its capability to integrate with computer aided design. This gives engineers the added advantage of evaluating the design and the solution to a specific problem through virtual tests involving a strong visual component. FEA provides good assistance to the engineer in identifying potential design faults and in optimizing the design of a structure. Thus, prototype testing in the present era is primarily used in the later stages of a design process, tremendously reducing the design cycle time [25].

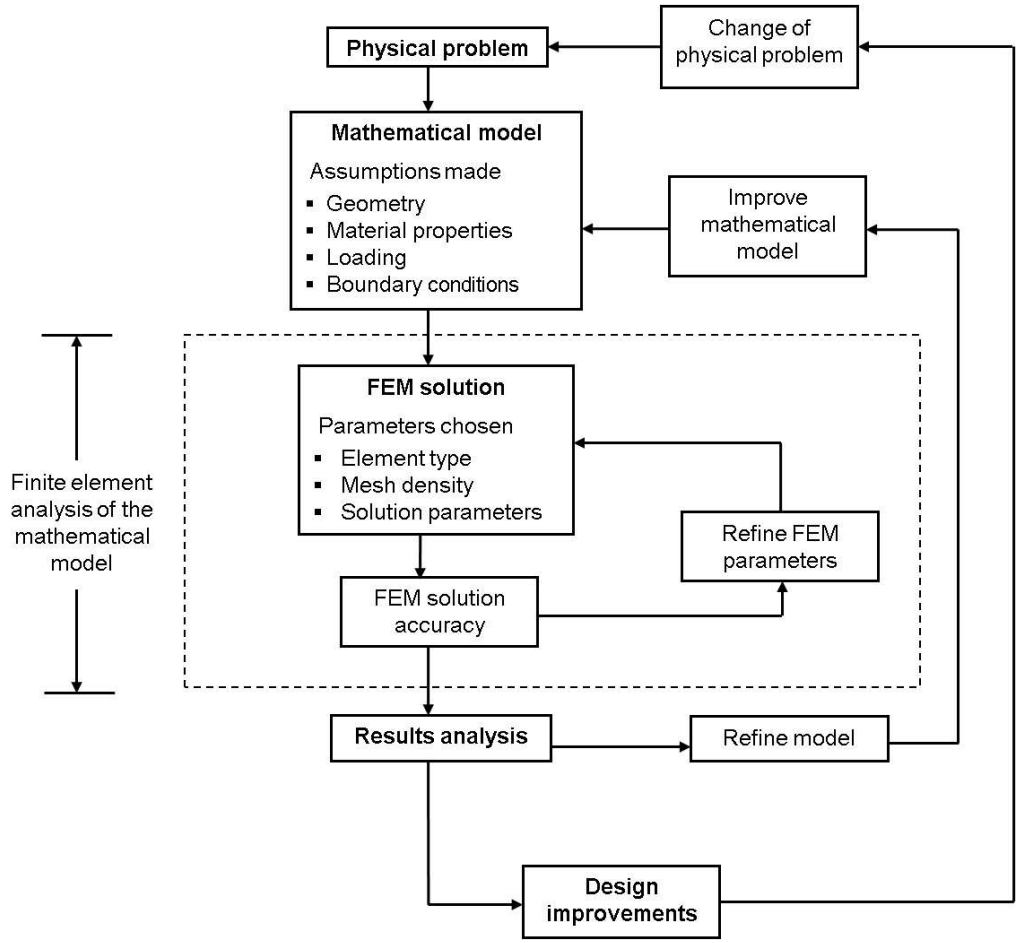

Figure 1.1: Flow chart showing the process of FEA.

This dissertation is an effort to utilize FEA in solving two important design problems with a common theme–*durability*. The first problem is important in the aerospace industry and involves understanding the durability of structural components made

out of fiber reinforced polymer matrix composite materials, that are used extensively for building aircrafts and spacecrafts. The second problem is important in the biomedical industry and involves the evaluation of certain design changes to artificial hip implants, that are heavily used today and will likely see even increased usage in the upcoming years due to an increased desire among elderly people to remain active during the later years of life. These problems will be investigated using the commercial finite element software package, ABAQUS [1].

This dissertation is arranged as follows: Chapters 2 through 6 discuss the modeling of intralaminar and interlaminar damage mechanisms in fiber-reinforced composites, while Chapters 7 through 10 provide details on the study of the durability of artificial hip implants. Specifically, Chapter 2 provides a brief introduction to composite materials, motivates the specific area of study within this broad field, provides some background information on prior research conducted in this area, and points out the objectives for this study. Chapter 3 provides details on the modeling methodology including the geometry, material models, loading, boundary conditions, etc. Chapter 4 contains details of an analysis conducted to evaluate the effectiveness of the discretization used in this modeling effort. Detailed results of the modeling effort are presented in Chapter 5. The conclusions from this investigation along with the scope for future work in this area are discussed in Chapter 6. The second part of the dissertations begins with Chapter 7, which provides an introduction to artificial hip implants. The important assumptions and the FEA modeling approach for the hip implant model are listed in Chapter 8. Chapter 9 discusses the results for the durability of the hip implant. Finally, Chapter 10 lists the conclusions and scope for future work on the prediction of the durability of hip implants.

CHAPTER 2: INTRODUCTION TO COMPOSITE MATERIALS

2.1 Introduction

Fiber-reinforced composites consists primarily of two phases: a "fiber" phase and a "matrix" phase. The fiber phase provides the composite its superior mechanical properties (high strength and stiffness), while the matrix phase serves to hold the fibers together and protect them from environmental effects. When the two phases are combined, chemical reactions and other processing effects often creates an additional phase, known as the "interphase", in the interface region between the fibers and the matrix. Figure 2.1 illustrates the different phases in a composite material. Thus, composite materials are heterogenous in nature. The properties of composites depend upon, among other things, the choice of material for the two phases, the geometry, and the distribution of the phases. An important parameter that determines the

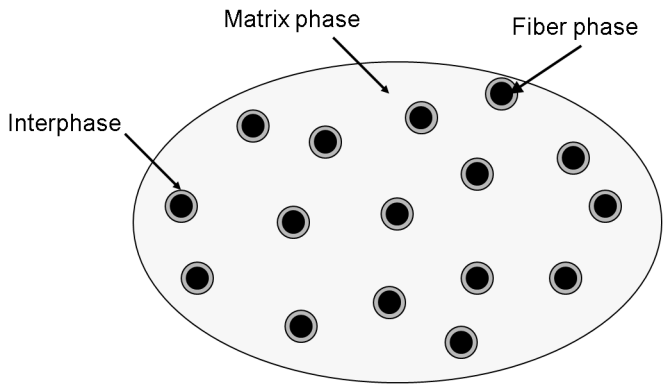

Figure 2.1: Multiple phases in a composite material.

homogeneity or the uniformity of the composite material system is the fiber volume fraction. If the fibers are non-uniformly distributed then the composite material becomes relatively more heterogenous. This increases the probability of failure in the weakest areas. The fiber and matrix materials must be chosen carefully and combined in an appropriate way to form a composite material with desired properties.

The human body is a very good example of nature's utilization of fibrous composites. The muscles and ligaments are oriented in different directions and concentrations to provide a strong, efficient, and versatile body. Some of the other common natural fiber composites include tree barks, wings of a bird, fish fins, and grass. All these structures are characterized by two or more phases in which one acts as a reinforcement to the other phase. Wood is another common composite material that most of us encounter in our daily lives. The use of composite materials can be traced back as early as 4000 B.C. during which the Egyptians used papyrus plants to make writing materials, boat sails and ropes. Biblical references suggest that straw-reinforced clay bricks were used by Egyptians around 1300 B.C. In the early nineteenth century, steel rods were used to provide reinforcement in masonry which lead to the development of steel-reinforced concrete. The first glass fibers were manufactured in 1932 by the Owens Corning Fiberglass Company. These glass fibers were combined with phenolic resin to make reinforced plastic dies for prototype parts in the aerospace industry. Soon fiberglass reinforced phenolic material was being used for other tooling applications in the aerospace industry. In the post-world war era, composite materials were being used in other industries as well. The first fiberglass boat was manufactured in 1940s. The first car with its full body made out of a composite material was introduced in the 1940s as well. Increasing use of composite materials in the aerospace industry lead to the development of the first boron and high strength carbon fibers in the early 1960s. In the early 1970s, metal matrix composites such as boron-aluminum were first introduced. Kelvar was first developed by DuPont in 1971 and soon the applications of composites expanded to sporting and biomedical industries.

Some of the materials commonly used as fibers include glass, carbon, ceramic, and metals. The amount of fibers in a composite can be controlled. This provides the flexibility to build a material with a desired set of properties for a specific application. Composite materials used in structures with a low to medium performance level contain short fibers. These fibers contribute to only local strengthening while the matrix material is the main load bearing constituent. Glass fibers are generally used in such applications due to its high tensile strength and low cost. But glass fibers

have low stiffness, low fatigue endurance, and shows signs of property degradation in severe hygrothermal environments. These factors limit their application in developing composite materials. Kelvar fibers have high stiffness and lower density, but have a low compressive strength. In structures that require a high performance, the entire strength and stiffness is governed by continuously distributed fibers. The matrix only provides support to the fibers. In addition, the matrix phase protects the fibers and also prevents local stress transfer [22] from one fiber to the other. Carbon fibers are being used increasingly in such high performance structures. A wide range of stiffness and strengths can be obtained using this class of fibers. Carbon fibers such as AS4, T300, and C6000 are representative of this category. These carbon fibers are generally manufactured at temperatures between 1200^0C to 1500^0C.

Some of the different types of matrix materials used in composites can be broadly classified as polymers, metals, ceramics, and carbon. The most commonly used matrix materials today are polymers which are further classified into thermosets and thermoplastics. Thermoset materials include epoxies, ploymide, and polyster. Epoxies are used in most composite material applications. Epoxies cured at a lower temperatures (120^0C) are used in structures exposed to low temperature variations (sporting goods), while those cured at a higher temperature (175^0C) are used in components that operate under higher temperature variations (aircrafts). Polyimides are used for higher temperature applications (379^0C). Thermoplastic materials can be used up to a temperature of 400^0C. For higher temperature applications (800^0C or higher), metal matrix materials such as aluminum, magnesium, and titanium alloys are used. For extremely high temperature applications (in excess of 1000^0C), ceramic or carbon matrix materials are used.

Composite materials can be fabricated in different forms, namely: (i) unidirectional lamina, (ii) Woven fabrics, (iii) Laminates, and (iv) hybrid composites. Each of the above-mentioned forms will be briefly discussed in the following.

Unidirectional Lamina: In a unidirectional lamina (also termed as a *ply*), all the fibers are oriented in the same direction as shown in Figure 2.2. The stiffness and the strength of the lamina are greater in the fiber direction compared to the transverse

direction. The lamina thus exhibits macroscopic orthotropic material behavior. In most unidirectional laminae, the effective properties of the ply in the transverse plane (thickness direction) may be isotropic, and such laminae are termed as macroscopically *transversely isotropic*.

Woven fabrics: Composite materials are produced based on techniques, such as

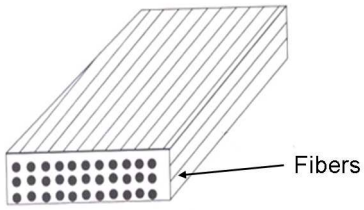

Figure 2.2: A unidirectional lamina (adapted from [34]).

weaving, developed by the textile industry . The fibers are woven into a cloth fabric form and then impregnated in the matrix material. The fabrics can be woven in different patterns. Figure 2.3 shows a plain weave pattern (left) and a five-harness satin weave (right).

Laminates: A stack of laminae is called a *laminate*. Generally, laminae with dif-

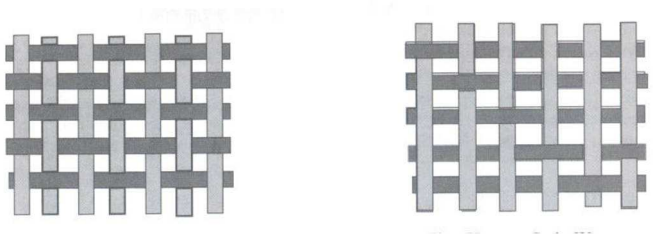

Figure 2.3: Woven fabrics, left - plain weave, and right - five-harness satin weave (adapted from [34]).

ferent fiber orientations are stacked together. Figure 2.4 shows a sequence of 0^0 and 90^0 laminae stacked on top of each other. The fibers in the 0^0 lamina are oriented along the X-axis. The desired effective strength and stiffness of the laminate can be obtained by varying the number of laminae, by varying the thickness of each lamina, and by changing the fiber orientation across the thickness (Z-axis , Figure 2.4). In this dissertation, failure mechanisms in laminates will be studied in detail.

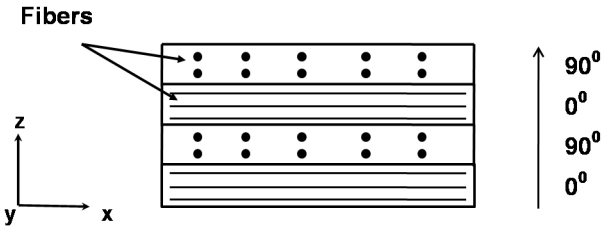

Figure 2.4: A stack of unidirectional laminae.

Hybrid composites: In certain class of composite materials, more than one type of fiber is used. Also, a composite material may be mixed with other materials, such as metals. Such composite materials are referred to as *hybrid composites*. As an example, Kelvar is inexpensive and has good tensile properties but exhibits weak compressive strength. Hence, it can be combined with carbon fibers to achieve the desired compressive strength, resulting in a hybrid composite material [34].

The biggest advantage of a composite material is the high strength and high stiffness compared to other traditional engineering materials such as metals. The strength and the stiffness can also be tailored for a specific application. With availability of different kinds of fiber and matrix materials, one could use any fiber-matrix combination depending on the application and use. Composite materials exhibit better fatigue resistance than metals such as aluminum. Fatigue life is an important property in the aircraft industry: this is one reason why composites outperform traditional aircraft materials such as aluminum. Better fatigue resistance is helpful in other applications such as transportation and bridges. Structural components are also often subjected to thermal stresses, which may lead to failure. Common examples of failures due to thermal effects are: failure by overheating due to friction between moving parts, highway buckle due to thermal expansions, and roof leaks due to thermal expansion and contraction. Therefore, it is desirable to engineer materials with zero coefficient of thermal expansion. By proper design and careful choice of materials, it is possible to manufacture a composite material with zero coefficient of thermal expansion [34]. Most matrix materials such as polymers and ceramics are corrosion resistant to chemicals and moisture. This property is useful in structures such as storage tanks in

chemical industries and offshore drilling platforms. Conductivity is another important property that can be tailored in a composite material depending on the application. Glass/polyster are non-conducting materials, that are commonly used to manufacture ladders to avoid electrocution. Copper-matrix materials are being used in high temperature applications due to the high thermal conductivity of copper. In addition to the above-mentioned advantages composite materials have also turned out to be cost effective during fabrication, leaving behind very little waste. As mentioned previously,

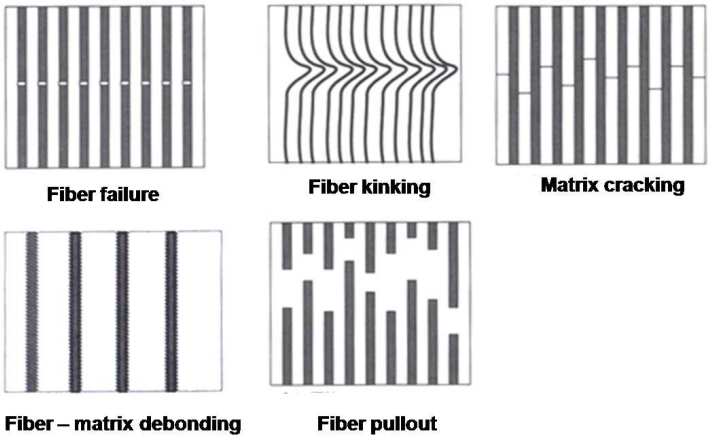

Figure 2.5: Different local failure mechanisms (adapted from [34]).

the applications of composite materials are increasing tremendously in industries such as aerospace, automotive, sports equipment, electronics, medical, and military. With the increasing use of composite materials it is important to understand the different failure mechanisms in order to prevent catastrophic failure of structures made out of such materials. Composite materials generally exhibit local failures (loss of stiffness and strength) before final catastrophic failure at the global structural level. The local failures in general do not necessarily correspond to the final failure. Figure 2.5 shows the different local failures modes that are typically observed in fiber-reinforced composite materials. These local modes typically occur as micro-level mechanisms that include fiber fracture, fiber buckling, fiber splitting, fiber/matrix debonding, matrix cracking, and radial cracks at the fiber/matrix interface. The term *damage* generally refers to one or more of these local failure modes. The process of damage is often considered to be a sequence of steps that begins with *damage initiation*, which

refers to the state in the material at which one or more of the micro-level damage mechanisms become active. With increasing load or time, the local failures may potentially develop further–a phenomenon that is commonly referred to as *damage accumulation/evolution* or *progressive failure* [34]. The final failure occurs due to the progression of potentially a number of different micro-level mechanisms. These micro-level failure mechanisms contribute to failure at the laminate level in the form of in-plane matrix cracks, matrix cracks in the off-axis plies, fiber failures in planes perpendicular to the fibers, and interlaminar failure or delamination.

Figure 2.6 shows some of the failure mechanisms that develop at the laminate level. *Splitting* refers to the case of matrix cracking along the direction of the fibers in the 0° ply (along the loading direction, Figure 2.6, top-left). *Transverse ply cracks* (henceforth abbreviated TPC) are essentially matrix cracks along the direction of the fibers in the off-axis plies i.e.90° ply (transverse to the loading direction, in Figure 2.6, top-right). The separation between two plies in a laminate is referred to as *delamination* (Figure 2.6, bottom). In the context of this study, splitting and TPC failure modes at the laminate level are classified as *intralaminar* failure mechanisms, while the delamination failure mode is referred to as an *interlaminar* failure mechanism.

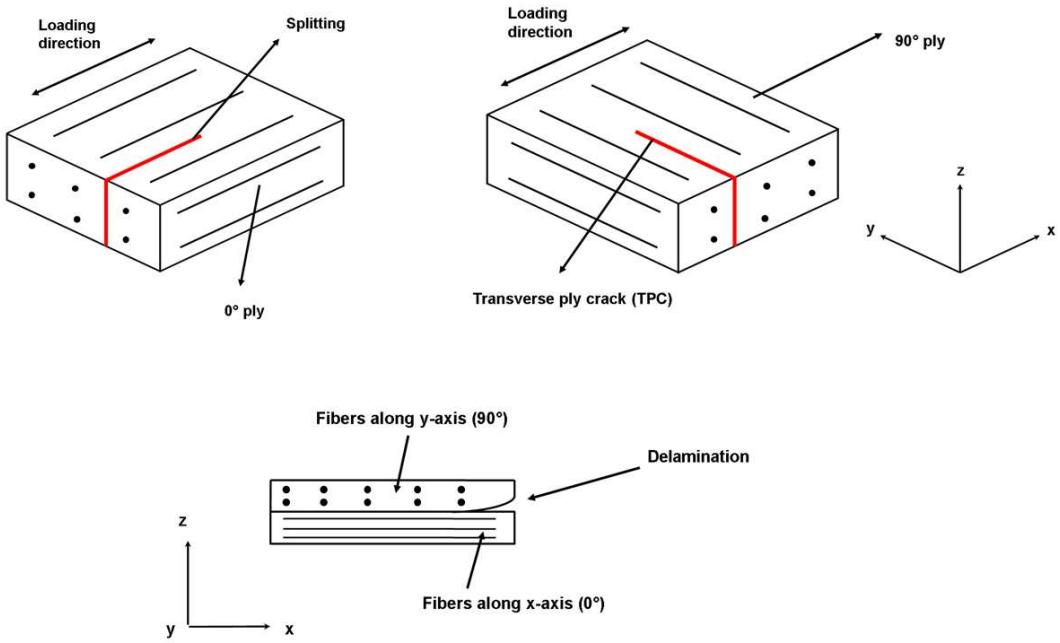

Figure 2.6: Intralaminar and interlaminar failure mechanisms.

In this study, we will focus on modeling the intralaminar and interlaminar damage behavior in carbon/epoxy fiber-reinforced laminated composites. In the following section we provide further motivation for this work.

2.2 Motivation

With the availability of numerous materials, one could use any combination to develop a composite material for their desired needs. But at the same time it is important to perform certain certification tests before these new materials can be used in real life applications. As an example, in the aerospace industry a large airframe requires approximately $\sim 10^4$ tests of the material and components to achieve certification [19]. In a composite material the strength and the stiffness can be altered by changing the orientation, combinations, and path (fibers following curved paths) of the fiber material. The certification system today considers each change in the fiber orientation, combination, or path as a new material. Thus, for each new material the amount of certification tests to be performed is fairly large. Therefore, engineers are limiting themselves to the available set of combinations of materials. Even though an engineer has the resources and capability of developing a new material, he seeks a solution with the existing materials to avoid complex and expensive certification tests. In such situations, virtual experiments can ease some of the complexities in performing the certification experiments.

To use virtual experiments or numerical models to assists in real time experiments, the numerical model must have the capability to accurately predict the failure mechanisms occurring in a composite material. This problem is still an active area of research within the composites community, with a strong focus on validating numerical models to existing experimental results. A common approach is to consider a macroscopic model with sufficient details such that it can validate the experimental results. Such models are generally classified as top-down models [19]. The parameters in the model are refined so that the global compliance of the structure is captured well. In doing so, the micro-level mechanisms must also be predicted correctly. Another approach is to predict the failure mechanisms by modeling the atomic and molecular processes using quantum mechanics and classical molecular dynamics. Such models

are classified as the bottom-up models [19]. A good middle-ground approach would be to model the failure mechanisms using top-down models, and to investigate the mechanisms that need further understanding using bottom-up models.

This study aims to further our understanding of the failure behavior of fiber-reinforced composites, and to model and predict the complex non-linear failure mechanisms accurately. We consider a top-down approach and, wherever possible, validate our results by comparing them with experimental data already available in the literature. In addition to the goal of developing numerical models to assist in reducing some of the experimental complexities, there are a few specific aspects in regards to the modeling of intralaminar and interlaminar failure mechanisms that motivated this study. These aspects will be pointed out in the next section. The following section provides some background information on both the experimental and numerical studies conducted by earlier researchers in order to better understand the intralaminar and interlaminar damage behavior in fiber-reinforced composites.

2.3 Previous Work

In recent years, a number of experimental and numerical studies have been conducted to investigate the damage behavior of composites in the presence of notches, cracks, and other forms of defects. For example, the experimental study by Spearing *et al.* [71] shows three types of damage mechanisms emanating from a notch in a $[90/0]_s$ specimen. These are: (i) splitting in the 0° plies, (ii) transverse ply cracks in the 90° plies, and (iii) delamination at the 90/0 interface. The study was conducted for various ply orientations and also varying specimen dimensions. Splitting was generally observed to occur at an early stage, followed by delamination. The damage in a laminate was assessed using techniques such as radiography, optical microscopy, and scanning electron microscopy. The observations suggest that notch tip damage zone grows in a self-similar manner under tensile cyclic loading. The post-fatigue strength was related to the split length that quantified the extent of damage. Results from our study will be compared to some of the results from this work. The same group of researchers [72] developed a fatigue model for notched laminates. The fatigue model

predicts the extent of damage growth based on prior knowledge of the damage pattern, but it does not predict the path of damage. Spearing and Beaumont [73] also developed a model to predict the post-fatigue strength and stiffness for notched laminates in which damage in the form of splitting, delamination and TPC has grown. This model is based on a finite element representation of the damaged specimen. The finite element representation is a simplified model of the damage mechanisms that were predicted in experiments. This model requires prior knowledge of the damage state in a laminate.

The experimental study by Found *et al.* [26] investigated the damage behavior for two-stage loading: namely, low-to-high and high-to-low fatigue loading condition. This study focused specifically on the longitudinal split behavior and did not investigate any other damage mechanisms. The study suggests that longitudinal splitting is greater for the low-to-high loading condition. The same was observed for both notched and unotched test coupons. Yan *et al.* [92] investigated the tensile strength of graphite/epoxy composites. The effects of clamping composite plates was the main focus of this study. Open hole and filled hole (bolt inserted in the hole of the laminate) test specimens were considered. Uniaxial tension tests were conducted on samples with varying ply orientation and geometries. The specimens were examined by X-ray to access the damage before and after tests. The specimens tested were divided into two groups, Group 1 and Group 2 respectively, based on the damage behavior observed. Fiber-breakage and matrix cracking were the only failure modes observed for Group 1. In Group 2, fiber-matrix splitting and delamination were observed. In Group 2 specimens it was observed that the notch strength improved as the fiber-matrix splits released the stress concentration around the hole. However, an increase in the bolt clamping load suppressed the growth of the fiber-matrix splits, but delamination was still observed to occur. This resulted in a lower notch strength. Their study concluded that fiber-matrix splitting is more important than delamination in determining the increase or decrease of tensile notch strength of laminates with filled holes.

Hashin and Rotem [31] proposed a set of failure criteria for unidirectional fiber

reinforced materials. They were among the first researchers to have carried out a detailed investigation of a cross-ply laminate as a plane stress problem. The assumption made was that if a laminate is symmetric about the mid-plane and subjected to only membrane forces, then the state of stress in the laminate is one of plane stress. Their work considered two modes of failure observed in experiments, namely fiber failure and the matrix failure. The criterion assume quadratic interaction between the tractions acting on the plane of failure. The criterion is expressed in terms of the S-N curves [78]. In 1980, Hashin [32] introduced a set of fiber and matrix failure criteria that distinguish between tension and compression. The aforementioned criteria have been implemented (for general use) within the commercial finite element software package, ABAQUS, to predict the different failure modes in composites, and will be explained in detail in Chapter 3. In more complicated cases, such as specimens with holes, a fully three dimensional stress state needs to be considered. In 1981, Hashin [33] proposed a modified set of failure criteria for composites under a cyclic stress state. The criterion involves quadratic stress polynomials expressed in terms of the transversely isotropic invariants of the cyclic stress tensor. The criterion is developed for the same modes (fiber and matrix failure, respectively) that were considered in the plane stress. The variational approach of Hashin was further developed by Nairn [56], Varna, and Berglund [86] and [87]. A group of aeronautical engineers, Linde *et al.* [49], developed a failure criterion to predict the failure mechanisms in a fiber metal laminate (FML). A strain-based continuum damage formulation is utilized to develop the failure criterion. The failure criterion developed does not explicitly distinguish between tension and compression. The two modes of failure considered in this criterion are the fiber and the matrix failure. This criterion will be utilized in our study and further details on this failure model will be presented in Chapter 3.

Chang *et al.* [15] investigated the tensile failure of open hole laminated composites. An analytical model was developed using a set of failure criteria that incorporated the *in-situ* strengths (explained in Chapter 4) of a ply. Various ply orientations were analyzed. The results from the analytical model showed good agreement with experimental results. This study concluded that the damage mechanisms and the

overall strength of the composite depends heavily on the ply orientation. Tan [66] developed a progressive failure model for laminated composites with open holes using the finite element method. This model considered environmental effects including residual thermal stresses and hygroscopic stresses. The Tsai-Wu criterion [83] is adopted in their study to model the failure behavior of the composite. Two modes of failure were considered: matrix cracking and fiber breakage. Finite element analysis, along with mesh convergence studies, were performed for different ply orientations. The ultimate failure load predicted from the finite element analysis was in good agreement with the experimental data.

The failure criteria used in the study by Chang *et al.* [15] includes the *in-situ* strength of a ply which is not considered in the Hashin's set of criterion [31] and [32]. Also, the criterion used by Chang *et al.* [15] for fiber failure does not distinguish between tension and compression, while Hashin's criteria [32] considers fiber failure in both tension and compression. The work by Tan [66] utilizes the Tsai-Wu criterion which does not distinguish between the different modes of failure in a composite as opposed to Hashin's criteria [31] and [32] .

Tohgo *et al.* [82] developed a criterion specifically for the initiation of splitting crack in unidirectional fiber composites. This criterion is based on mixed mode conditions characterized by the tensile and shear stress intensity factors. Graphite epoxy composite systems were analyzed in this work. The study concluded that the tensile stress intensity factor is responsible for the initiation of the splitting crack. Shahid *et al.* [67] developed a progressive failure model with two constituents: a constitutive model that relates the ply properties with the amount of damage in the laminate, and a damage accumulation model that estimates the accumulated damage in the laminate as a function of the loads. The damage model utilizes Hashin's criteria [32] (proposed in 1980) to predict the matrix cracking, fiber matrix shearing, and the fiber breakage. The ply strengths used in the criteria are assumed to be a function of the crack density (i.e., they are not treated as constants). This model was implemented in a non linear finite element program.

Hashin's 1980 criterion [32] for matrix compression did not consider the in-plane

shear effects that appear to considerably reduce the effective compressive strength of the ply. Sun *et al.* [77] proposed a modification to Hashin's criterion [32] for transverse compression of the matrix. The criterion was modified by adding a term related to shear stresses, that has the effect of increasing the transverse compressive strength. Puck's criterion [62] for matrix in transverse compression is a further improvement to both Hashin's and Sun's criterion. Specifically, Puck introduced the concept of a fracture plane in his proposed criterion. Based on Hashin's criteria and Puck's concept of the fracture plane, Dávila *et al.* [23] developed a new set of phenomenological failure criteria for fiber-reinforced polymer laminates, originally referred to as the LaRC03 set of criteria. The six set of criteria included: matrix failure in compression, matrix failure in tension, fiber failure in tension, fiber failure in compression, fiber kinking, and matrix damage in biaxial compression. The criteria developed for matrix and fiber in compression are based on a Mohr-Coulomb interaction of the stresses associated with the plane of fracture. Pinho *et al.* [61] improved the LaRC03 set of criteria, and denoted the modifications as LaRC04. This set of criteria were developed for both in-plane and three-dimensional stress states, taking into account nonlinear shear effects. The authors claim that LaRC04 criteria seems to provide the best fit to experimental data to date. Maimi *et al.* [53] developed a thermodynamically consistent damage model for fiber-reinforced composites based on the LaRC04 criteria, and utilized the model to computationally predict the failure load of laminates with different ply orientations. This damage law is discussed in details in Chapter 4.

An international exercise known as the world-wide failure exercise (abbreviated as WWFE) [35] was launched in 1995 to establish the status of failure prediction theories for polymer composite laminates. The purpose of this exercise was to provide designers and researchers a detailed qualitative and quantitative assessment of the existing theories that predict failure in composite laminates. A total of 19 different failure theories have been investigated through this exercise. The performance of each of these theories were evaluated by comparing with experimental results, using a process designed by the organisers of this exercise. After a detailed assessment of each of the failure theories, the best five theories [68] are of Zinoviev *et al.*, Bogetti

et al., Puck and Schürmann, Cuntze and Freund, and Tsai *et al.*

The failure theory by Zinoviev *et al.* [96] and [97] is based on the maximum stress failure criterion. A post-failure analysis is also developed in this work. Zinoviev *et al.* assume a linear elastic stress-strain behavior up to the point of initial failure. They also include corrections to the continuously changing fiber orientation in a laminate when loaded monotonically. Bogetti *et al.* [10] and [11] developed a failure theory using the three-dimensional form of the maximum strain failure criterion. On the other hand, Tsai *et al.* [51] and [47] utilized the Tsai-Wu failure criterion which does not distinguish between the different failure mechanisms. They assume a linear elastic material behavior and the stiffness of the material is reduced after the initial failure. The theories of Puck and Schürmann [62] considered a three-dimensional non-linear analysis to predict the progressive failure mechanisms. Cuntze and Freund [20] and [21] use a similar approach as Puck and Schürmann in some regards, but their study assumes interaction between the failure modes due to probabilistic effects. The theories proposed by Puck and Schürmann, and Cuntze and Freund, captured more features of the experimental behavior [68] compared to all the other theories that were investigated in this exercise.

Extensive numerical studies using the finite element method have been carried out with the aim of predicting the damage behavior in fiber reinforced composites; see, for example, [72], [41], [91], [30] and [29], and references therein. The splitting and delamination cracks are often predicted using special purpose elements known as interface elements or cohesive elements. These elements are introduced at locations where splitting and delamination cracks have been observed from experimental studies. Wisnom and Chang [91] developed a finite element approach to model the damage behavior in notched composites. Plane stress elements were used to model each ply and interface elements were used to capture delamination. The same set of interface elements were also used to capture the splitting crack. The interface elements assumed an elastic perfectly-plastic response, with the failure behavior governed by a critical displacement/separation. The model assumes orthotropic material properties for the plies and consider non-linear in-plane shear responses. It is not evident that

ply failure is modeled. The results from this research suggest that both the splitting and delamination failure modes are shear dominated. Therefore, properties related to separation in the normal direction (Mode I like) are not considered for the interface elements. This study also points out that the transverse modulus did not have any effect on splitting and delamination. The results from the numerical study agreed well with the experimental results. Another important conclusion from this study is that splitting drives delamination.The study also highlights the importance of an in-plane non-linear shear response in making accurate predictions. Hallet and Wisnom [29] used a similar finite element based approach, which assumed a strain-based failure criterion for fiber fracture. However, the non-linear shear response is not included in this model. The authors suggest that the choice of a strain-based criteria to predict fiber failure also takes into account the effects of non-linear shear response.

The details of the damage predictions from numerical studies have generally been found to depend on the interface element formulation. The study by Wisnom *et al.* [41] proposed a specific constitutive law to model the cohesive elements. The law accounts for progressive mixed-mode delamination under varying mode ratios during the debonding process. This constitutive law was implemented in the commercial explicit finite element code LS-DYNA [52]. The interface elements were inserted at potential sites of splitting and delamination observed from experiments.

A recent review by Yang and Cox [93] suggests an increasing trend over the last decade to explicitly model the non-linear crack tip process zone. The review also suggests that a cohesive zone formulation seems to be a computationally efficient and good approximation to reality. In their work, a cohesive zone model (henceforth abbreviated CZM) is used to predict delamination as well as splitting. The CZM uses independent cohesive laws for the opening mode and the two shearing modes, and thus accommodates the use of different fracture toughness (area under the traction separation curve) and cohesive strength parameters for the different modes. The cohesive elements were implemented as eight-node user-defined elements in the commercial finite element software package ABAQUS. These elements were placed at locations where delamination and splitting were found to occur from experimental studies [71].

The same cohesive laws are used to predict both splitting and delamination. The shapes of the delamination zones and splitting cracks are found to be consistent with experimental observations [71].

Other recent studies have also focused on developing new approaches to predict the delamination mode of failure. For example, de Borst [12] investigated various discretization techniques to capture discontinuities at the laminate interfaces. Some of the techniques reviewed are: special interface elements, mesh-free methods, finite element methods exploiting the partition of unity property of element shape functions, and discontinuous Galerkin methods. Wells *et al.* [90] present a new model to simulate delamination. The key feature of their study was to uncouple the material structure and the element mesh. The displacement function is separated into a continuous part that describes the continuum response of the model, and a discontinuous part that represents the discontinuities arising from delamination. In the following section, we discuss the objectives for this study.

2.4 Objective

Given the practical importance of this area of research, commercial finite element software packages have also come a long way towards providing their customers with a set of capabilities that effectively model damage and failure in engineering structures. For example, the software package ABAQUS recently implemented a general framework for modeling damage and failure. It includes cohesive elements to model failure at interfaces and a set of capabilities, that are based on the well-known Hashin model [31] and [32], to simulate progressive damage mechanisms in fiber-reinforced composites. We utilize these capabilities in the research presented in this dissertation. Specifically, in this study we attempt to predict the combined effects of matrix splitting and interfacial delamination failure modes in fiber-reinforced composite materials. Cohesive elements are placed at the ply interfaces to predict delamination. However, unlike in some of the earlier studies [41], [91], [30] and [93] we do not introduce cohesive elements at the locations in the matrix where splitting is expected to occur. The broad goal of this study is to simultaneously predict the locations of matrix splitting and delamination, and their effects on the overall load-displacement

response of a structure. We carry out the numerical simulations on a plate with a slit, that is loaded in tension.

CHAPTER 3: MODELING METHODOLOGY

3.1 Geometry and Material Properties

A rectangular specimen with a slit at the center, as shown in Figure 3.1, is considered for this study. The dimensions are chosen such that the length, l, is five times the width, w [71]. Specifically, a specimen having a width of 24 mm and length of 120 mm is chosen [71]. The slit length, $2a$, is assumed to be 8 mm. The slit length is [71] such that the ratio, $w/2a = 3$. The specimen is made out of a carbon/epoxy

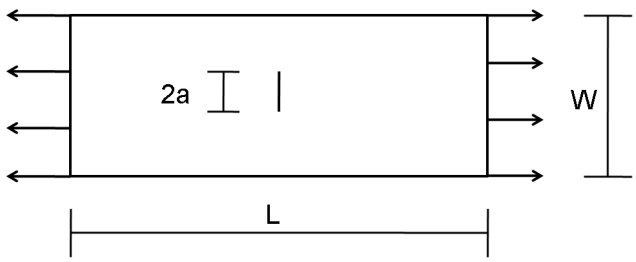

Figure 3.1: Geometry of the laminate.

laminate, with the orthotropic material properties for a single ply tabulated in Table 3.1. A $[90/0]_s$ ply orientation is assumed in this study. Most of the simulations in this study utilize a 1/8th symmetry model, that includes symmetry in the thickness direction. However, in some cases a quarter-symmetry model is also considered.

Table 3.1: Elastic properties of carbon/epoxy (T300/1034-C) laminate.

$E_1(GPa)$	$E_2(GPa)$	$G_{12} = G_{13} = G_{23}(GPa)$	ν_{12}
146.8	11.4	6.1	0.3

3.2 Finite Element Mesh and Boundary Conditions

The mesh for this model is generated within ABAQUS with the node numbers and node locations defined using a separate FORTRAN program. This approach

gives the user complete control of the node and element numbering scheme, which can be very useful while post-processing results either in tabular form or through the visualization module of ABAQUS. Cohesive elements with zero physical thickness (based on nodal coordinates–explained in detail in section 3.4) are placed at the 0/90 interfaces (Figure 3.2).

The continuum shell element will be used in this study to model the plies. Continuum shells have a three-dimensional topology that can be used to directly discretize a three-dimensional body, such that the thickness of the shells is determined by the nodal co-ordinates. This approach is unlike conventional shell elements that have a surface topology representing the mid-surface of the shell, with the kinematics of the element formulation accounting for bending effects in addition to membrane effects. The continuum shell elements have only displacement degrees of freedom unlike the conventional shells that have rotational degrees of freedom in addition to displacements. In a sense, the continuum shell elements are similar to the continuum solid elements in terms of the geometry but their kinematic and constitutive behavior is similar to conventional shell elements. Both 6-node and 8-node continuum shell elements are available within ABAQUS. In this study, the 8-node element (element type SC8R) will be utilized. We will model each ply with a single continuum element along the thickness direction. We will also consider a case in which each ply is modeled using two elements (SC8R) along the thickness direction and compare with the response obtained using a single continuum element (per ply along thickness).

The load is applied through a prescribed displacement field, as shown in Figure 3.3. The direction of the load coincides with the 0° fiber direction or the global X-

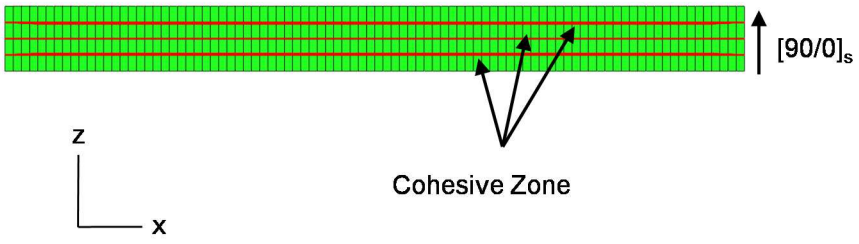

Figure 3.2: Ply orientation and location of cohesive elements.

direction, and the load magnitude corresponds to 1.5% nominal strain. The study by Yang and Cox [93] suggests self similar delamination growth at a nominal strain of about 0.9%. In this study we consider a higher load in order to (i) predict the behavior of the composite beyond the initiation of localized damage, and (ii) possibly get estimates of the final failure.

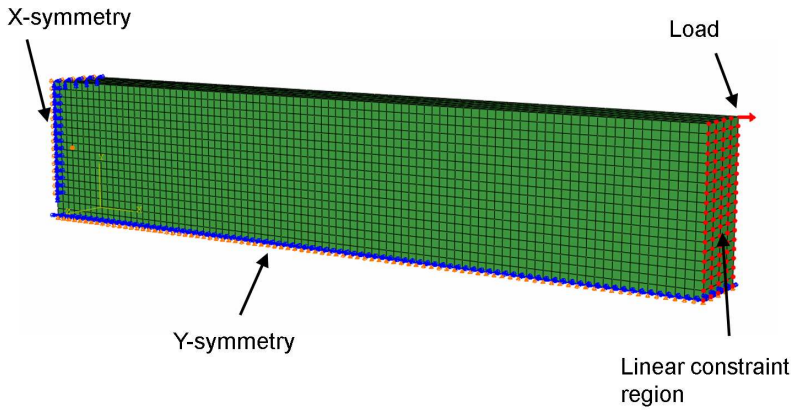

Figure 3.3: Boundary conditions on the model.

Linear constraint equations are used to constrain the nodes on the right face of the structure in Figure 3.3 to a single node. The latter is referred to as the master node, while the nodes that are constrained to move along with the master node are referred to as slave nodes. The displacement boundary condition is applied to the master node, and the reaction force output at this node provides a measure of the load needed to impose the (applied) displacement field over the entire right face.

3.3 Failure Criteria for Intralaminar Damage

In this section, Hashin's failure criteria [32], which is incorporated within ABAQUS, is described in detail. This built-in criteria will be utilized to capture the intralaminar damage behavior of the fiber-reinforced composite specimen discussed in the earlier section. In addition to Hashin's criteria, an alternative set of failure criteria developed by Linde [49] have also been used to model intralaminar failure. Linde's model is not available in ABAQUS as a built-in material model, but is made available through a user material subroutine.

3.3.1 Hashin's criteria

Hashin and Rotem [31] developed a set of fatigue failure criteria for unidirectional fiber reinforced composite materials under a state of plane stress. These criteria take into account four damage mechanisms that are commonly observed in fiber-reinforced composites, namely (i) fiber failure in tension, (ii) fiber failure in compression, (iii) matrix failure in tension, and (iv) matrix failure in compression. These failure mechanisms are assumed to be governed by the following relationships, which also define the *damage initiation criteria* for the respective modes in the context of a progressive damage model [1]:

$$F_f^t = \left(\frac{\hat{\sigma}_{11}}{X_T}\right)^2, (\hat{\sigma}_{11} \geq 0), \tag{3.1}$$

$$F_f^c = \left(\frac{\hat{\sigma}_{11}}{X_C}\right)^2, (\hat{\sigma}_{11} < 0), \tag{3.2}$$

$$F_m^t = \left(\frac{\hat{\sigma}_{22}}{Y_T}\right)^2 + \left(\frac{\hat{\tau}_{12}}{S_L}\right)^2 (\hat{\sigma}_{22} \geq 0), \tag{3.3}$$

$$F_m^c = \left(\frac{\hat{\sigma}_{22}}{2S_T}\right)^2 + \left[\left(\frac{Y_C}{2S_T}\right)^2 - 1\right]\frac{\hat{\sigma}_{22}}{Y_C} + \left(\frac{\hat{\tau}_{12}}{S_L}\right)^2 (\hat{\sigma}_{22} < 0). \tag{3.4}$$

In the equations above, F_f^t, F_f^c, F_m^t,and F_m^c denote the damage initiation criteria corresponding to fiber tension, fiber compression, matrix tension, and matrix compression failure modes, respectively. The quantities X_T, X_C, Y_T, Y_C, S_L, and S_T denote the macroscopic longitudinal tensile strength, longitudinal compressive strength, transverse tensile strength, transverse compressive strength, longitudinal shear strength, and transverse shear strength, respectively, of the composite, and their magnitudes are generally determined by experiments. Typical values for these quantities are tabulated in Table 3.2 [54]. The stress measures $\hat{\sigma_{11}}$, $\hat{\sigma_{22}}$, and $\hat{\tau_{12}}$, that

Table 3.2: Unidirectional strengths of carbon/epoxy (T300/1034-C) laminate.

Longitudinal tensile strength $X_T(MPa)$	Longitudinal compressive strength $X_C(MPa)$	Transverse tensile strength $Y_T(MPa)$	Transverse compressive strength $Y_C(MPa)$	Longitudinal shear strength $S_L = S_T(MPa)$
1730.0	1379.0	66.5	282.2	58.7

appear in the damage initiation criteria, are the components of the so-called *effective stress tensor* [43]. The effective stress tensor, $\hat{\boldsymbol{\sigma}}$, is related to the Cauchy stress tensor, $\boldsymbol{\sigma}$, through the relation [55],

$$\hat{\boldsymbol{\sigma}} = \mathbf{M}\boldsymbol{\sigma}, \tag{3.5}$$

where $\mathbf{M}$ is referred to as the damage operator [55] that takes into account the effects of accumulated damage in the fiber, d_f, that in the matrix, d_m, and accumulated shear damage, d_s, and is given by [1]:

$$\mathbf{M} = \begin{bmatrix} \frac{1}{(1-d_f)} & 0 & 0 \\ 0 & \frac{1}{(1-d_m)} & 0 \\ 0 & 0 & \frac{1}{(1-d_s)} \end{bmatrix} \tag{3.6}$$

The effective stress tensor is identical to the Cauchy stress tensor before damage initiates in any of the modes. However, upon initiation of damage the effective area in the material that offers resistance against deformation reduces, and the effective stress tensor is intended [43] to denote the forces that act on unit damaged area.

The general framework of modeling progressive damage in materials requires the introduction of the concept of *damage evolution* for the different modes of damage. Damage evolution for a certain mode of damage refers to the material response between the initiation of damage and final failure (loss of stress carrying capacity) in that mode. The evolution of damage in the different modes is assumed (in ABAQUS) to be governed by an equivalent stress-displacement relationship, as shown in Figure 3.4. The behavior shown in this figure is to be interpreted as follows. Before damage initiation in any given mode, the material response in that mode is linear elastic (positive slope) up to a critical displacement, δ_{eq}^0, that corresponds to the initiation of damage (Figure 3.4). After the initiation criteria is satisfied, the material stiffness is assumed to be progressively degraded utilizing a linear softening behavior (negative slope) with δ_{eq}^f defining the displacement at complete failure. The post

damage-initiation response of the material has the form [1],

$$\boldsymbol{\sigma} = \mathbb{C}_d \boldsymbol{\varepsilon}, \tag{3.7}$$

where $\mathbb{C}_d$ is the fourth-order damaged elasticity tensor, and ε is the nominal strain tensor. The damaged elasticity tensor is governed by the fiber, matrix and shear damage variables and is given by:

$$\mathbb{C}_d = \frac{1}{D}\begin{bmatrix} (1-d_f)E_1 & (1-d_f)(1-d_m)\nu_{21}E_1 & 0 \\ (1-d_f)(1-d_m)\nu_{12}E_2 & (1-d_m)E_2 & 0 \\ 0 & 0 & (1-d_s)GD \end{bmatrix} \tag{3.8}$$

where $D = 1-(1-d_f)(1-d_m)\nu_{12}\nu_{21}$, d_f is the current state of the accumulated damage in the fibers, d_m is the current state of accumulated damage in the matrix, and d_s is the current state of accumulated shear damage, and E_1, E_2, ν_{12} , ν_{21} and G are the elastic properties as defined in Table 3.1.

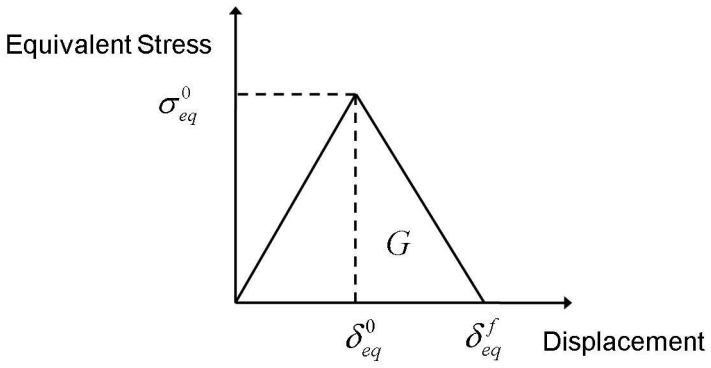

Figure 3.4: Damage evolution law for carbon-epoxy laminate.

The damage evolution is governed by so-called fracture energies, which refers to the area under the stress (effective) - displacement curve for each mode. Thus, the critical equivalent displacement at failure (discussed above) for each mode can be computed based on the fracture energy for that mode. The fracture energies for the different modes [54] are tabulated in Table 3.3.

Table 3.3: Fracture toughness of carbon/epoxy (T300/1034-C) laminate.

Longitudinal tensile fracture energy $G_{1+}(N/mm)$	Longitudinal compressive fracture energy $G_{1-}(N/mm)$	Transverse tensile fracture energy $G_{2+}(N/mm)$	Transverse compressive fracture energy $G_{2-}(N/mm)$
89.8	78.2	0.23	0.76

3.3.2 Linde's model

Linde *et al.* [49] proposed a model to predict the damage behavior of fiber metal laminates (FML). FML consists of alternate layers of aluminum and glass fiber reinforced epoxy. This material is being used increasingly in modern aircraft fuselage designs. Damage in the aluminum and the glass/epoxy layers are due to different mechanisms and therefore, the materials are modeled separately. The material model of interest in this study is that utilized by the above authors to capture the failure behavior of the glass/epoxy layer.

The failure criteria is developed on the basis of a strain based continuum damage formulation. There is no explicit distinction between the damage behavior in tension or compression. Therefore, only two damage variables are assumed corresponding to damage in the matrix and the fiber, respectively, unlike the four variables in Hashin's criteria. An exponential degradation of the material properties is assumed in this model. The initiation of damage in the fiber governed by [49]:

$$f_f = \sqrt{\frac{\epsilon_{11}^T}{\epsilon_{11}^C}(\epsilon_{11})^2 + \left(\epsilon_{11}^T - \frac{(\epsilon_{11}^T)^2}{{\epsilon_{11}}^C}\right)\epsilon_{11}} > \epsilon_{11}^T \tag{3.9}$$

where ϵ_{11}^T is the fiber failure strain in tension, and ϵ_{11}^C is the failure strain in compression. The failure strains are computed based on the known failure stress data (Table 3.2) using the relationship,

$$\epsilon_{11}^T = \frac{X_T}{C_{11}} \tag{3.10}$$

$$\epsilon_{11}^C = \frac{X_C}{C_{11}} \tag{3.11}$$

where X_T and X_C are the longitudinal tensile and compressive strengths, respectively,

and C_{11} is the component of the undamaged elasticity matrix. Once the above criterion (Equation3.9) is satisfied, progressive damage begins with evolution governed by:

$$d_f = 1 - \frac{\epsilon_{11}^T}{f_f} e^{(-C_{11}\epsilon_{11}^T(f_f - \epsilon_{11}^T)L^c/G_f)} \tag{3.12}$$

where d_f is the fiber damage variable, L^c represents a characteristic element length, and G_f is the fiber fracture energy.

The damage in the matrix is initiated based on the following relationship,

$$f_m = \sqrt{\frac{{\epsilon_{22}}^T}{{\epsilon_{22}}^C}(\epsilon_{22})^2 + \left({\epsilon_{22}}^T - \frac{(\epsilon_{22}^T)^2}{{\epsilon_{22}}^C}\right)\epsilon_{22} + \left(\frac{\epsilon_{22}^T}{\epsilon_{12}^S}\right)(\epsilon_{12})^2} > \epsilon_{22}^T \tag{3.13}$$

where ϵ_{22}^T is the transverse failure strain in tension, ϵ_{22}^C is the transverse failure strain in compression, and ϵ_{12}^S is the shear failure strain. The threshold values for the transverse strains are given by:

$$\epsilon_{22}^T = \frac{Y_T}{C_{22}} \tag{3.14}$$

$$\epsilon_{22}^C = \frac{Y_C}{C_{22}} \tag{3.15}$$

$$\epsilon_{12}^S = \frac{S_L}{C_{44}} \tag{3.16}$$

where Y_T and Y_C are the tensile transverse and compressive strengths, respectively, S_L is the longitudinal shear strength, and C_{22} and C_{44} are the components of the undamaged elasticity matrix. The evolution of matrix damage is governed by the relation,

$$d_m = 1 - \frac{\epsilon_{22}^T}{f_m} e^{(-C_{22}\epsilon_{22}^T(f_m - \epsilon_{22}^T)L^c/G_m)} \tag{3.17}$$

where d_m is the matrix damage variable and G_m is the matrix fracture energy.

In this study, the results based on the exponential damage evolution law from Linde's model will be compared to those obtained using the linear softening law discussed earlier in the context of Hashin's model. Linde's model couples the tensile and compressive behavior of the fiber and the matrix in a single relationship, given by Equation 3.9 and 3.13, respectively. To understand this further, the governing

equation for fiber initiation (Equation 3.9) is analyzed. By performing basic algebraic operations on Equation 3.9, it is found that this equation is essentially a quadratic equation in terms of ϵ_{11}. The two roots of this equation are the longitudinal tensile failure strain, ϵ_{11}^T, and the longitudinal compressive failure strain, ϵ_{11}^C. Likewise, in the absence of the shear term, the matrix initiation equation is basically a quadratic equation in terms of ϵ_{22}. Here the two roots are the transverse tensile failure strain, ϵ_{22}^T, and the transverse compressive failure strain, ϵ_{22}^C. Hence, we conclude that the Linde's model reduces to failure under a critical applied strain in the limiting cases of pure tension and pure compression in the fiber- and the transverse direction, respectively.

3.4 Cohesive Elements

This section describes the methodology used to capture the interlaminar damage behavior utilizing cohesive elements. The following sections provide some information on the background and the formulation of cohesive elements.

3.4.1 Introduction

Cohesive elements are used to model fracture across adhesively bonded interfaces. These elements are based on the concepts of cohesive zones introduced by Dugdale [24] and Barenblatt [5]. The cohesive zone modeling approach has become a powerful tool in simulating nonlinear fracture processes. In recent years, cohesive elements have been used to model delamination or interlaminar damage in composite materials. The cohesive elements provided by ABAQUS will be utilized in this study to model the interlaminar damage behavior.

In ABAQUS [1], the mechanical response of cohesive elements may be defined based on (i) a continuum approach, (ii) a traction-separation approach, and (iii) a uniaxial stress state approach. Each of the above mentioned classifications are useful for certain type of applications. In situations where two bodies are connected by an adhesive material with a finite thickness, the continuum based modeling approach is more appropriate. Built-in conventional material models or user-defined material models can be used to define the continuum response of the cohesive elements. In the case of bonded laminated composite materials, the interface material between the laminates is very thin and can be essentially considered to be of zero thickness. In

such cases, the traction-separation modeling approach is more appropriate, and this is the approach used in the present work. The traction-separation approach will be discussed in somewhat more details later in this section. The uniaxial stress state based approach is meant for modeling gaskets, where the gaskets are assumed to be under a uniaxial stress state. Also, this approach can be utilized to model adhesives that are assumed to be relatively unconstrained in the lateral direction.

3.4.2 Representation of a cohesive element

A schematic of a 4-node two-dimensional cohesive element and a 8-node three-dimensional cohesive element are shown in Figure 3.5, left and right, respectively. The response of a cohesive element is characterized by the relative motion of the

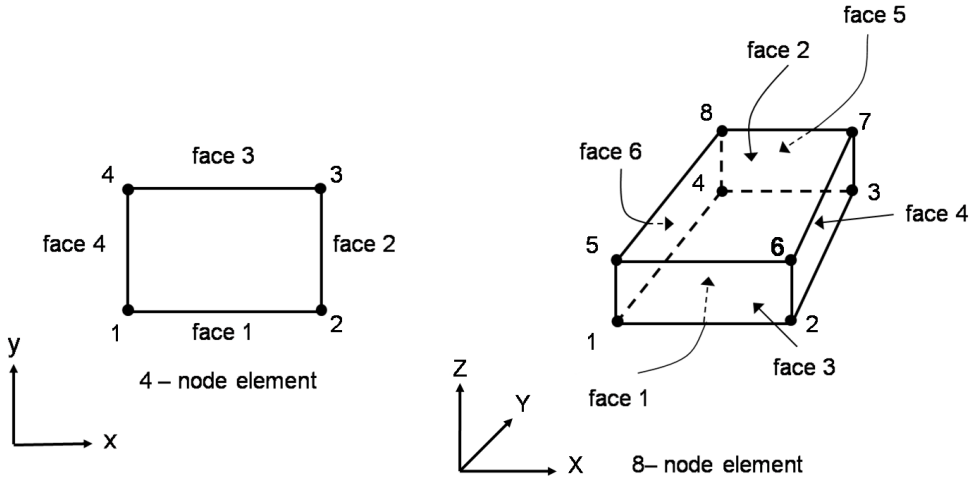

Figure 3.5: Two-dimensional cohesive element (left) and a three-dimensional cohesive element (right), [1].

bottom surface and the top surface measured with respect to the thickness direction (local Z-direction for the three-dimensional element and local Y-direction for the two-dimensional element, as shown in Figure 3.5) and two-other orthogonal directions. For a two-dimensional element the bottom surface is defined by face 1 between nodes 1 & 2, and the top surface is defined by face 3 between nodes 3 & 4 (Figure 3.5 left). Similarly, for a three-dimensional element, the bottom surface is defined by face 1 between nodes 1, 2, 3 & 4, and the top surface is defined by face 2 between nodes 5, 6, 7, & 8. The separation between the bottom surface and the top surface in the

thickness direction denotes the opening or closing of the interface. In this study, the three-dimensional cohesive element will be utilized.

3.4.3 Traction-separation response of cohesive elements

The traction-separation approach is mainly used to model adhesive interfaces in situations where the thickness of the adhesive is negligible. The cohesive element is formulated in such a way that it allows the user to define zero geometric thickness (i.e., the top and bottom surfaces are identically at the same spatial location initially). This unique feature of the element is accommodated within the traction-separation approach by formulating the constitutive response directly in terms of the traction versus separation (as opposed to stress versus strain).

The traction-separation approach is broadly classified into two groups [6], namely (i) reversible models that consider the traction components as derivatives of a potential function, and (ii) irreversible models in which progressive damage beings once the initiation criteria are satisfied. The reversible models assume that the response of the cohesive zone is reversible until final failure has occurred. In the irreversible models, the cohesive response is irreversible once damage has initiated. A traction-separation law that is based on the later approach will be considered in this study.

In particular, a bilinear traction-separation law, shown in Figure 3.6, is considered for this study. The law is assumed to be linear elastic prior to damage initiation. The elastic behavior is defined in terms of an elasticity matrix that relates the nominal stresses to the nominal strains. The nominal strains are the separations between the top and the bottom surface of the element divided by the original *constitutive thickness* of the element. The constitutive thickness may, in general, be different from the geometric thickness of the element defined in terms of nodal coordinates of the top and bottom faces. In particular, for the case of an element with zero geometric thickness, a default constitutive thickness of 1.0 is assumed such that the magnitude of separation is equal to the magnitude of the corresponding nominal strain. In this study, we define zero geometric-thickness cohesive element at the interfaces between the different plies. The nominal stresses are defined to be the forces divided by the area at each integration point. In Figure 3.6, the quantities

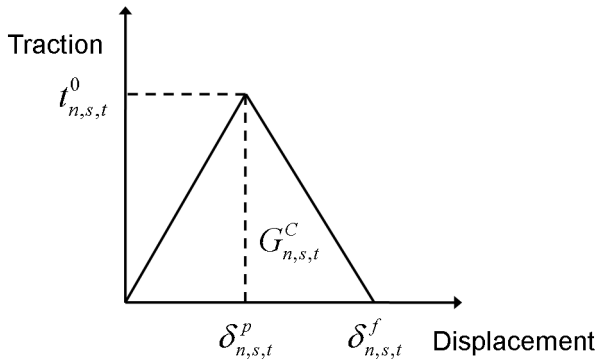

Figure 3.6: A typical bilinear traction-separation law.

t_n^0, t_s^0, and t_t^0 represent the peak traction in the normal, first shear, and second shear direction, respectively. These are the appropriate components of the nominal traction vector in three-dimensional problems. In two-dimensional problems, the second shear component t_t^0 is not considered. The quantities δ_n^p, δ_s^p, and δ_t^p represent the equivalent displacements at damage initiation, while the quantities δ_n^f, δ_s^f, and δ_t^f represent the equivalent displacements at failure in the normal, first, and second shear directions, respectively. These displacements are essentially the appropriate components of the nominal strain.

The linear elastic constitutive relationship between the nominal stress and nominal strain before the initiation of damage is given by:

$$t = \mathbf{K}\epsilon \tag{3.18}$$

where t is the nominal stress vector, ϵ is the nominal strain vector and $\mathbf{K}$ is the elasticity matrix. In this study, an uncoupled behavior between the normal and shear components is assumed. Thus, the off-diagonal terms in the elasticity matrix are set to zero and only the diagonal terms are assumed to be nonzero. The damage initiation of the cohesive elements is defined by a quadratic nominal stress criterion, and is given by:

$$\left(\frac{\langle t_n \rangle}{t_n^0}\right)^2 + \left(\frac{t_s}{t_s^0}\right)^2 + \left(\frac{t_t}{t_t^0}\right)^2 = 1. \tag{3.19}$$

The initiation begins once the sum of the traction ratios in the above Equation 3.19

reaches a value of 1.0.

Once the initiation criteria is satisfied, the stiffness of the element is progressively degraded using a linear softening law as shown in Figure 3.6. The damage evolution law is based on the energies dissipated during the damage process at the interface. It is governed by fracture energies in the pure normal and the two shear modes, quantified by G_n^C, G_s^C, and G_t^C, respectively. The mixed mode behavior is assumed to be governed by a power law, given by:

$$\left(\frac{G_n}{G_n^C}\right)^\alpha + \left(\frac{G_s}{G_s^C}\right)^\alpha + \left(\frac{G_t}{G_t^C}\right)^\alpha = 1, \tag{3.20}$$

where G_n, G_s, and G_t are the energies dissipated in the normal, first shear, and second shear directions, respectively. The power α is assumed to be 1.0 [89] and [38]. In this study, the fracture energies for both the shear modes are assumed to be the same [93]. The peak strengths of the cohesive region and the critical fracture energies [93] are tabulated in Table 3.4.

Table 3.4: Cohesive zone properties.

Modes	Toughness (N/mm)	Peak Strength (MPa)
Mode I - G_n^C	0.35	50.0
Mode II - G_s^C	0.7	30.0
Mode III - G_t^C	0.7	30.0

3.5 Viscous Stabilization

Non-linear static problems can lead to local instabilities such as local buckling and material instability. Material instability is typically a result of material softening and stiffness degradation. Such instabilities may lead to convergence problems in an implicit finite element solution scheme. The implementation of the progressive damage of cohesive elements in ABAQUS accommodates a form of viscous regularization or automatic stabilization that helps with such convergence issues. In particular, the method of viscous regularization ensures that the tangent stiffness matrix remains positive for small time increments during the material softening process.

The viscous regularization algorithm utilizes a modified viscous damage variable, defined by: [1],

$$\dot{d_v} = \frac{1}{\eta}(d - d_v) \tag{3.21}$$

where $\dot{d_v}$ defines the evolution of the modified damage variable, η is the viscous regularization coefficient, and d is the original damage variable without considering viscous effects. If viscous regularization is included in a model, the tangent stiffness of the damaged interfacial response will be a function of the viscous damage variables. The viscous coefficient is selected by the user and is typically much smaller than the characteristic time increment for the problem before damage initiates. The inclusion of viscous regularization leads to an increase in the apparent fracture energy of the interface and results in better convergence characteristics in the presence of material softening.

The damage modeling framework using Hashin's criteria allows for four damage variables, with a viscosity coefficient associated with each damage variable. For Linde's model, a single viscous coefficient is utilized for both fiber and matrix damage variables. A similar approach for viscous regularization is also utilized in the cohesive zone model.

CHAPTER 4: VALIDATION OF MESH SIZE

In this chapter we investigate a carbon fiber-reinforced polymer (abbreviated as CFRP) plate with a hole at the center that is loaded in tension. Only intralaminar damage mechanisms are considered for this part of the study–i.e., delamination across plies is neglected for the time being. The main objective of this part of the investigation is the determination of appropriate mesh size and other modeling constructs that are needed for an accurate prediction of intralaminar damage mechanisms. To this end, the results of the present simulation are compared with both experimental and numerical results that are available in the literature for this problem. The information gathered through this study will be utilized in the next part of this dissertation to model both intralaminar and interlaminar damage mechanisms in a CFRP plate with a center slit that is loaded in tension.

4.1 Introduction

The mechanisms that lead to failure in composite materials are very complex, and some mechanisms such as matrix and fiber compression are still not clearly understood. Existing numerical models [31], [23], [96], [62] and [51] are being evaluated continuously, and new models are being proposed and developed to capture these complex failure mechanisms accurately. As discussed in the last chapter, final catastrophic failure in a composite material is typically preceded by progressive damage mechanisms governed by so-called fracture energies associated with the different failure mechanisms. Therefore, it is essential to use failure criteria that not only predicts the onset or the initiation of damage, but also captures the evolution of damage. This would in turn increase the likelihood of a more accurate prediction of the response at the structural level, particularly the peak in the global load-displacement behavior.

The damage behavior in the composite is modeled across multiple length scales. At the micro-scale, the individual damage mechanisms at the fiber and matrix levels

determine the behavior at the meso-scale, which is measured by the response of a single ply or a number of plies. The latter in turn determines the structural response at the macro-scale. A good measure of the accuracy of the modeling paradigms at the different length scales is the level of agreement of the global load-displacement response and the final failure load with available experimental data. The purpose of the study presented in this chapter is to ensure that the mesh size, element type, and failure criteria used to predict the intralaminar damage behavior provides reasonable estimates of the final failure load and displacement.

Camanho *et al.* [54] (henceforth referred to as C07) have proposed a continuum damage model that is used to predict the onset and propagation of intralaminar failure mechanisms. These mechanisms include matrix cracking and fiber fractures. This damage model predicts the failure mechanisms using the LaRC failure criteria developed by Dávila *et al.* [23]. The predictions of the damage model are compared to experimental data for a CFRP specimen with an open hole that is loaded in tension. In the present study, the Hashin model and the Linde model (both discussed in the last chapter) will each be used to predict the response of the open-hole CFRP specimen, and the the response will be compared to the results presented in C07.

In the following section, the details of the computational model are presented. These include the geometry of the model, material properties, the LaRC criteria utilized in C07, critical mesh size calculations, and some other combinations of parameters considered for this study. Finally, the results obtained from this parametric study will be presented, and the differences between the model considered here and that in C07 will be discussed.

4.2 Computational Model Description

4.2.1 Model geometry

A rectangular laminate with a central hole, as shown in Figure 4.1, is considered for modeling the intralaminar damage behavior. A symmetry about x-axis is assumed and only the upper half of the geometry is modeled. A $[0^0/\pm 45^0/90^0{}_7]_S$ ply orientation is assumed with each ply having a thickness of 0.1308 mm. Symmetry about the thru-thickness mid-surface of the laminate is also assumed for most simulations, leading to

further reduction of the model size (quarter of the original model) with only 10 plies explicitly modeled. However, for a few simulations, all 20 plies are modeled. Such cases will be explicitly pointed out during the discussion. For the rest of this chapter, it should be assumed that a quarter of the model with only 10 plies is considered.

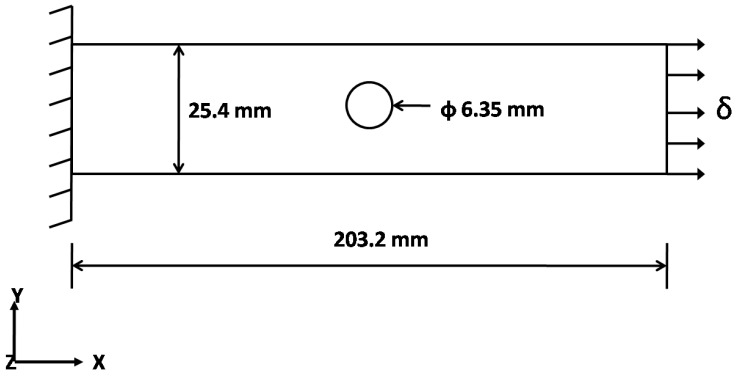

Figure 4.1: Rectangular laminate with a central hole.

4.2.2 Material properties

The material properties used in the simulations presented in this chapter correspond to carbon fiber reinforced epoxy T300/1034-C. The elastic properties, unidirectional strengths of the plies, and the fracture toughness values are tabulated in Tables 4.1, 4.2, and 4.3, respectively. The other important material property that

Table 4.1: Elastic properties of carbon/epoxy (T300/1034-C) laminate.

$E_1(GPa)$	$E_2(GPa)$	$G_{12} = G_{13} = G_{23}(GPa)$	ν_{12}
146.8	11.4	6.1	0.3

needs to be considered is the *in-situ* strength of the plies. Previous studies [59] and [14] have shown that the transverse tensile and in-plane shear strength of a ply increases due to constraints from neighboring plies, and are much higher compared to the corresponding strengths of an unconstrained ply. The *in-situ* strengths for T300/1034-C are tabulated in Table 4.4 [54]. In this study, the load-displacement response of the model with and without the use of *in-situ* strengths in the simulations will be investigated in detail.

Table 4.2: Unidirectional strengths of carbon/epoxy (T300/1034-C) laminate.

Longitudinal tensile strength $X_T(MPa)$	Longitudinal compressive strength $X_C(MPa)$	Transverse tensile strength $Y_T(MPa)$	Transverse compressive strength $Y_C(MPa)$	Longitudinal shear strength $S_L = S_T(MPa)$
1730.0	1379.0	66.5	282.2	58.7

Table 4.3: Fracture toughness of carbon/epoxy (T300/1034-C) laminate.

Longitudinal tensile fracture energy $G_{1+}(N/mm)$	Longitudinal compressive fracture energy $G_{1-}(N/mm)$	Transverse tensile fracture energy $G_{2+}(N/mm)$	Transverse compressive fracture energy $G_{2-}(N/mm)$
89.8	78.2	0.23	0.76

The orthotropic thermal expansion coefficients of the material used are $\alpha_{11} = -1.0 \times 10^{-6}/^0C$ and $\alpha_{22} = 26.0 \times 10^{-6}/^0C$. A temperature change of -152^0C is assumed [74] which represents the process of cooling the composite laminate from its curing temperature to the ambient temperature.

Table 4.4: In-situ strengths (MPa) of T300/1034-C.

	Thin embedded ply $(\pm 45^0)$	Outer ply (0^0)	Thick embedded ply (90^0)
Y_T	158.8	101.2	105.4
S_L	109.5	89.8	73.4

4.2.3 Loads and boundary conditions

The left end of the laminate is fully constrained. Y-symmetry boundary conditions are applied to the bottom edge as shown in Figure 4.2. When a quarter of the geometry (i.e., 10 plies) is modeled, Z-symmetry boundary conditions are applied to all nodes in the X-Y plane as shown in Figure 4.2. The specimen is loaded through displacement control of the right edge of the plate. Linear constraint equations are utilized to tie the nodes along the right edge to a single node (which is also known as the master node). The sum of the reaction forces due to the applied displacements at all the nodes on the right edge is available for output at the master node.

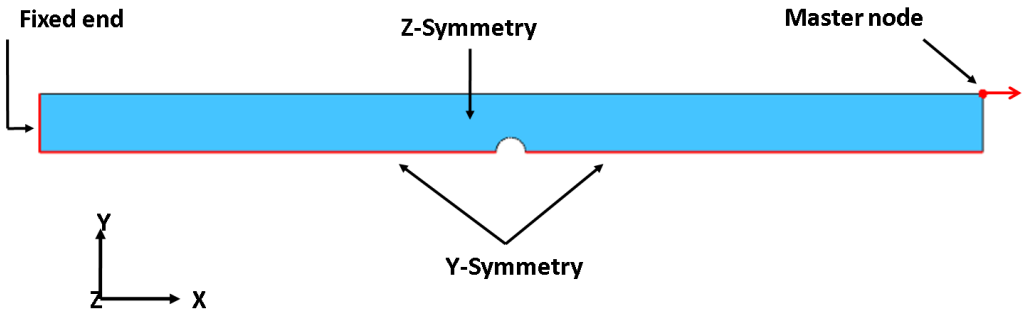

Figure 4.2: Loads and boundary conditions.

4.2.4 Mesh generation and critical mesh size

In this investigation two different mesh discretizations are utilized. The first mesh is uniform throughout the entire model, while the second mesh is non-uniform with additional refinement near the hole. The uniform mesh, shown in Figure 4.3, is generated within ABAQUS/CAE. The non-uniform mesh is similar to that used in

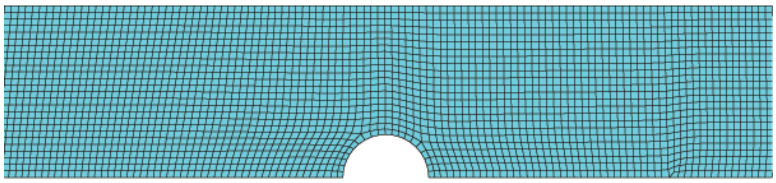

Figure 4.3: Uniform mesh discretization.

reference C07. This mesh was generated by partitioning the model and by using a combination of the different mesh control (and seeding) techniques available in ABAQUS/CAE. The mesh is relatively coarse away from the hole, as shown in Figure 4.4.

The mesh size chosen must ensure that the elastic energy of the element is less than or equal to the fracture energy [54] to avoid snap back in the constitutive relationship. The expressions for elastic energy and the fracture energy, respectively, are given by [54]:

$$U_n = \frac{X_n^2 l_{cr}^2 t}{2E_n} \tag{4.1}$$

$$g_n = G_n l_{cr} t, \tag{4.2}$$

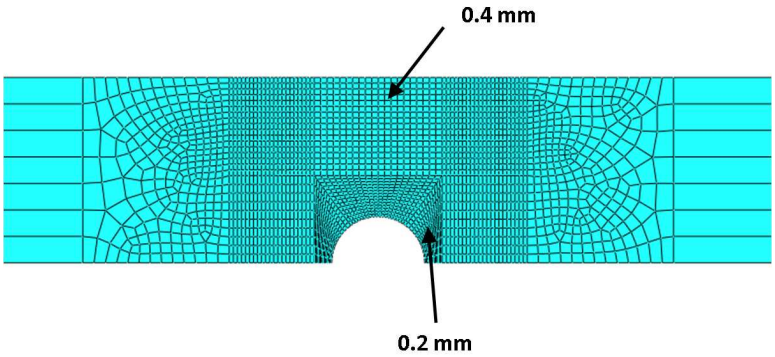

Figure 4.4: Non-uniform mesh discretization.

where the index n corresponds to the different modes of failure i.e. longitudinal tensile ($n = 1+$), longitudinal compressive ($n = 1-$), transverse tensile ($n = 2+$), transverse compressive ($n = 2-$) and in-plane shear ($n = 6$), X_n is the ply strength in each mode, l_{cr} is the critical element size, t is the ply thickness, E_n is the Young's modulus, and G_n is the fracture energy for each mode. From Equation 4.1 and 4.2, the maximum allowable size for an element may be expressed as [54],

$$l_{cr} \leq \frac{2E_nG_n}{X_n^2} \tag{4.3}$$

The maximum value of the element size predicted in C07 utilizing the *in-situ* strengths is 0.508 mm. It is not clear from C07 which *in-situ* strength needs to be used in equation 4.3. The combination of the material parameters for matrix tension mode of failure and the outer ply *in-situ* strength leads to a value that is close to that reported in C07. The maximum element size computed using these parameters is 0.512 mm. Based on this estimate, the mesh with uniform elements use an element size of either 0.5 mm or 0.25 mm. For the cases where the mesh is refined near the hole, a minimum element size of 0.2 mm and a maximum element size of 0.4 mm are used (Figure 4.4).

Reference C07 also suggests that in situations when the mesh size is larger than the critical value computed above, the strengths may be reduced to avoid the snap-back

in the stress-strain relationship. The adjusted strengths can be determined by:

$$X_n = \sqrt{\frac{2E_nG_n}{l_{cr}}} \tag{4.4}$$

This approach could be utilized to work with a coarse mesh in regions where extensive damage does not occur. This also justifies a non-uniform mesh that is very fine near the hole and coarser away from the hole.

4.3 Failure Criteria and Modeling Assumptions

A new set of plane stress failure criteria for fiber-reinforced polymer composites were developed by Dávila *et al.* [23]. These criteria were denoted as LaRC03. The LaRC03 criteria were further extended to general three-dimensional stress states [61], taking into account the effects of nonlinear in-plane shear response. The modifications to the LaRC03 criteria were denoted as LaRC04, and utilized in C07 to capture the intralaminar damage behavior of a composite plate with a hole.

The LaRC03/04 framework includes six equations that predict the progressive damage behavior of fiber-reinforced composites. The damage evolution laws force softening of the material as soon as one criterion is activated [54]. Exponential softening laws are used for all the failure modes except for the longitudinal tension mode (i.e., fiber failure mode). A general form of the six expressions is given by:

$$d_n = 1 - \frac{1}{f_n(r_n)} exp\{A_n[1 - f_n(r_n)]\}, \tag{4.5}$$

where, as before, n corresponds to each failure mode as explained under Equation 4.2, $f_n(r_n)$ is a function selected to force softening of the constitutive relation, and A_n are the adjusting parameters. The adjusting parameters are calculated based on the corresponding fracture toughness, the critical element size, and the corresponding strengths. These parameters also ensure that the dissipated energy computed by the numerical model is independent of the mesh refinement.

A more complex softening law has been proposed to predict the fiber failure. This law is a combination of a linear and an exponential degradation response. The response is linear till the stress reaches the so called *pull out stress*, and switches to

an exponential softening response with further increase of the stress. Thus, the total fracture energy for the longitudinal tensile mode is the sum of the energy associated with the linear softening law ($G1+_L = 20N/mm$) and the exponential softening law ($G1+_E = 69.8N/mm$). In this part of the study, we model the intralaminar damage behavior of the ply using Hashin's criteria in which the damage evolution is driven by a linear softening law. We also model the damage behavior of the ply using Linde's set of criteria in which the evolution is governed by an exponential softening law. The details of these criteria are mentioned in the previous chapter 3. The response obtained using these criteria will be compared to the results from C07. We expect the knowledge gained from this work to provide us with additional insights to investigate the problem of simulating both intralaminar and interlaminar damage behavior.

Some of the differences between the computational model used in C07 and the model utilized in this study are:

1. The failure model used in C07 is based on the LaRC criteria, while our model utilizes either Hashin's or Linde's failure criteria.

2. C07 uses an exponential damage evolution law for each damage mode other than longitudinal tension, and a combination of linear and exponential softening laws for longitudinal tension. Our modeling approach, when used with Hashin's damage model, uses linear softening laws for all the damage modes. On the other hand, an exponential law is utilized when our model uses Linde's criteria.

3. C07 accounts for the Mode II transverse fracture energy, $G6$. This parameter is not utilized in either the Hashin or the Linde model.

4. C07 uses an implicit dynamic analysis, while our model carries out a static analysis.

5. C07 uses a fully integrated shell element (S4 in ABAQUS). We use three different types of elements–reduced integration conventional shells, 8-node continuum shells, and 8-node reduced integration solids (S4R, SC8R, and C3D8R, respectively, in ABAQUS).

In the following section we discuss the results of our simulations. The section is arranged as follows. The results for the conventional shell elements are discussed first, and this is followed by the results for the continuum shell elements and continuum solid elements. For each of these element types, different cases analyzed are outlined and the corresponding results discussed. The authors of C07 kindly shared with us with the ABAQUS input file for their model. This enabled us in understanding some of the key differences between the two modeling approaches. Also, some cases were analyzed in which Hashin's criteria and Linde's model were incorporated in C07. The responses for these cases are also discussed in the following section.

4.4 Results and Discussion

The results obtained from a parametric study involving different cases are discussed below. Quarter symmetry of the model is considered for all the cases (10 plies with "Z-symmetry" boundary conditions). Some cases with half symmetry (20 plies) are also analyzed in order to validate the quarter symmetry assumption. Some of the common aspects in the modeling approach for all cases are as follows,

1. The first step is a thermal step in which the laminate is cooled from the curing temperature to the ambient temperature. This step is important as the change in temperature would result in residual stresses that might have an effect on the damage behavior of the ply. In the first step a temperature change of $-152°C$ is applied and this temperature condition is carried onto the 2nd step.

2. The second step is static, with a displacement-controlled loading.

3. The different plies are modeled using a composite shell section, with one integration point per ply.

4. All simulations are carried out with a stabilization factor of 1e-5. The results were similar for even lower values of stabilization.

Note: In all the following sections and sub-sections, the term "unidirectional properties" refers to the global ply properties with the transverse tensile strength, $Y_T = 66.5MPa$, and the longitudinal shear strength, $S_L = 58.7MPa$. When the term

"*in-situ* strengths" is used in regards to the definition of the material properties, the magnitudes of Y_T and S_L are changed for each ply based on the *in-situ* strength data from C07.

4.4.1 Parametric study using conventional shell elements

Uniform mesh:

In this section, we present results for the composite plate-with-a-hole problem using conventional shell elements (element type S4R in ABAQUS). The entire model is discretized utilizing a uniform element size. Hashin's criteria are used to predict the onset of damage within the plies. The following are the different cases considered:
Case 1: The unidirectional ply properties are used as-is (i.e., the *in-situ* strengths are neglected). The fiber fracture energy $G1+$ is assumed to be 89.8 N/mm (the sum of the fracture energy associated with linear softening, 20.0 N/mm, and that associated with exponential softening, 69.8 N/mm).
Case 2: Similar to case 1, except that the fiber fracture energy is reduced to half: (45 N/mm). This step was carried out based on private communication with the authors of C07 that suggested that in the absence of an exponential softening law, using half the fracture energy with a linear softening law captures the damage response better.
Case 3: The *in-situ* strengths are used for the outer ply (0^0), thin embedded ply ($\pm 45^0$), and thick embedded ply (90^0). The fiber fracture energy is assumed to be half of its original magnitude (i.e. 45 N/mm).

Figure 4.5 shows a comparison of the load-displacement responses for cases 1, 2 and 3 for element size of 0.5 mm, along with the results from C07. It can be observed that with just the unidirectional strengths specified (case 1) the peak load and displacements from the present simulation are significantly higher compared to the results presented in C07. Additionally, the slope of the load-displacement response agrees well initially with C07. However, the slope reduces at a value of displacement that is approximately half the total displacement, and the overall load-displacement response deviates from the linear response presented in C07. By reducing the fiber fracture energy (case 2) the response follows the same path as in case 1, but the peak load and displacement are somewhat lower (and closer to the results presented in C07). As in

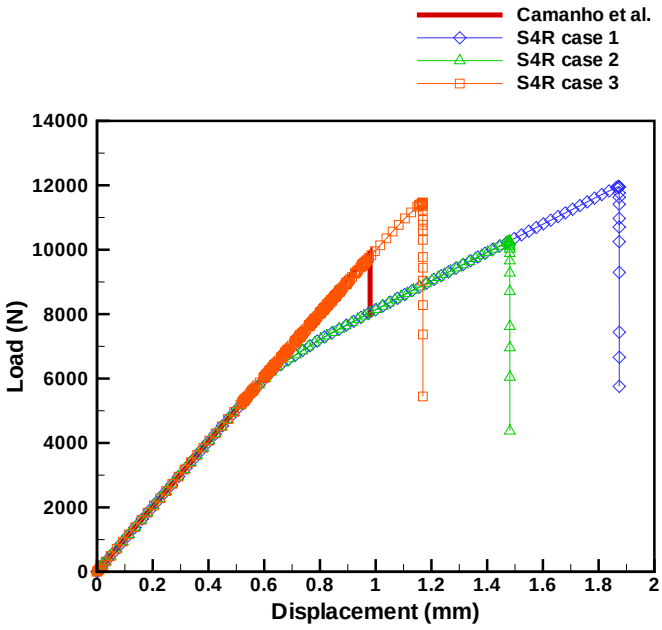

Figure 4.5: Load-displacement response using S4R elements (0.5 *mm*) with Hashin's criteria.

case 1, a deviation from a linear response is also observed. The non-linear response is not observed when the *in-situ* strengths are used in the simulations (case 3), and the slope of the load-displacement response in this case matches very well with the results in C07. However the peak load and displacement are still somewhat higher compared to C07. The results for case 3 did not change when a half-symmetry (20 plies) model was used. The response with 20 plies for case 3 is shown in Figure 4.6. Figure 4.7 shows the results for the three cases (1, 2 & 3) for a uniform element size of 0.25 *mm*. These results show trends similar to the earlier results for the 0.5 *mm* case. Also in this figure, the results from the quarter-symmetry model are compared to the results for the half-symmetry model for case 3 only, showing essentially no differences in the results between these two assumptions. Figure 4.8 compares the load-displacement responses for different element sizes of 0.5 *mm* and 0.25 *mm*, respectively, and for case 3. The 0.25 *mm* element size predicts a marginally higher peak load and displacement.

As discussed earlier, in the absence of an exponential softening law, the fiber fracture energy was reduced by a factor of two in the simulations for cases 2 and 3.

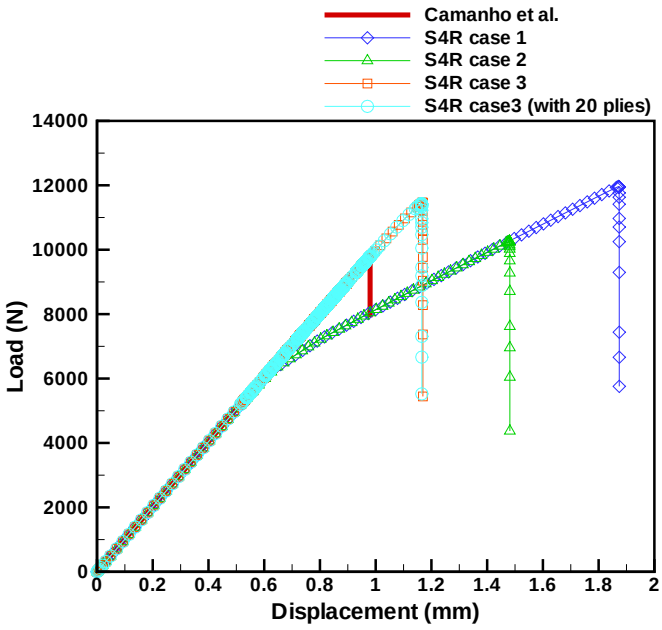

Figure 4.6: Load-displacement response using S4R elements (0.5 mm), with Hashin's criteria, and symmetry comparison.

This resulted in peak loads that are much closer to the load predicted in C07. By further reduction of the fiber fracture energy to 35 N/mm, a corresponding reduction in the peak load and displacement was also observed. The results are shown in Figure 4.9; it may be noted that the additional reduction of the fiber fracture energy did not bring the peak loads and displacements much closer to the results in C07. The results suggest that while the strategy of reducing the fiber fracture energy in lieu of using an exponential softening law brings the peak load a lot closer to earlier reported values (C07, and experimental results referred to therein), further reduction beyond a factor of 2 does not appear to have a significant effect on the global response.

Nonuniform mesh:

The model discretized using a non-uniform mesh is shown in Figure 4.10. This particular strategy for non-uniform meshing was motivated by a similar approach used in C07, as well as the general notion that most of non-uniformities in the field quantities would be near the hole. As shown earlier in Figure 4.4, the mesh near the hole is twice as refined (element size: 0.2 mm) compared to the far-field mesh (element size: 0.4 mm). As with the case for the uniform mesh, Hashin's criteria were utilized to

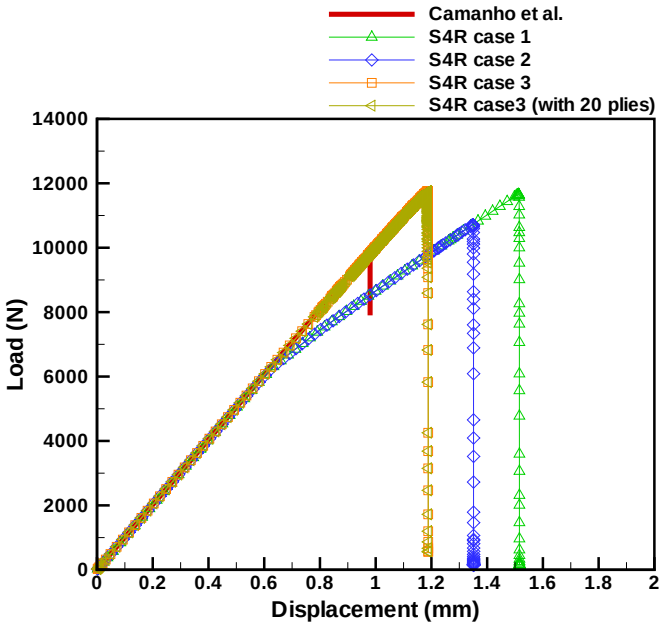

Figure 4.7: Load-displacement response using S4R elements (0.25 mm), with Hashin's criteria, symmetry comparison.

predict the onset of damage for the different case studies. Additionally, the model used in C07 was modified to use Hashin's criteria (recall that C07 uses the LaRC family of failure criteria) so that the response from that model can be compared with that from our model. Some of the differences between the two models, with more details on the modeling aspects are outlined towards the end of this section.

case 4: The elements in each ply are divided into 2 sets. We denote the elements in these two sets as *damage* elements and *linear* elements, respectively, as shown in Figure 4.10. The unidirectional ply properties are used directly to define the constitutive response of the linear elements, while the *in-situ* strengths are used for the damage elements. The fiber fracture energy for both the element sets is assumed to be 89.8 N/mm (i.e., same magnitude as described in the earlier section for case 1).

Case 5: The thin embedded ply ($\pm 45°$) *in-situ* strength is used to define the response of the linear elements. However, all the fracture energies associated with the fiber and the matrix in the linear elements are increased by a factor of 1000 compared to the damage elements. Additionally, the fiber fracture energy in the damage element

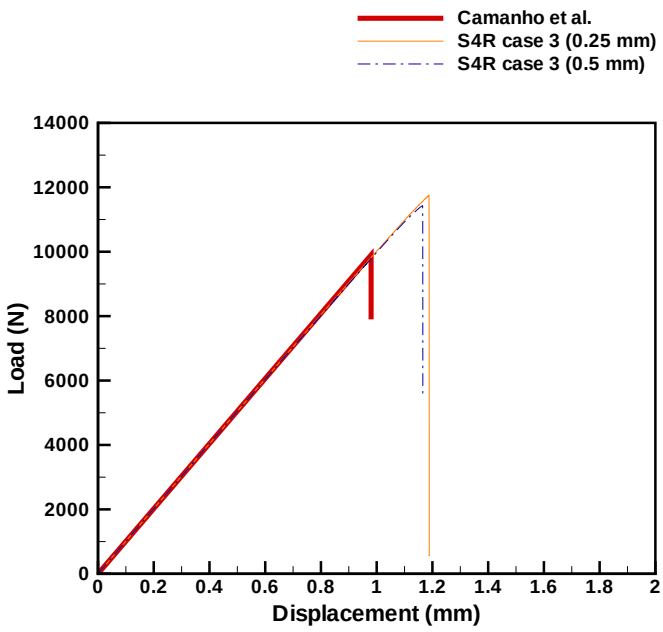

Figure 4.8: Load-displacement response for varying element size using Hashin's criteria, case 3.

set is reduced to half (45 N/mm). These strategies were motivated by private communication with the authors of C07.

Case 6: For this case we do not distinguish between the linear and the damage elements, and instead use the *in-situ* strengths for all the plies over the entire model. This case is similar to case 3 discussed earlier; the only difference being a refined mesh near the hole.

Figure 4.11 shows the fiber fracture plane that occurs due to a load in the X-direction. In all the refined mesh cases, the fiber failure occurred in 0° ply as shown in Figure 4.11. This location is consistent with fracture plane reported in C07. The stretched elements are completely damaged in the fiber tension mode as shown in Figure 4.11. The response of S4R elements for cases 4, 5 and 6 are plotted in Figure 4.12. In case 4 the slopes agree well with C07 up to a displacement of about 0.6 mm, after which slopes diverge from each other. A plateau region with oscillations in the load appears to be occurring right after the slopes diverge. At this instant in the loading history, damage under the matrix tension mode occurs in the *linear* element set, away from the hole, and slowly propagates toward the *damage* element set, near

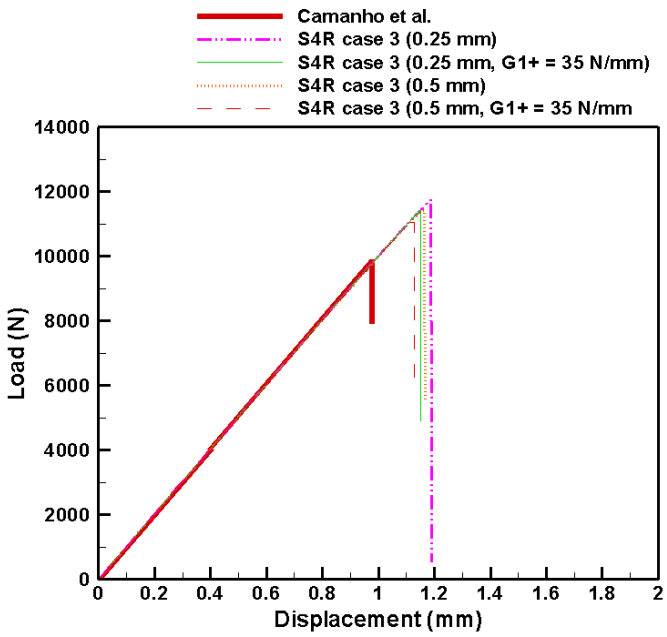

Figure 4.9: Load-displacement response, comparing the effect of reduced fiber fracture energy (G1+) for case 3 using Hashin's criteria.

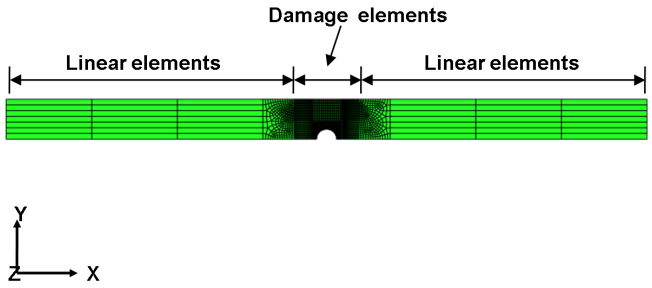

Figure 4.10: Non-uniform mesh with different element sets.

the hole. It is possible that the matrix crack is not propagating in a monotonic fashion, leading to oscillations in the load-displacement response. From Figure 4.12, it can be observed that the slope of the response for cases 5 and 6 matched well with C07. It also appears that the magnitude of the peak load and displacement predicted in 5 and 6 are almost the same. It should be noted that in case 5, the fiber and matrix fracture energies defined for the linear element set (away from the hole) are multiplied by a factor of 1000, probably to force localization of damage near the hole instead of away from the hole, as mentioned previously for case 4. In case 6, the material properties (considering the *in-situ* strength with half fiber fracture energy,

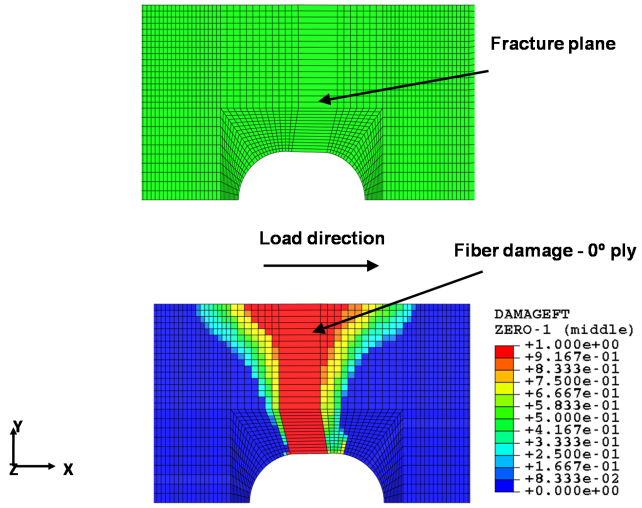

Figure 4.11: Fracture plane in the 0° ply.

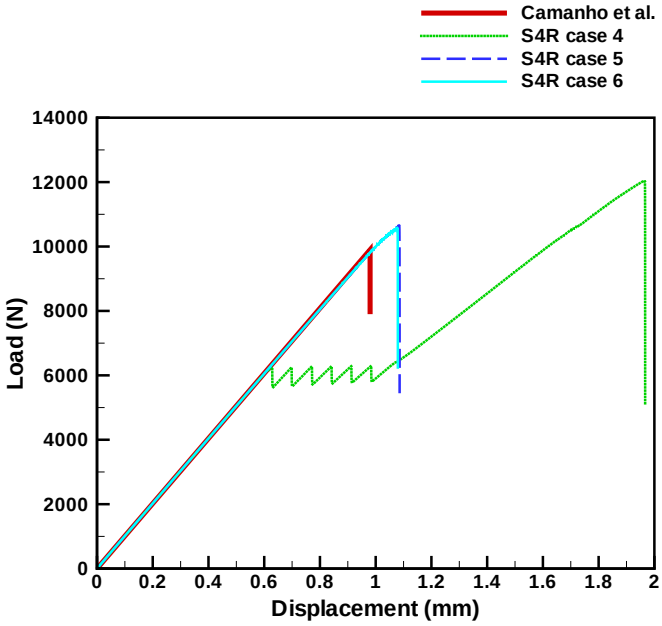

Figure 4.12: Load-displacement response for the refined mesh cases using Hashin's criteria.

45 N/mm) are defined to the entire model. Thus, in our model, the strategy used by the authors of C07 (case 5) did not appear to make an effect on the load-displacement response, when cases 5 and 6 were compared.

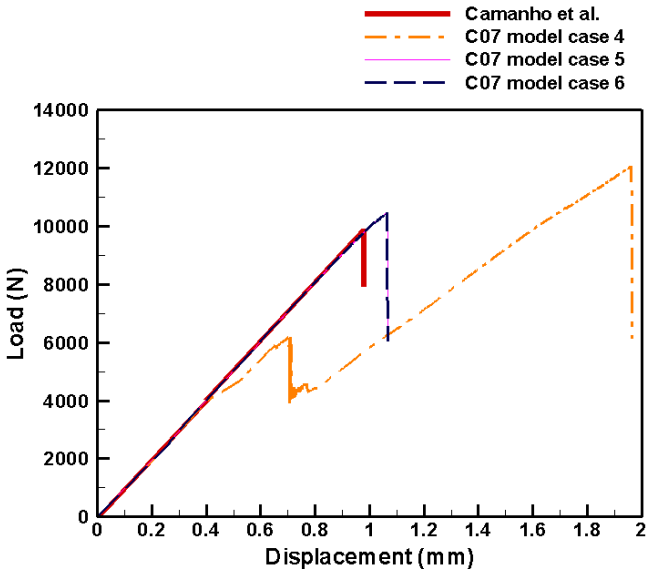

Figure 4.13: Load-displacement response for C07 model with Hashin's criteria.

Next we present the results obtained utilizing the model used in C07, with the material properties for the LaRC failure criteria substituted with corresponding properties needed for Hashin's criteria. The responses for cases 4, 5 and 6 are qualitatively similar to the corresponding response observed from our model, and are shown in Figure 4.13. The plateau region of oscillations observed in Figure 4.12 for case 4 was also observed in the model from C07 but with a varying amplitude. The peak load and displacement predicted from the model used in C07, for cases 5 and 6, showed good qualitative and quantitative agreement with our model (shown in Figure f:c4-f14). Figure 4.14 shows a comparison (on the same plot) between the results from our model (with a refined mesh) and the results from the C07 model.It may be noted that the same stabilization factor (1e-5) is used when comparing our model with the C07 model.

As pointed out earlier case 6 is the same as case 3, with the only difference being the refined mesh in case 6 instead of the uniform mesh in case 3. Figure 4.15 compares the responses from our model (for both cases 3 and 6) with the corresponding results from the C07 model. It is clear that the refined mesh is able to predict the peak load and displacement better than the uniform mesh.

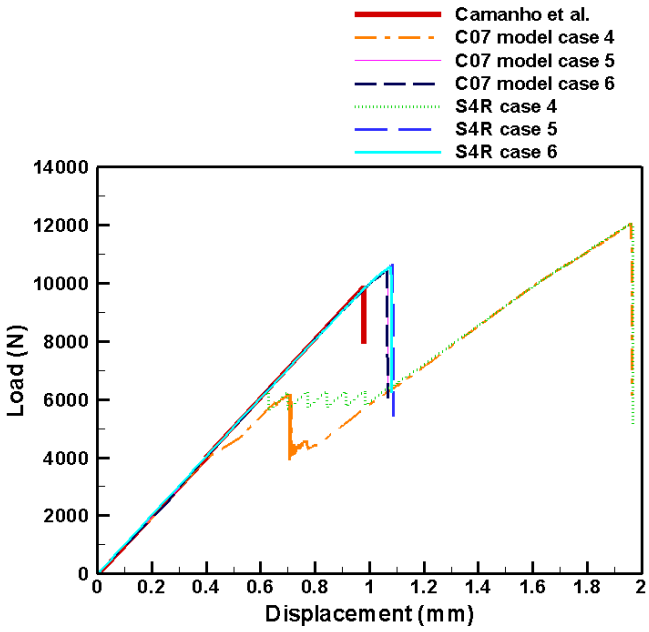

Figure 4.14: Load-displacement response comparing C07 model with our model, both using Hashin's criteria.

In the following we provide more details regarding the differences between the C07 model and our model:

1. The C07 model uses an implicit dynamic analysis step, while our analysis is static. We carried out an implicit dynamic analysis with our model, and obtained a marginally higher peak load and displacement compared to both C07 and our static analysis. This can be attributed to the difference in mesh and the HAFTOL parameter. Initially, our model did not converge using the HAFTOL value from the C07 model (15,000). It appears that the analysis ended just before the final failure occurs. When the HAFTOL parameter was reduced (12,000), our model converged, but the peak load and displacement obtained was slightly higher compared to the results from the static analysis. A parametric study might help to determine the appropriate HAFTOL to be used in our model. The density value for the implicit dynamic analysis was chosen from C07.

2. The number of elements (1736) in the C07 model is lesser than our model (2630).

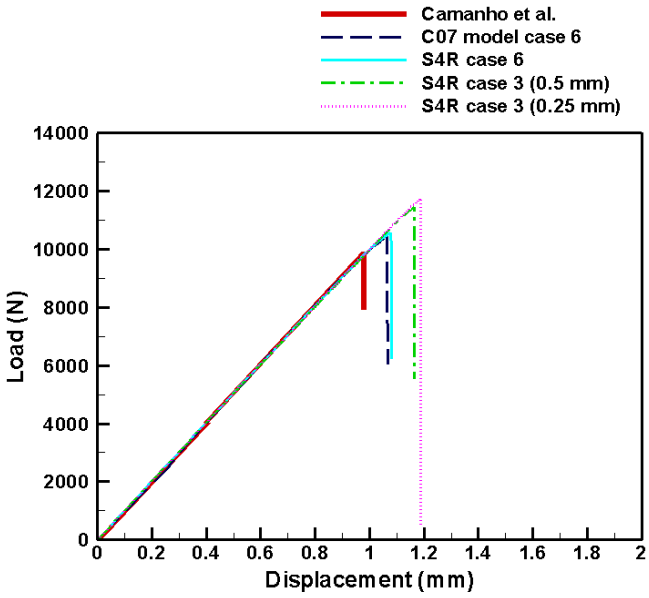

Figure 4.15: Load-displacement response comparing C07 model with our model for cases 3 and 6, both using Hashin's criteria.

3. The solution control parameters used in the C07 model and our static model are different.

4. The C07 model uses S4 (fully integrated conventional shells) elements while our model uses S4R elements (reduced integration conventional shells). This difference can be neglected as the response using S4 elements in our model was very close to the response from S4R elements

5. The transverse shear response is explicitly defined in the the C07 model. However, including the transverse shear response in our model did not change the response for any of the cases that were analyzed without explicitly specifying the transverse shear stiffness.

Results from both uniform and refined mesh using Linde's model:

In this section, we present results utilizing the progressive damage model recently proposed by Linde *et al.* [49] that uses an exponential damage evolution law. This model is available as a user-subroutine (UMAT) with the released version of

ABAQUS. Simulations utilizing Linde's model were carried out for case 3 for the uniform mesh, and case 6 for the refined mesh. Recall that cases 3 and 6 are essentially the same, except for the difference in the mesh, and yielded the closest agreements with the C07 results in the earlier simulations. In addition to cases 3 and 6, the response of a model using unidirectional ply properties is also investigated. To this end, the cases presented earlier with labels 1 and 6 are re-analyzed with unidirectional properties. The fiber fracture energy is assumed to be its original (and full) value of 89.9 N/mm for all simulations using the Linde model. This is because an exponential damage evolution law is used with the Linde model (adjustments to the fiber fracture energy are only needed when a linear damage evolution law is used).

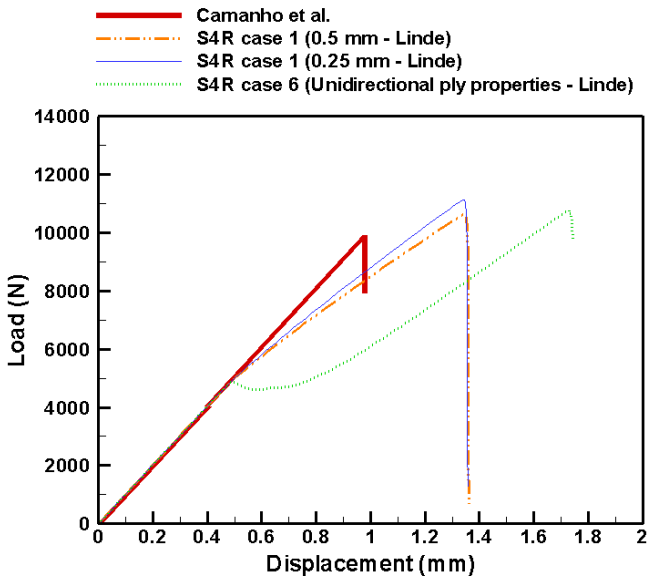

Figure 4.16: Load-displacement response using Linde's model with unidirectional ply properties.

Figure 4.16 shows the results obtained by using Linde's model for case 1 (0.5 mm and 0.25 mm element size) and case 6 (refined mesh, with unidirectional properties). The results for case 1 using 0.5 mm and 0.25 mm element sizes show generally similar trends, including a deviation from the linear response before reaching the peak load. However, case 6 utilizing unidirectional ply properties predicts a small drop in load at a relatively small applied displacement, which is followed by a load-displacement

response with a positive slope that is somewhat lower than the slope in the first branch of the same response (i.e., slope of the response before the small drop in load). Figure 4.17 shows the load displacement response for case 3 with two different (uniform) mesh sizes, and case 6 (with non-uniform mesh). It can be observed that the response is not very sensitive to the mesh. In Linde's model the exponential evolution law accounts for the characteristic element length in formulating the softening response, which reduces the mesh sensitivity of the global results. The characteristic element length is taken in to account in Hashin's criteria of damage evolution as well. The peak load and displacement predicted by the 0.5 mm and 0.25 mm element sizes (case 3, Figure 8.8) were close to each other with a difference in magnitudes of, approximately less than 3%.

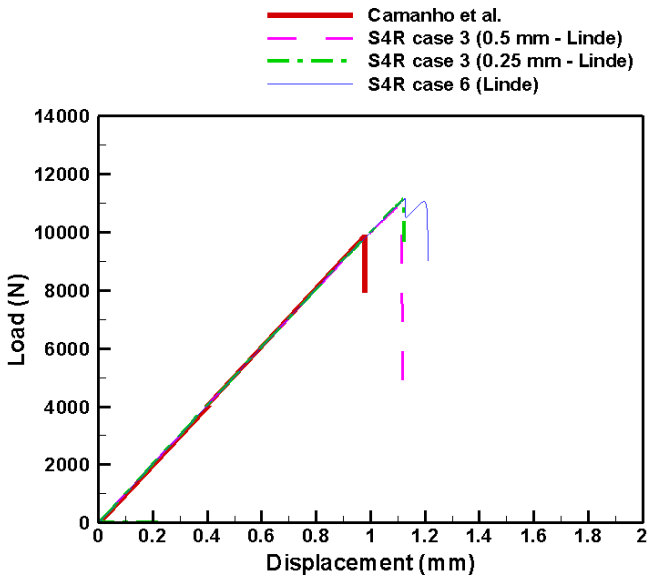

Figure 4.17: Load-displacement response for varying element size using Linde's model.

Figure 4.18 shows a comparison of the load-displacement responses obtained using Hashin's and Linde's criteria, respectively. The two cases considered for comparison purposes are: (i) case 3 (uniform mesh) with 0.5 mm and 0.25 mm element sizes, and (ii) case 6 (refined mesh). By comparing the results for case 3, it can be observed that the peak load and displacement obtained using Linde's criteria (that uses full fiber fracture energy because the softening response in exponential) are closer to the peak

load and displacement reported in C07, compared to the results with Hashin's criteria (that uses half the fiber fracture energy to compensate for linear softening) . On the other hand for case 6, it can be observed that the model using Hashin's criteria predicts a lower peak load and displacement compared to Linde's model. In fact, in this case the Hashin results are closer to the results from C07. This provides motivation for modifying the Hashin damage modeling framework to accommodate exponential softening; however this modification will not be pursued in this dissertation and is suggested future work in this area. The mesh-dependent reversal of behavior observed in the results also deserves further investigation. From the response of case 6 using Linde's model (Figure 4.18), it appears that the structure experiences a local peak prior to reaching a global peak. This results in a slight increase in load right after the first load drop.

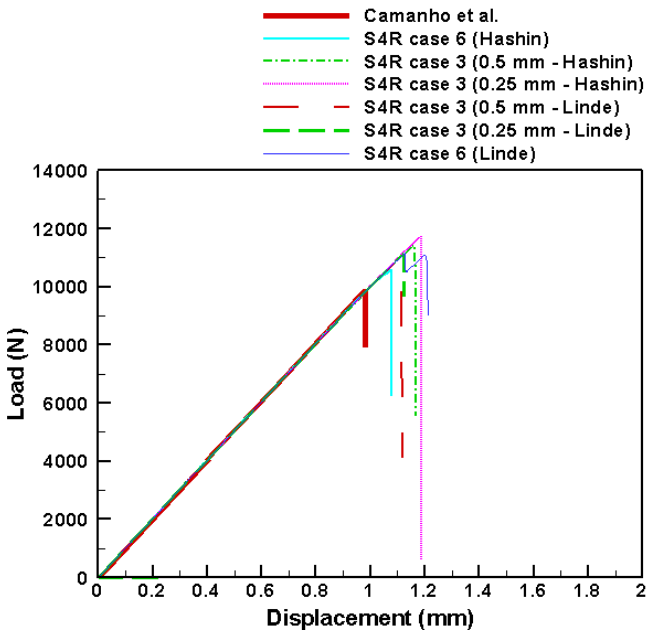

Figure 4.18: Load-displacement response comparing Linde's model with Hashin's criteria.

4.4.2 Parametric studies using continuum shell elements

Uniform mesh cases:

In this section, we present results for the composite plate-with-a-hole problem using continuum shell elements (element type SC8R in ABAQUS). These elements have

a topology that is similar to solid continuum brick elements (i.e., 8 nodes instead of 4); however the kinematic and constitutive calculations are based on a plane-stress assumption. In this approach, each ply can either (i) be modeled as a single shell element, or (ii) a fraction of a shell element (through the thickness) if the composite shell modeling paradigm is used. We used the latter approach as it was deemed to be less intensive computationally. We have obtained results for a number of different cases. The first set of cases analyzed is similar to cases 1, 2 and 3 (discussed earlier) with element sizes of 0.5 mm and 0.25 mm, respectively. Although the difference between the cases presented below and cases 1, 2 and 3 presented in earlier sections is in the element type, we define separate cases with continuum shell elements for better clarity. In the discussion to follow we will refer to continuum shell elements using the corresponding element-type in the ABAQUS element library: SC8R. The different cases that will be studied are as follows:

Case 7: Unidirectional ply properties with the full value of the fiber fracture energy (89.8 N/mm) are used for the entire model. Only one element (with ten composite sections to represent the ten plies) is used in the thickness direction and quarter-symmetry (10 plies) conditions are assumed. The total thickness of the laminate is 1.308 mm.

Case 8: Same as case 7, except that the fiber fracture energy is reduced by a factor of 2 to 45 N/mm.

Case 9: The *in-situ* strengths are used for the entire model and the fiber fracture energy is assumed to be half of its original value, i.e., 45 N/mm.

The load displacement responses for cases 7, 8 and 9 with 0.5 mm element size are shown in Figure 4.19. The qualitative behaviors for the different cases are similar to the corresponding behaviors observed earlier with S4R elements (Figure 4.5), but both the peak load and peak displacement are much higher in magnitude. The deviation of the response from linearity is observed early on for both cases 7 and 8, and as expected, case 8 results in lower peak load and displacement. For case 9, even though the *in-situ* strengths are used in place of the unidirectional strengths, the slope of the response

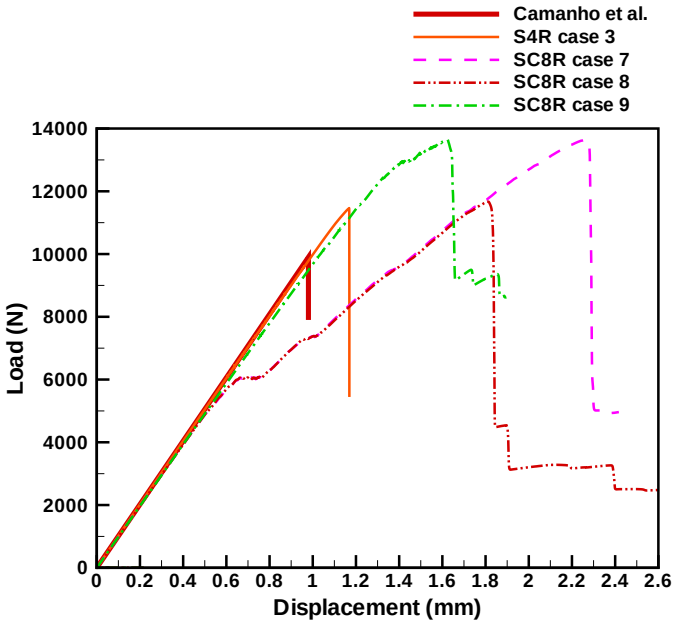

Figure 4.19: Load-displacement responses using SC8R elements (0.5 mm) with Hashin's criteria.

shows a small deviation from linearity before the peak load is attained. Recall that for the simulations using S4R elements, the slope of the response remained linear and matched very well with that of the C07 results. To facilitate a direct comparison of the responses using conventional shells (S4R) and continuum shells (SC8R), we have added the response for case 3 in the same plot. The results suggest that the S4R elements capture the overall response better than SC8R elements.

Figure 4.20 shows the corresponding results for an uniform mesh of continuum shells (SC8R) with an element size of 0.25 mm. The implicit finite element calculations for case 7 did not converge (with stabilization factor of 1e-4), and therefore the load drop is not shown for this case. Convergence could be obtained with a higher stabilization factor, but our general experience in this matter suggest that a higher stabilization driver would also result in a higher peak load and displacement. By reducing the fiber fracture energy (case 8), we observe that the response follows the same path as that in case 7. The results for case 9 predict a higher peak load and displacement, similar to the earlier discussed results for 0.5 mm element size. The figure also shows the response obtained using S4R elements (case 3), and as observed

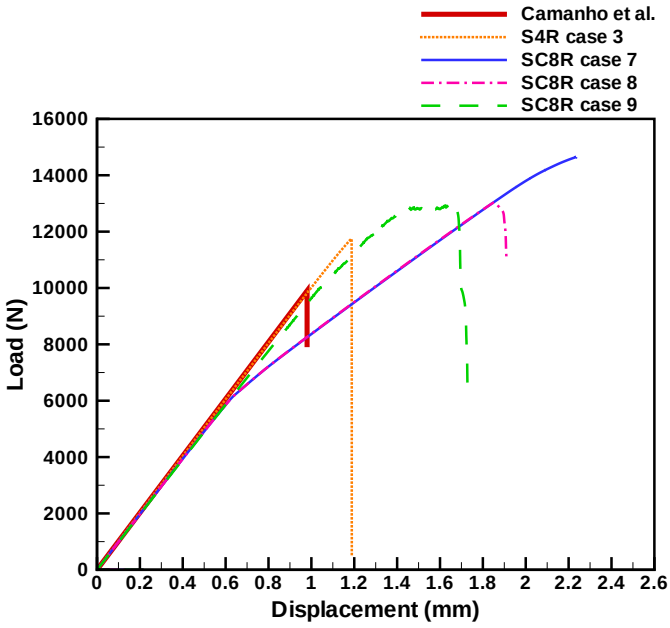

Figure 4.20: Load-displacement response using SC8R elements (0.25 mm) with Hashin's criteria.

earlier, the response with S4R elements agree better with the results presented in C07.

Figure 4.21 shows a plot comparing the results for 0.5 mm and 0.25 mm element sizes using both S4R (case 3) and SC8R (case 9) elements. We have picked cases 3 and 9 for comparison because, based on our earlier observations, the results for these cases are, in relative tersms, in better agreement with C07. Similar to our observation with S4R elements, in the case of SC8R elements the 0.25 mm element size predicts a slightly higher peak load when compared to the peak load for an element size of 0.5 mm. However, unlike what was observed with S4R elements, the 0.5 mm element size predicts a slightly larger displacement. Overall the results suggest that the SC8R elements with just 1 element through the thickness predict a much larger peak load and displacement when compared to S4R elements. Additionally we also observe that the load drop for the simulations with SC8R elements is not as sharp as in the case of S4R elements.

Based on the observations made from cases 7, 8, and 9 (all using a single SC8R element through the thickness), additional simulations are carried out with two and

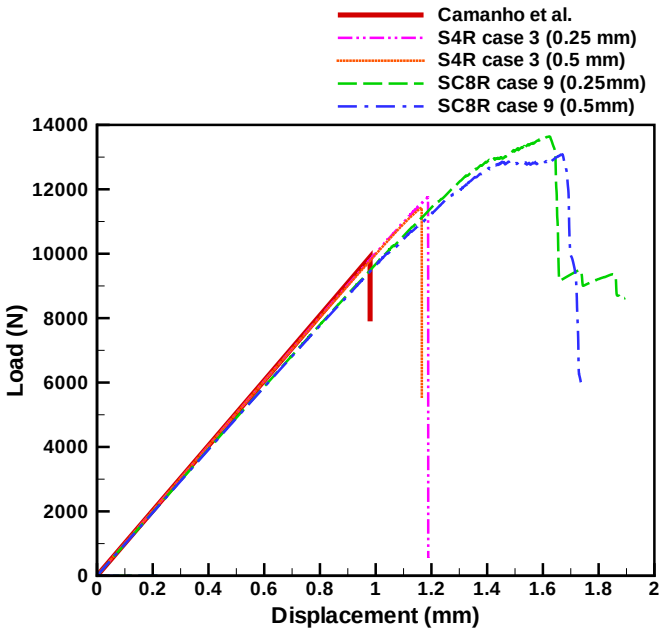

Figure 4.21: Load-displacement response comparing the element types (S4R & SC8R) for varying element sizes using Hashin's criteria.

five SC8R elements, respectively, through the thickness. The additional cases are analyzed for 0.5 mm element size because the earlier results were observed to be relatively insensitive to the element size. The details for these cases are as follows:

Case 10: The *in-situ* strengths and half the fiber fracture energy (45 N/mm) are used for the entire model. This is similar to case 9 except that in the present case, two elements are used in the thickness direction. The ten plies are simulated by defining two composite shell sections, with five plies in each section.

Case 11: This case is similar to case 10 except that five elements are used in the thickness direction. Naturally, this required five composite shell sections with two plies for each section.

Figure 4.22 shows a comparison of the results obtained with SC8R elements (cases 9, 10, and 11) along with that for S4R elements (case 3). The results from cases 10 and 11 are close to each other and the peak load for these cases are relatively closer (when compared to the earlier cases, such as case 9, with SC8R elements) to the results presented in C07. In particular, the peak displacement with five SC8R elements through the thickness (case 11) agrees very well with the S4R (case 3) results. It can

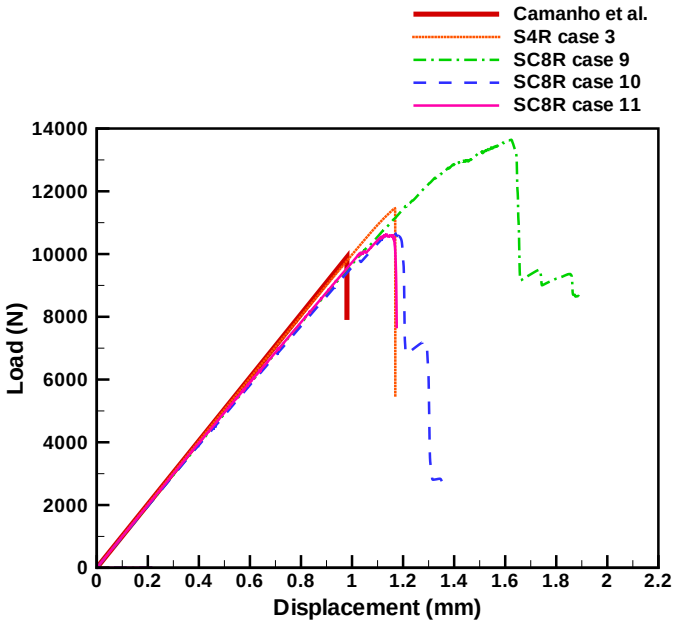

Figure 4.22: Load-displacement response using SC8R elements (0.5 mm) for varying number of elements through thickness, with Hashin's criteria.

also be observed that the slopes of the response using SC8R elements deviate from the nominal linear response at relatively high loads for both cases 10 and 11. This aspect of the results suggest that the onset of progressive damage occurs somewhat earlier in the simulations with SC8R elements. It is not entirely clear why this is so, and pending further investigation we can only surmise that the differences in the kinematics between the two element formulations leads to these differences. Overall, the above results strongly suggest that more than one element is needed through the thickness for simulations with SC8R elements. The issue of whether to use S4R elements or SC8R elements must then be decided based on other considerations such as (i) overall computational cost, and (ii) ease of use with respect to other advanced features such as the modeling of contact.

Refined mesh:

A refined mesh, similar to the one using S4R elements, is used for the simulations discussed in this section. The different element sets (damage and linear elements) considered in cases 4 and 5 (using S4R elements) are ignored, and all material properties are defined to be the same for the entire model. The different cases considered

are as follows:

Case 12: Unidirectional properties of the plies and the full magnitude of fiber fracture energy (89.8 N/mm) are used. This case is similar to case 7 (with SC8R elements), except that the mesh discretization is different. A single element is used in the thickness direction.

Case 13: The *in-situ* strengths of the plies and half the fiber fracture energy (45.0 N/mm) are used. Only one element is used in the thickness direction. Previous observations suggest that the response using the unidirectional properties and half the fiber fracture energy would likely follow the same path as in case 12, with a lower peak load. Therefore, the case of half the fiber fracture energy with unidirectional properties (similar to case 8) is ignored.

Case 14: The material definition is same as in case 13. However, two elements are used in the thickness direction (similar to case 10).

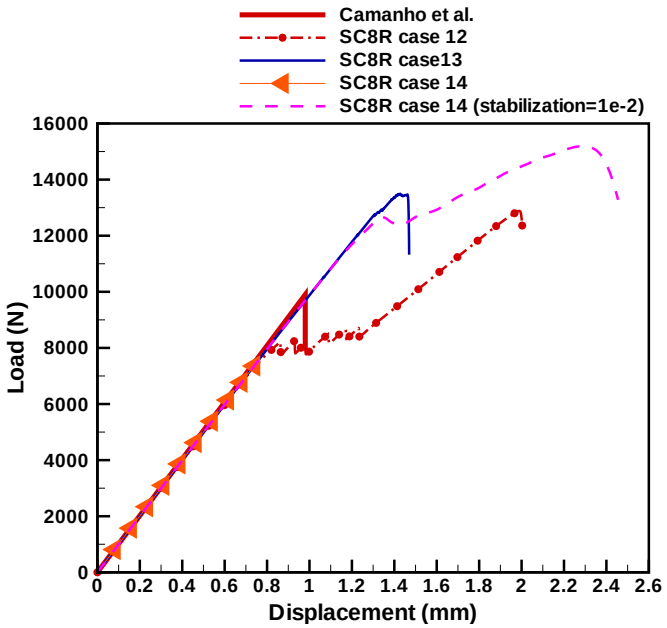

Figure 4.23: Load-displacement response using SC8R elements (refined mesh) with Hashin's criteria.

Figure 4.23 shows the load-displacement responses for cases 12, 13, and 14. The nonlinear implicit finite element simulation for case 12 did not converge to completion, similar to case 7 (uniform mesh with 0.25 mm element size, Figure 4.20). When the

in-situ strengths are used (case 13), the slope of the response agrees well with the results in C07, but the peak load and displacements are predicted to be higher. The nonlinear implicit finite element simulation for case 14 did not converge initially with a stabilization factor of 1e-4. The stabilization factor required for the analysis to converge was 1.e-2. The results show that a higher value of the stabilization factor leads to a higher load and displacement, as would be expected.

Comparison between Linde and Hashin models for both uniform and refined mesh simulations

In this section we compare the results obtained using Hashin's failure model, both uniform and refined mesh cases, with corresponding results obtained using Linde's model. To this end, the simulations for cases 7, 9, and 10 (all with uniform mesh) and cases 12, 13, and 14 (all with refined mesh) are repeated, using Linde's model to define the progressive damage responses of the plies. From previous observations, the results for cases 10 and 11 (uniform mesh, but with two and five elements, respectively, through the thickness, and using Hashin's criteria) were found to be close to each other. Therefore, the case with an uniform mesh and five elements through the thickness is not considered any further in this section. Figure 4.24 shows that with unidirectional ply properties, the slopes of the load-displacement curves for both the Hashin model and the Linde model deviate from the linear response observed in C07. This is consistent with the corresponding observations from the simulations using S4R elements. Results for case 7 with the Linde model show that the peak load and displacement are significantly reduced with an exponential damage evolution law (as compared to a linear damage evolution law for the Hashin model). As mentioned earlier, the nonlinear implicit finite element simulation for case 12 (refined mesh with Hashin's model) did not converge all the way with a stabilization factor of 1e-4. However, the response for this case seems to be following the path of the responses from case 7 (Hashin) and case 12 (Linde). Figure 4.25 compares the responses for simulations that use the *in-situ* strengths of the plies and half the fiber fracture energy, with an uniform mesh (case 9) and a refined mesh (case 13). The results

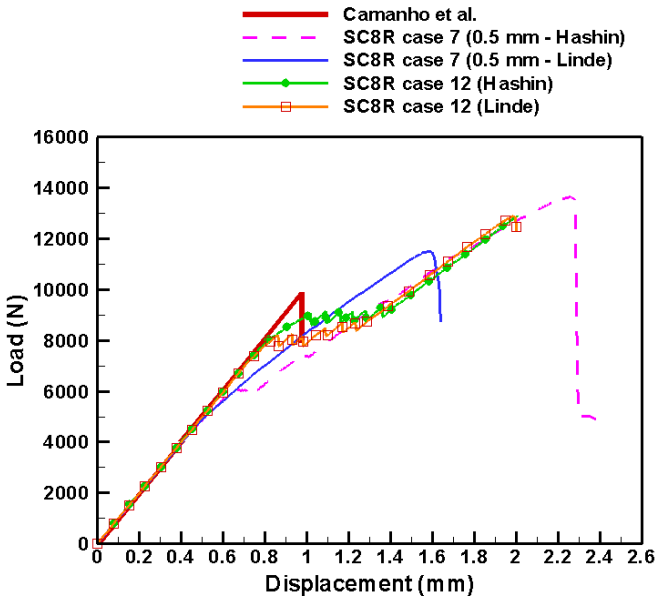

Figure 4.24: Load-displacement responses comparing Hashin's and Linde's models with SC8R elements (uniform and refined mesh cases).

suggest that when the *in-situ* strengths and half the fiber fracture energy are used with the Hashin model, the slope of the response from the refined mesh matches the slope from C07 marginally better than the response from the uniform mesh (with 0.5 *mm* element size). However, the peak load and displacement predicted in both these cases are higher compared to C07. On the other hand, the simulations using Linde's model (both cases 9 and 13) did not converge with a stabilization factor of 1e-4. As discussed previously, a converged solution may be obtained if a higher stabilization factor is used. However, in such cases the predicted peak load and displacement will likely be much higher when compared with C07 (see, for example, the results for case 14 using Hashin's criteria, Figure 4.23). It is possible that the convergence problems are due to a sharp drop in the response of the structure beyond the peak load. If this is indeed the case, then it can be concluded that the Linde model is predicting the peak load and displacement in better agreement with C07 when compared to the Hashin model. Figure 4.26 compares the responses from the Hashin and the Linde models for cases 10 (uniform mesh) and 14 (refined mesh), respectively. In both these cases, two elements are used in the thickness direction. Additionally, *in-situ* strengths and

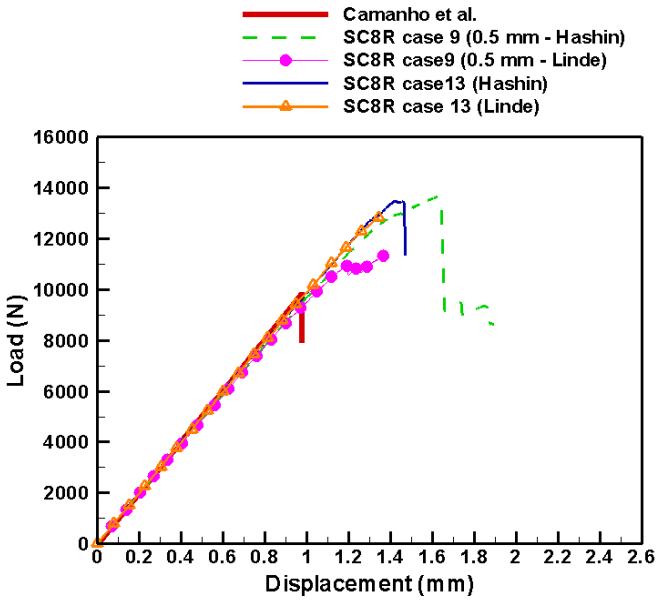

Figure 4.25: Load-displacement response comparing Hashin's criteria and Linde's model SC8R elements (uniform and refined mesh cases).

half the fiber fracture energy are used to define the damage response for the whole structure. From the figure we observe that the case 10 results with Hashin's criteria are, in relative terms, in better agreement with C07. Most of the simulations using Linde's model failed to converge. As it turns out, Linde's model with SC8R elements converged only with the unidirectional ply properties (cases 7 and 12). The load at which the analysis for cases 9 and 10 fails is almost the same. This suggests that, as observed earlier with S4R elements (Figure 4.17), the peak load and displacement are not mesh sensitive with Linde's model.

4.4.3 Parametric study using continuum solid elements

In this section, we revisit the plate with a hole problem, and obtain its response using solid continuum elements (element type C3D8R in ABAQUS). Hashin's criteria cannot be used directly with C3D8R elements because, as implemented in ABAQUS, these criteria assume the underlying element stress-state to be one of plane stress. Therefore, all simulations using solid continuum elements use Linde's model. The simulations for cases 7, 9, 10, and 11 are carried out by replacing the SC8R elements with C3D8R elements. In case 7, the unidirectional ply properties are considered,

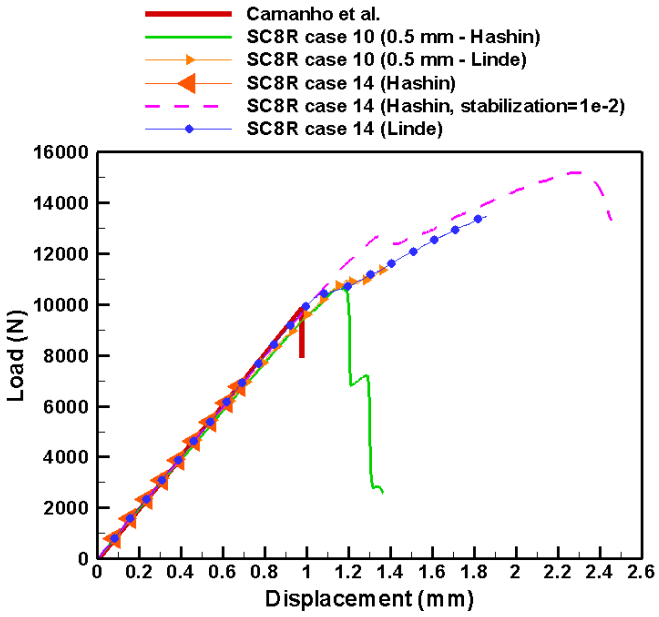

Figure 4.26: Load-displacement response comparing Hashin's criteria and Linde's model SC8R elements (uniform and refined mesh cases).

with full magnitude of the fiber fracture energy ($89.8N/mm$). Case 9 considers the *in-situ* strengths of the ply with only half the fiber fracture energy ($45N/mm$). In both the aforementioned cases only 1 element through the thickness is considered. Case 10 and 11 are similar to case 9 except that 2 and 5 elements, respectively, are considered in the thickness direction.

Figure 4.27 shows the responses obtained using C3D8R elements for the cases mentioned above. It can be observed that with unidirectional ply properties (case1, 4, 7 and 12) the slope diverges from the results of C07, a behavior that is consistent with that observed earlier with S4R and SC8R elements. The slope agrees better with C07 when the *in-situ* strengths are used (case 3, 6, 9, 13 and 14). The peak load is closer to the peak load in C07 for case 10 (with two elements through the thickness). Figure 4.28 shows a comparison of the results using C3D8R elements with those using S4R elements (the latter from case 3, uniform mesh with *in-situ* strengths and half the fiber fracture energy). The peak load obtained from C3D8R elements is higher compared to the peak load of S4R elements.

Finally, a comparison of the responses using S4R, SC8R, and C3D8R elements is

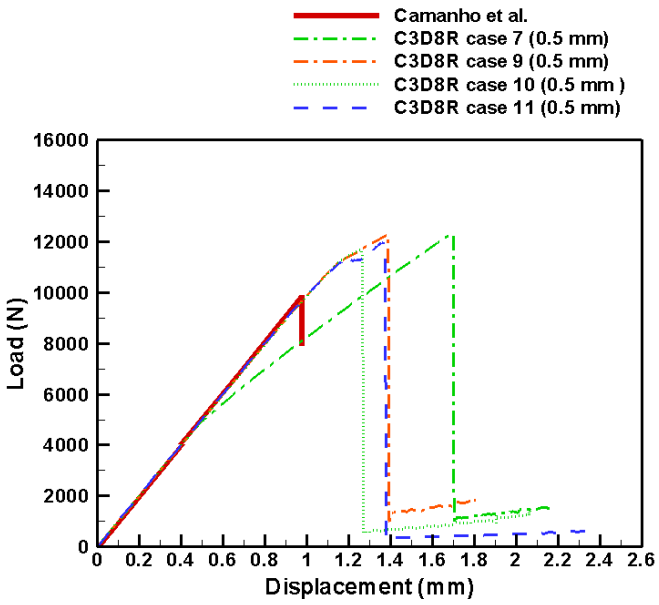

Figure 4.27: Load-displacement response using C3D8R elements (uniform mesh) with Linde's model.

made in Figure 4.29. The response from the 3 different element types can be compared only for the case with unidirectional ply properties. The finite element simulations for the SC8R element cases with Linde's model did not converge for cases 9, 10 and 11. Therefore, a direct comparison of the simulations with SC8R and C3D8R elements cannot be made. We observe that the responses with the SC8R and C3D8R elements predict a higher peak load and displacement compared to that with S4R elements, but the slopes for the responses with SC8R and C3D8R elements are in good agreement.

4.5 Conclusions

In this chapter we have carried out finite element simulations of the problem of tensile loading of a composite laminated plate with a hole. The constitutive response of the individual plies in the laminate is modeled using orthotropic elasticity, along with a progressive damage model that considers a number of different modes of failure in the matrix and the fibers. The progressive damage model utilizes a set of damage initiation criteria based on models developed by Hashin and Linde, respectively, and a progressive damage evolution law that is driven by a separate fracture energy and

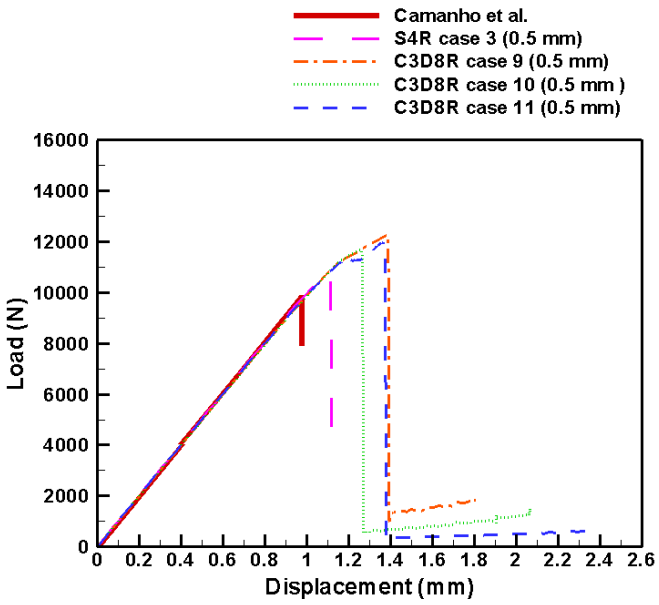

Figure 4.28: Load-displacement response, comparing C3D8R elements with S4R (uniform mesh) with Linde's model.

a linear softening response for each mode. Parametric studies were carried out to understand the effects of different modeling paradigms on the global load-displacement response of the structure. While the original objective of the study presented in this chapter was to ascertain the optimum element size for the accurate capture of intralaminar damage mechanisms, the observed results have been enlightening in their own right and have provided avenues for further research.

The results suggest that the peak load and displacement are not captured accurately with a linear softening damage evolution law. In the absence of an exponential softening law, an ad hoc reduction of the fiber fracture energy by a factor of two appears to lead to a global response that is closer to experiments. Previous studies [67] have observed that Hashin's failure criteria for unidirectional laminates can also be used to model the progressive failure behavior of laminates using *in-situ* strengths. The observations made in this study complement those from previous studies. It is observed from our simulations that the *in-situ* strengths play an important role in accurately capturing the slope of the load-displacement response. The simulations

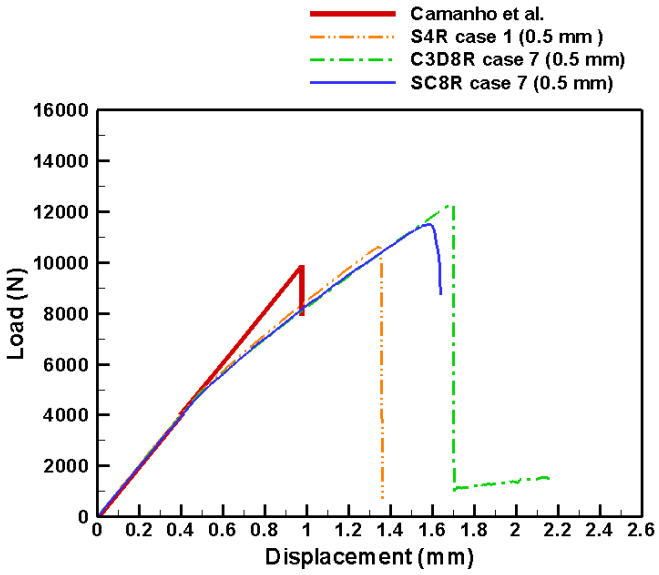

Figure 4.29: Load-displacement response, comparing S4R, SC8R and C3D8R elements (uniform mesh) with Linde's model.

using Linde's model suggest that an exponential softening law with the full fiber fracture energy captures the response of the structure better than a linear softening law using half the fiber fracture energy.

In this investigation, we analyze three different element types; conventional shells (S4R in ABAQUS), continuum shells (SC8R in ABAQUS) and continuum solids (C3D8R in ABAQUS), to model the progressive damage behavior of the ply. The key observations made by using conventional shells are as follows: using Hashin's criteria, the uniform mesh cases (0.5 mm and 0.25 mm element size) with the *in-situ* strengths and half the fiber fracture energy, predicted a peak load close to each other (less than, approximately 3% difference in magnitudes). However, the refined mesh case with the *in-situ* strengths and half fiber fracture energy predicted, approximately 12% lower peak load compared to the unifrom mesh case, and much closer to the peak load from C07. Using Linde's model, the peak load and displacements predicted were almost the same for both the uniform and refined mesh cases. Thus, the results obtained from Hashin's criteria appears to be sensitive to the mesh discretization, even though the characteristic element length is taken into account.

The study using continuum shell elements (SC8R) suggest that the in-plane mesh size of 0.5 *mm* and 0.25 *mm* did not show any significant discrepancies. But a significant change in the peak load and displacement was observed by using more than one element along the thickness direction. The response using two and five elements through the thickness seems to be very close to each other. Therefore, to capture the intralaminar and interlaminar damage behavior using continuum shells, at least two elements should be used in the thickness direction if the composite shell section definition (within ABAQUS) is utilized.

A comparison of all three element types was made for the case in which the unidirectional properties were defined. The conventional shells seems to predict a load-displacement value closer to the results from C07. The slope of the response (the part of the load-displacement curve that deviates from C07 when the unidirectional properties are used) obtained using the continuum shells and solids (SC8R & C3D8R) matched well with each other, while the conventional shells predicted a marginally higher slope compared to the aforementioned element types.

The continuum shell elements resemble the three-dimensional solid elements, and discretize the entire three-dimensional geometry. The formulation of these elements is such that their kinematic and constitutive behavior is similar to the conventional shell elements, as mentioned in Chapter 3. The continuum shell elements are also more accurate in contact modeling [1] compared to conventional shells. Contact is an important aspect to consider in the modeling of both intralaminar and interlaminar damage behavior of composites. By using two or more continuum shell elements in the thickness direction, the results (peak load, displacement and slope) matched well with the conventional shell element type. Thus, based on these observations, our original approach of modeling each ply with a single continuum shell element (as described in Chapter 3) seems reasonable. In the next chapter, we present the results obtained from the study of the combined intralaminar and interlaminar damage behavior of fiber reinforced composite materials.

CHAPTER 5: RESULTS AND DISCUSSIONS

In this chapter a detailed study of a fracture problem, that involves both intralaminar and interlaminar damage mechanisms in a laminated composite material, is presented. To this end we have selected, as outlined in Chapter 3, the problem of tensile loading of a composite plate with a slit at the center. The intralaminar damage mechanisms are simulated using the progressive damage framework discussed in Chapter 4, and utilizes both the Hashin and the Linde damage models. The interlaminar damage mechanism, on the other hand, is modeled using a cohesive zone framework (see Chapter 3 for details). The present chapter is arranged as follows. We begin with a brief analysis to determine the critical element size for the cohesive zone between the individual plies in the laminate , and also discuss the effects of a coarse versus a refined mesh in the cohesive zone. This is followed by detailed discussion of the results from our simulations using the Hashin model and the Linde model, respectively. The chapter concludes with a summary of some of the key characteristics of the damage mechanisms in a composite laminate, as observed from the simulations presented in this thesis.

5.1 Cohesive Region Mesh Size

In Chapter 4, a detailed parametric study was carried out to determine the optimum in-plane size of the finite elements that is needed to capture intralaminar damage mechanisms. The results from the former study will provide guidance towards selecting a good mesh for the individual plies in the next phase of the work that is presented in this chapter. Likewise, it is also important to ensure that the mesh size in the cohesive region is capable of capturing the interlaminar damage behavior (delamination) accurately. This section outlines the procedure we use to determine the optimum mesh size in the cohesive zone. To this end, we must first determine the length of the cohesive zone which provides a rough measure of the physical length

scale over which delamination occurs. Specifically, the length of the cohesive zone is defined as the distance between the crack tip (corresponds to the first cohesive element that has completely failed) and the point ahead of the crack tip at which the traction is maximum [85] as shown in Figure 5.1. Following [93], the characteristic

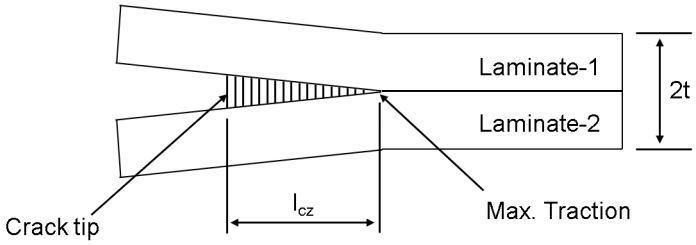

Figure 5.1: Length of the cohesive zone [85].

length of the cohesive zone may be estimated as:

$$l_{cz} = \left[\frac{G_c E'}{(\tau^0)^2}\right]^{1/4} (\frac{t}{2})^{3/4} \tag{5.1}$$

where l_{cz} is the length of the cohesive zone, G_c is the critical fracture energy, E' is the elastic modulus, τ^0 is the interfacial peak strength, and t is the ply thickness. For transversely isotropic materials E' is assumed to be the transverse modulus of the material, given by E_2. The length of the cohesive zone for Modes I, II & III can be determined by substituting the respective critical fracture energies and peak strengths in Equation 5.1. Based on the above calculations the number of elements, N_e, that must be placed in the cohesive zone is related to the cohesive element size, l_e, through the obvious relationship [85]:

$$N_e = \frac{l_{cz}}{l_e}. \tag{5.2}$$

Using Equation 5.1, the cohesive zone length for Modes I, II, & III are computed and tabulated in Table 5.1 for two different values of the ply thickness.

The length of the cohesive zone is the smallest in Mode I. Previous studies [85] and [6] have suggested that at least two to five elements are required in the cohesive

Table 5.1: Cohesive zone lengths for each mode.

Ply thickness (mm)	l_{cz} Mode I (mm)	l_{cz} Mode II (mm)	l_{cz} Mode III (mm)
0.5	0.397	1.270	1.270
1.0	0.667	1.804	1.804

region to capture the crack growth, for a pure Mode I case. A conservative approach in determining the appropriate mesh size in the cohesive zone would be to satisfy the mesh size requirement (of two to five elements in the cohesive zone) for Mode I. A choice of 0.25 mm for the cohesive element size would ensure that there are more than 2 elements in the cohesive region for a laminate with a ply thickness of 1 mm. Therefore, a uniform mesh size of 0.25 mm is used to discretize both the cohesive region and the plies. A few simulations with fewer than two elements in the cohesive region were also carried out. In the discussion to follow, the results from these simulations will be compared with results from simulations with more than two elements in the cohesive zone.

5.2 Prediction of Intralaminar and Interlaminar Damage Mechanisms

For the rest of this chapter, the term *evolution* will be used to refer to the situation in which the damage initiation criteria for a particular damage mode (Equation 3.1 - 3.4, 3.9, 3.13, and 3.19 from Chapter 3) has been met, and the damage variable corresponding to that mode begins to evolve. The damage variable for each mode evolves from an initial magnitude of 0.0, which signifies no damage, to a final value of 1.0, which signifies a complete loss of stress carrying capacity. When an element is fully damaged (as opposed to fully damaged in a certain mode only), we assume that all possible damage mechanisms (i.e., splitting, TPC, and delamination) have completely propagated. It may be noted that in the discussion to follow, the word crack generally refers to a "smeared crack" as opposed to a discrete one.

5.2.1 Results using Hashin's criteria

In the following paragraphs, the results presented are from a model with a $[90/0]_s$ ply orientation and with a ply thickness of 1 mm. As outlined in the previous section, an uniform element size of 0.25 mm is assumed for modeling both the plies (refers to

the in-plane element size only) as well as the cohesive region.

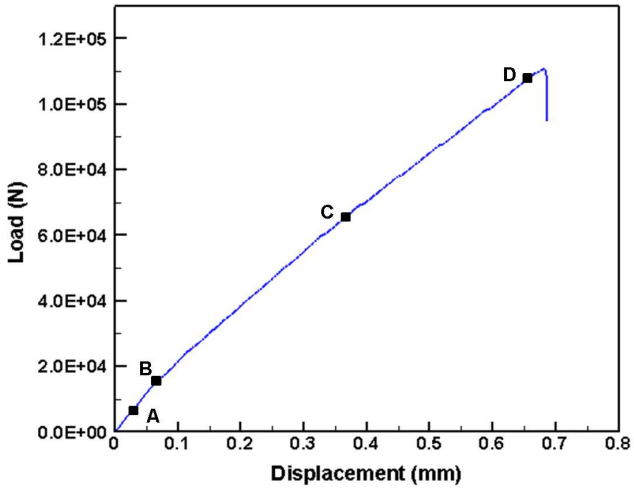

Figure 5.2: Load-displacement response using Hashin's criteria.

Figure 5.2 shows the load-displacement response for the structure referenced above. The points A, B, C, and D refer to the instant in the deformation history of the structure at which one of the initiation criteria is first met, and the corresponding damage variable starts evolving (from 0.0 toward 1.0). Point A corresponds to the initiation of damage in the cohesive region, which is observed to occur before any other mode of damage. This is followed by the initiation of matrix damage in tension, or what we will refer to as splitting, in the 0° ply, and is denoted by point B. The evolution of splitting extends through the thickness of the plies and is observed in the 90° plies as well (at point B). The initiation of TPC (matrix damage in tension in the 90° ply) begins at a much later stage, and corresponds to point C in the figure. Finally, point D corresponds to the initiation and subsequent evolution of damage in the fibers of the 0° ply, which eventually leads to the final catastrophic failure of the laminate (the latter corresponds to the sharp drop in the load-displacement response). Details and visual results showing the progression of all the different damage modes will be discussed in the rest of this chapter.

Figure 5.3 shows contour plots of the levels of damage (as quantified by the output variable, SDEG, in ABAQUS) in the cohesive zone between the 90° and 0° plies at different points in the deformation history of the laminate. It may also be noted

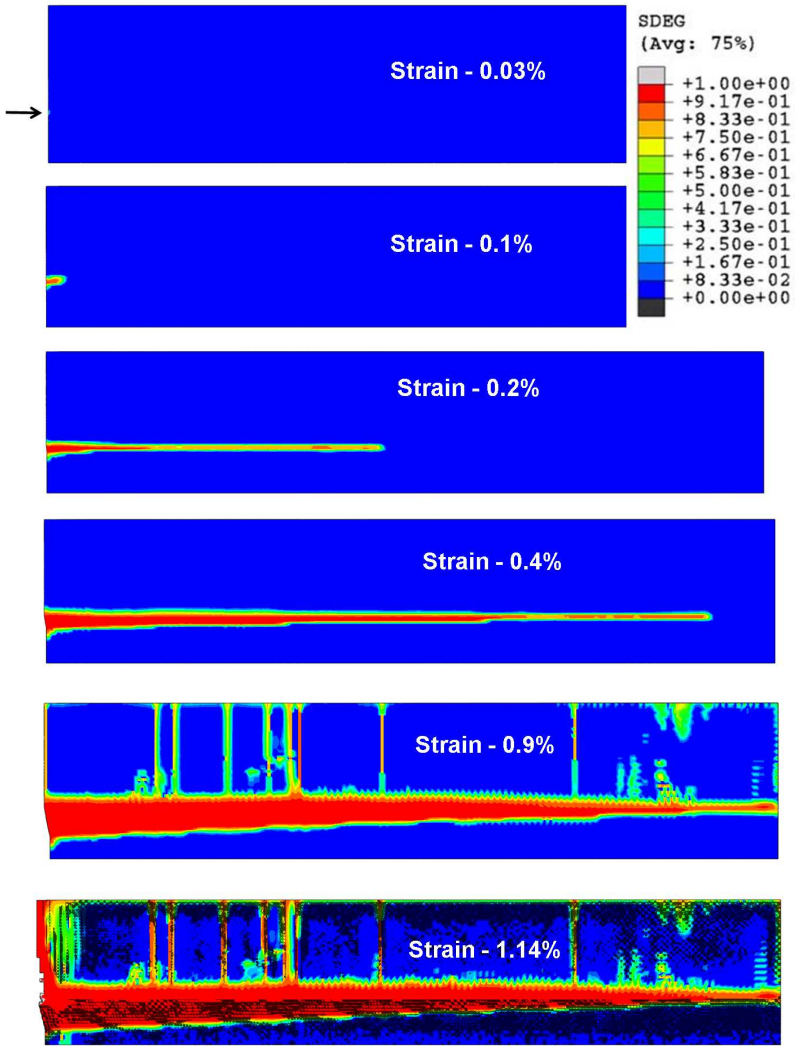

Figure 5.3: Progression of damage in the cohesive region at the 0/90 interface.

that the model does not include a cohesive zone at the symmetry boundary between the two 0° plies at the middle of the laminate. We have made this simplification based on our experience with full (in the thickness direction) models that showed no delamination between plies with like orientation. The damage in the cohesive zone initiates at the tip of the slit, as pointed out by the arrow in Figure 5.3. Damage begins at a very early stage, at a global strain of 0.03%, and the effects are initially limited to a single element in this region. The value of the damage variable in this element reaches a value of 0.92 at 0.1% strain. With further loading, the evolution of the damage zone in the cohesive layer follows a path that is along the direction

of the splitting crack occurring in the 0° and 90° plies. However, the magnitude of the damage variable in this element does not increase at the same rate with further loading. When the global nominal strain reaches 0.9%, the damage variable increases beyond 0.92. It appears that the increase in the damage variable in the cohesive zone may be related to the initiation and growth of TPC in the 90° plies. Finally, at 1.14% nominal strain the magnitude of the damage variable in some elements near the slit reaches a value of 1. The elements that have completely lost their load bearing capability are removed from the analysis by default, except when they are in a state of compression at the instant the damage variable reaches a value of 1. The elements that are eventually removed (observed around 1.14% strain in Figure 5.3) are along the ply interface in a region where fiber damage initiates in the neighboring 0° ply (point D in Figure 5.2).

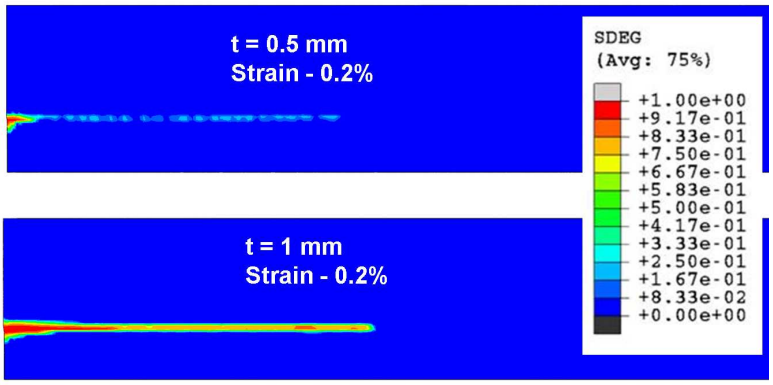

Figure 5.4: Effect of considering more than 2 elements in the cohesive region.

The shape of the zone in which delamination progresses is qualitatively consistent with the numerical results obtained by Yang and Cox [93]. Also, the triangular shape that characterizes the zone in which progressive delamination occurs is also consistent with experimental observations [71]. However, the results suggest that even though the cohesive elements in the interface zone show a propensity to fail pretty early on in the deformation history of the structure, they do not quite undergo complete failure till the occurrence of the final failure of the laminate.

Figure 5.4 shows the evolution of delamination for plies with thickness of 0.5 mm

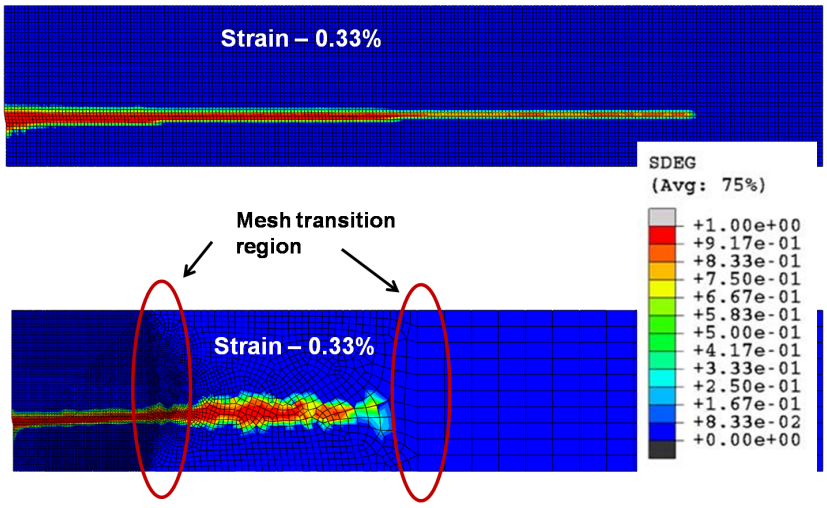

Figure 5.5: Comparison of the state of damage in the cohesive region for varying in-plane mesh sizes for a 1 mm thick ply.

and 1 mm, respectively. All other factors remaining the same, the length of the cohesive zone for each value of the ply thickness is tabulated in Table 5.1. A uniform mesh with an element size of 0.25 mm results in *less* between one and two elements (as before, for Mode I) in the cohesive region for a ply of 0.5 mm thickness. As discussed earlier, for a ply of 1 mm thickness the number of elements in the cohesive region is in between two to three elements. Thus, the two parts of the above figure correspond to cases with fewer than two cohesive elements and more than two cohesive elements, respectively, in the cohesive zone. It can be observed from the figure that the propagation of delamination is not captured well with fewer than two elements in the cohesive zone.

We have also carried out additional simulations for a non-uniform mesh that is very fine near the slit and coarser away from it. This refinement is applied to the entire model (both cohesive elements and continuum elements). The mesh size close to the slit is 0.1 mm. This results in approximately six to seven elements (corresponding to length of the cohesive zone under Mode I conditions) in the cohesive zone, as compared to the uniform mesh case, that resulted between two to three elements. Figure 5.5 shows a comparison of the state of damage in the cohesive elements between the simulations with an uniform and a refined mesh, respectively, and at 0.2% nominal

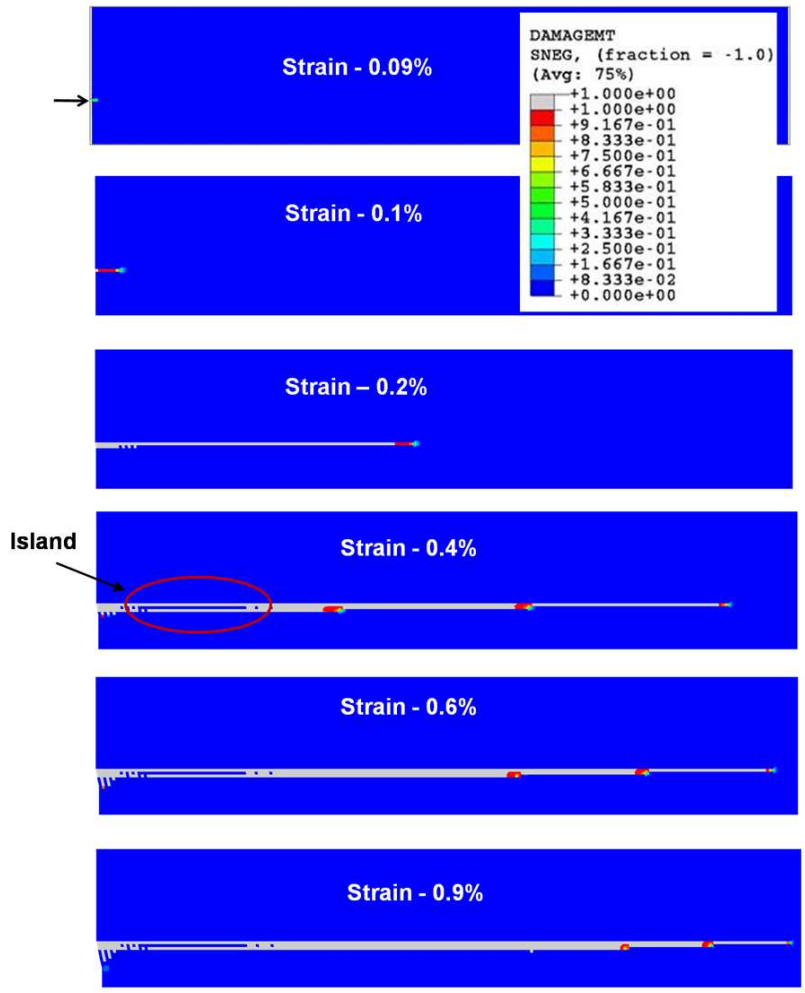

Figure 5.6: Progression of the splitting crack in the 0^0 ply.

strain. The top half of the figure is for the case of the uniform mesh (0.25 mm), while the bottom half corresponds to the refined mesh. It can be observed that the shape of delamination is similar in both cases, except for the length of the delamination zone. In the cohesive region for the refined mesh, the delamination crack appears to grow along the irregular mesh lines in the mesh transition region and hence deviates from the apparent straight path associated with an uniform mesh. On the other hand, for the uniform mesh, the crack grows more or less along a straight path. The excess energy dissipation that is associated with a zigzag crack path might explain why the crack grows a shorter distance for the refined mesh case, although we do not have hard evidence (as could be obtained, for example, by comparing the total energy dissipated in the delamination zones for the two cases) to support this claim. We

note that even with a finer mesh, the cohesive elements do not fail completely.

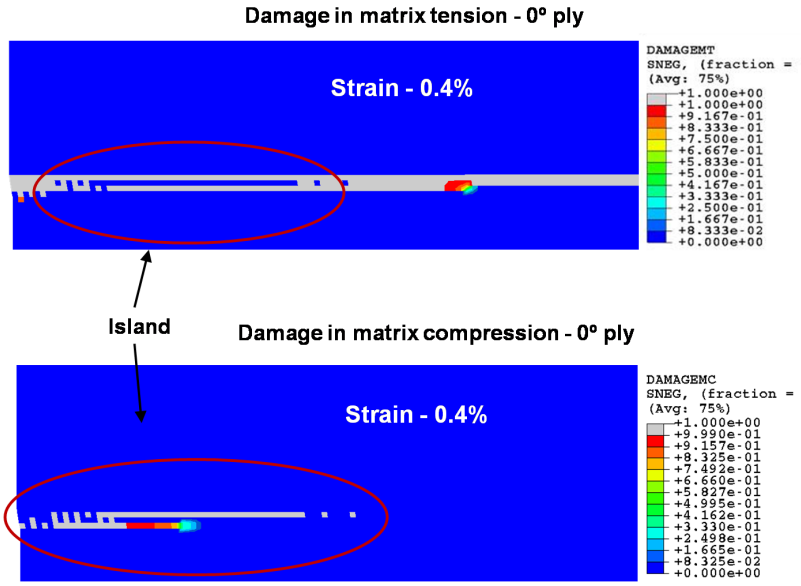

Figure 5.7: Zoomed in view of the *island*.

The splitting crack in the 0^0 ply also initiates at the slit, as indicated by the arrow in Figure 5.6. As pointed out earlier, we refer to the damage mode due to matrix tension along the fiber direction in the 0^0 ply as the splitting crack. The splitting crack also extends through the thickness of the ply in addition to its growth along the fiber direction. The location/orientation of the splitting crack at various stages during the deformation history is shown in Figure 5.6. The scales in the contour plot are such that the regions in gray correspond to full damage in the matrix tension mode, while the elements that are red are about 99% damaged. We observe that the splitting crack extends over almost the entire length. It can also be observed from the figure corresponding to 0.4% strain that a set of elements (shown in blue and referred to as *island* in the figure) in the wake of the splitting crack do not fail in the sense described above (i.e., they do not fail in the matrix tension damage mode). Interestingly, the elements in this island region are damaged due to matrix compression and not tension. Figure 5.7 shows a zoomed in view of the *island*. It can be clearly observed that the set of elements which did not fail in matrix tension, failed under the matix compression mode. The change in length of the splitting crack

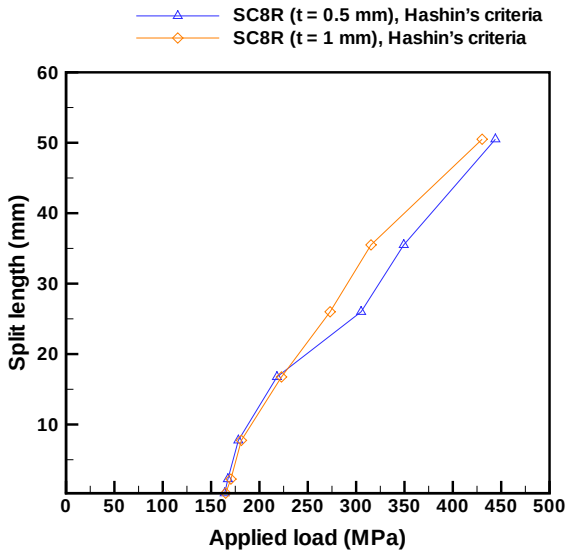

Figure 5.8: Comparison of the progression of split length in the 0^0 ply for a ply thickness of 0.5 mm and 1 mm.

with deformation suggests that the rate of growth of the split decreases after 0.4% strain, and the growth after 0.6% strain is almost negligible. Figure 5.8 shows a plot that compares the progression of the split length for two different values of the ply thickness. It is observed that the split initiates in the thicker ply at a marginally higher load initially. However, during the later stages of the deformation history, the rate of growth of the split is somewhat higher in the thicker ply. Previous experimental study [71] confirms this observation. For a refined mesh, the characteristics of the splitting crack were initially similar to those for the uniform mesh. However, with further deformation the split in the case of the refined mesh does not progress as much along the length as it did for the uniform mesh, similar to the behavior of the delamination crack as mentioned in the previous paragraph.

In addition to the splitting crack, transverse ply cracks (TPC) are also found to develop in the 90° ply, as can be seen in Figure 5.9 which represents a contour plot of the damage variable associated with matrix tension, but in the 90° ply. Damage in matrix tension along the fiber direction in the 90° plies is referred to as TPC. It is observed that TPC originate close to the slit and above the splitting crack. The TPC appear to initiate at about 0.58% strain. It is interesting to note that

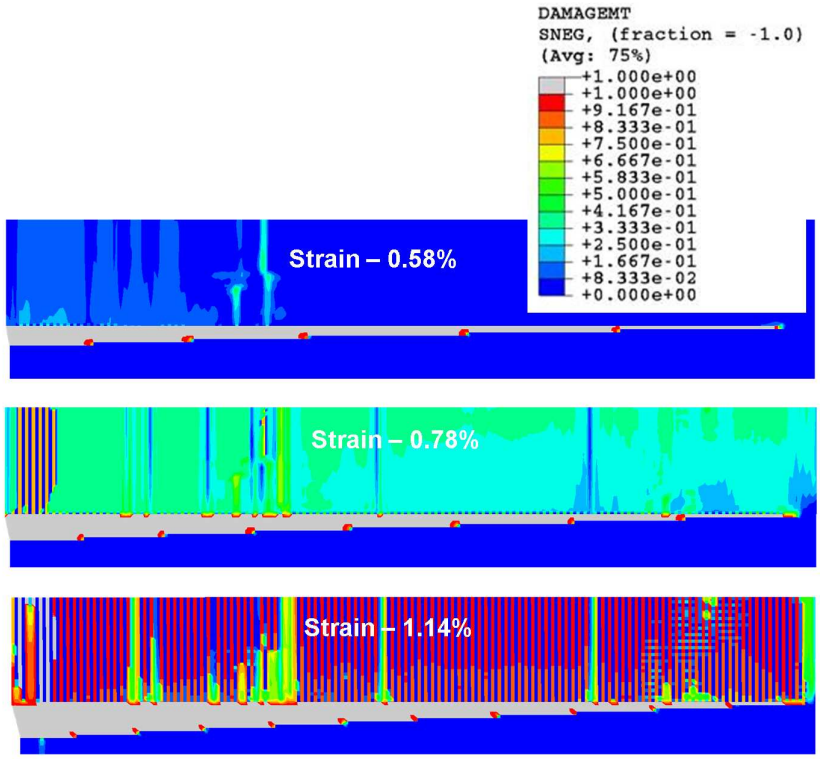

Figure 5.9: Progression of TPC in the 90° ply.

the growth of the splitting crack appears to be diminishing around this value of the applied nominal strain. This observation suggests that the splitting crack and the TPC damage mechanisms are competing in the sense that given a certain amount of available energy (supplied as external work through far-field loading), the TPC and splitting cannot progress at the same rate: any one mechanism proceeds, while the other subsides. We also observe that the TPC span the entire length of the 90° ply. These can be seen in Figure 5.9 as the red and blue fringes which spread out over the entire length of the ply. This behavior is consistent with experimental observations reported in [71]. We also note that the TPC close to the slit are in a state of full damage (i.e., the damage variable for matrix tension has reached a value of 1.0). The other TPC are in a state of partial damage, although in most cases the damage variable is fairly close to 1.0. It may also be noted that the model with a refined mesh did not complete, and failed to converge beyond 0.3% strain. The growth of TPC, which appears to occur at a later stage, was thus not observed in the refined mesh case.

Figure 5.10: Damage of fibers in the 0° ply.

The final catastrophic failure in the laminate occurs due to fiber failure. The load-displacement plot (Figure 5.2) shows that final failure occurs at a displacement of approximately 0.68 mm, which corresponds to a nominal strain of about 1.14%. The fiber damage mode initiates right before the load drop, which corresponds to point D in Figure 5.2. It appears that the rate of damage growth in the fiber in the 0° ply is significantly higher compared to the corresponding rates of splitting and the TPC (in the 90° ply), in the sense that complete failure rapidly follows damage initiation. The location of fiber fracture is shown in Figure 5.10, which shows a contour plot of the damage variable corresponding to fiber damage in tension. A closer observation of the slit region (not apparent from Figure 5.10) reveals that damage initiates in the fibers in the region where the splitting zone in the matrix intersects with the zone of transverse ply cracks (in the matrix). The experimental results reported by [71] make similar observations as well. As pointed out earlier, the calculations for the refined mesh model failed to converge at a much earlier stage; hence the fiber failure mechanism was not captured in the refined mesh model.

As discussed in Chapter 3, the above models (both uniform mesh and refined mesh cases) use a single element for each ply in the thickness direction. In the following we show results for a model that uses two elements in the thickness direction for each ply. Figure 5.11 shows the load-displacement responses for the models with one and two elements per ply in the thickness direction. The plot shows that the

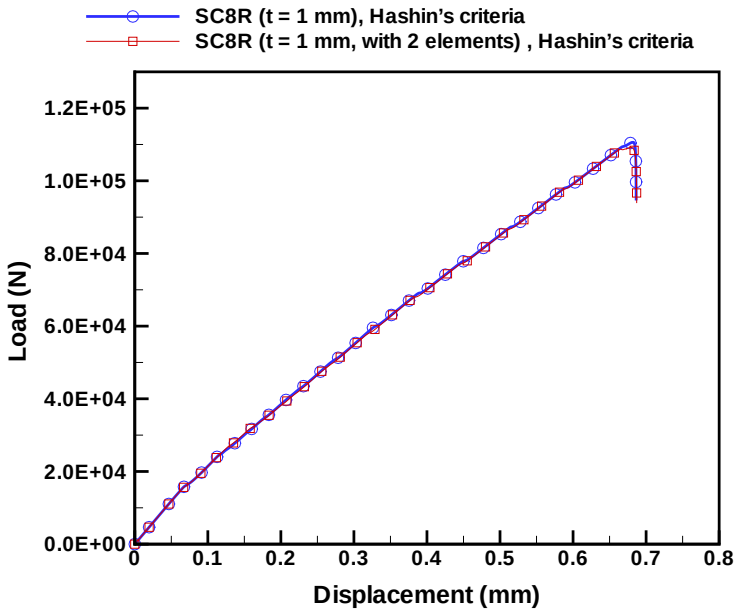

Figure 5.11: Load-displacement responses; comparison of results with a single element versus two elements per ply in the thickness direction.

load-displacement response is not affected by a finer discretization in the thickness direction. Figure 5.12 shows contour plots of the damage variables associated with all the pertinent damage modes in the structure: delamination, splitting, TPC, and fiber damage at the end of the analysis. The overall patterns of the contours for delamination, splitting, and the TPC are not very different between the cases of one versus two elements through the thickness. The only significant difference we observe between these two cases is the location of the fiber damage in the 0° ply (shown in Figure 5.12), which appears to be occurring roughly halfway between the slit and the region of far-field loading. This observation, while different from what we noticed with only one element through the thickness, is perhaps not too surprising in view of the experimental observations reported in [71]. The aforementioned authors noticed clusters of broken fibers in the 0° ply at various locations along the length of the split, and remarked on the connections between the locations of these broken fibers and the stress concentrations associated with the intersections of splitting cracks and the TPC. Additionally, we also observe from our results that the delamination damage mode

(0/90 interface) evolves simultaneously with the fiber damage mode in the 0° ply, and that the location of delamination coincides with the location of fiber damage in the 0° ply. Similar behavior has been observed in the model with one element per ply in the thickness direction, although, as pointed out above, at a different location (next to the slit). A case with three elements through the thickness was also investigated. The results were no different from the case with two elements through the thickness, except that the final load drop could not be captured due to non-convergence of the analysis. The location of the initiation of fiber damage was more or less in the same region as observed in the case with two elements through the thickness. The load-displacement response of the case with three elements through the thickness was exactly the same as the response obtained with one and two elements through the thickness, until the point at which the analysis failed.

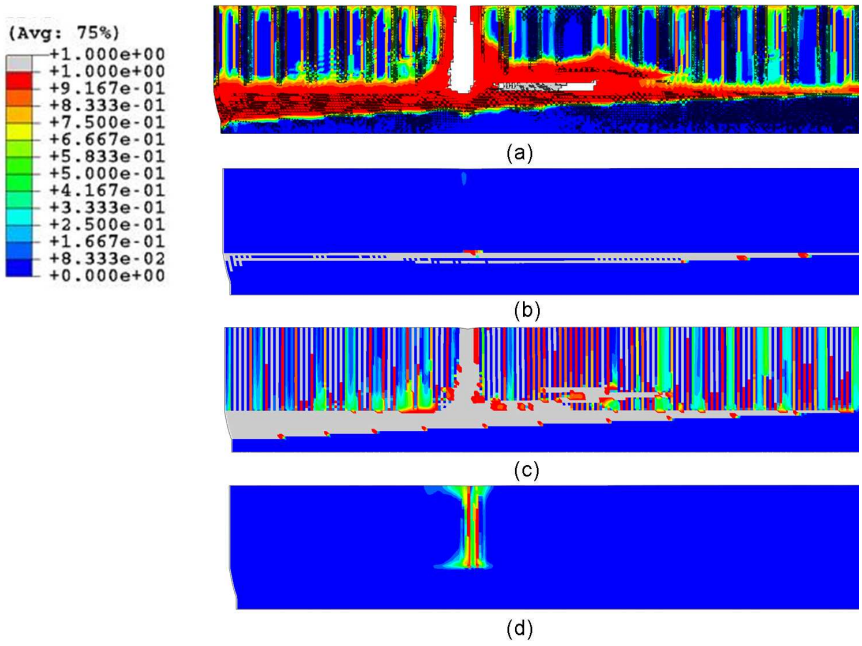

Figure 5.12: Contour plot of the damage mechanisms at 1.14% strain, (a) delamination, (b) splitting in the 0° ply, (c) TPC in the 90° ply, and (d) fiber damage in the 0° ply.

In summary, we observe from our simulations that both the intralaminar and the interlaminar damage modes can be captured using the framework proposed in this

thesis. The interlaminar damage, or delamination, initiates early on in the deformation history. However, complete delamination (or complete loss of load carrying capacity at the interface) is not observed until almost the end of the deformation history, and appears to coincide with fiber fracture. Both splitting in the 0° ply and TPC in the 90° ply are captured using Hashin's criteria to describe the damage response of the plies, and the results appear to be consistent with experimental observations. The final failure of the laminate occurs due to the fiber failure in the 0° ply. The results with two and three elements per ply in the thickness direction did not alter the load-displacement response of the model obtained with a single element in the thickness direction, although the location of fiber fracture in this case is puzzling. In the next subsection we present results for the same problem, but using Linde's model to describe the damage response of the plies.

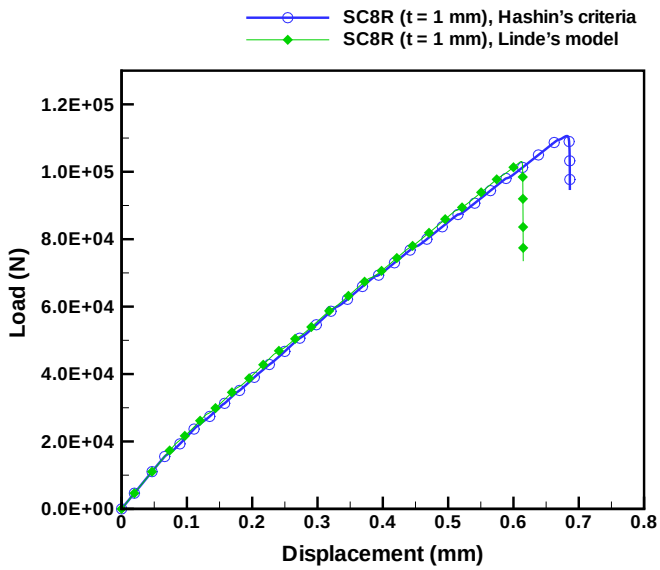

Figure 5.13: Comparison the load-displacement response for Hashin's criteria and Linde's model.

5.2.2 Results using Linde's model

In this section we discuss the results for a model that uses only one element per ply in the thickness direction. The model is uniformly meshed with an element size of 0.25 mm. The ply thickness is assumed to be 1 mm. Figure 5.13 shows the load-displacement responses comparing the Linde and the Hashin models for intralaminar

damage. Continuum shell elements (element type SC8R in ABAQUS) are used to model the plies. The slope of the curve obtained from both models are approximately the same. The peak load predicted using Linde's model is approximately 5% lower compared to the peak load predicted by Hashin's criteria. The damage mechanisms of splitting and delamination occur simultaneously much before the final failure. Recall that the investigation of only intralaminar damage mechanisms reported in Chapter 4 (albeit for a different composite configuration) also suggested that Linde's model predicts a lower peak load and displacement compared to Hashin's model. 5.14) near the slit.

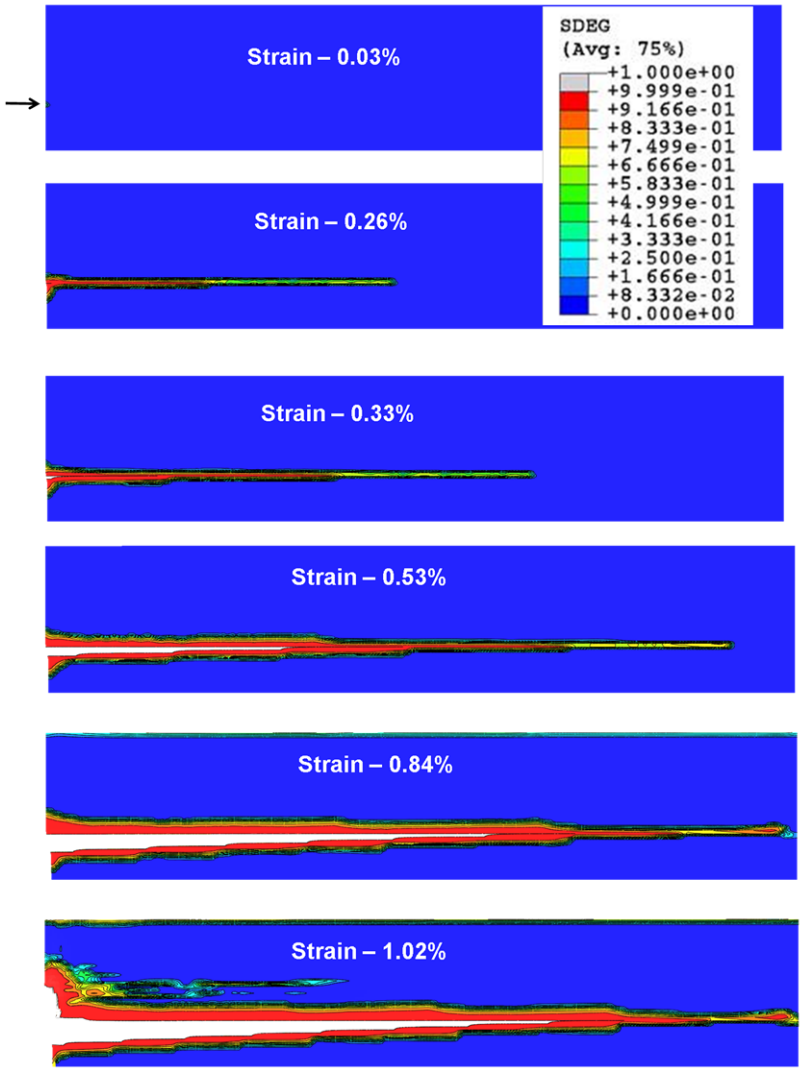

Figure 5.14: Progression of delamination using Linde's model (with SC8R elements).

Linde's model was also utilized to compare the results for the present problem under (i) the assumptions of plane stress (as is the case with continuum shell elements) and (ii) a fully three-dimensional stress state (to be simulated using solid continuum elements). Linde's model is made available with the released version of the software as a user-material [1]. The model can be used in both plane stress and three-dimensional stress states, unlike the Hashin's model which is also relevant in a state of plane stress. Figure 5.14 shows the progression of delamination from the simulations that assume plane stress conditions in the plies. The delamination damage mode initiates at approximately 0.03% nominal strain in a single element (indicated by arrow in Figure The load at which this particular damage mode initiates is the same as that observed earlier with Hashin's criteria. At 0.26% nominal strain the damage variable reaches a value of 1.0 at the first integration point of this element. Recall that in the earlier simulations using Hashin's criteria, complete failure (damage variable equals 1.0) in the cohesive zone was not observed until the fibers failed. The first evidence of total delamination of all the integration points in an element occurs at 0.33% strain, and the element is deleted. Delamination grows with further loading and at 0.53% strain a triangular-shaped damaged region can be observed in the cohesive layer below the splitting crack. At this point the delamination angle is computed based on the ratio of the height of the triangular region to its length. The height of the triangular region is measured based on the number of failed cohesive elements along the global y-direction. Likewise, the length of the triangular region is measured based on the number of failed cohesive elements along the global x-direction. The delamination angle at 0.53% nominal strain is approximately 5.4°. The delamination angle reduces to approximately 2.4° at 0.84% strain and remains the same thereafter till the end of the analysis. The experimental results reported in [71] predict a delamination angle of 4°. At 1.02% strain, delamination grows *above the location of the slit* forming a triangular shape. The term *above the location of the slit* refers to the region above the slit, toward the top edge of the rectangular geometry. We will be referring to this term in the following paragraphs to describe the growth of delamination.

The progression of the splitting crack from the present simulation is shown in

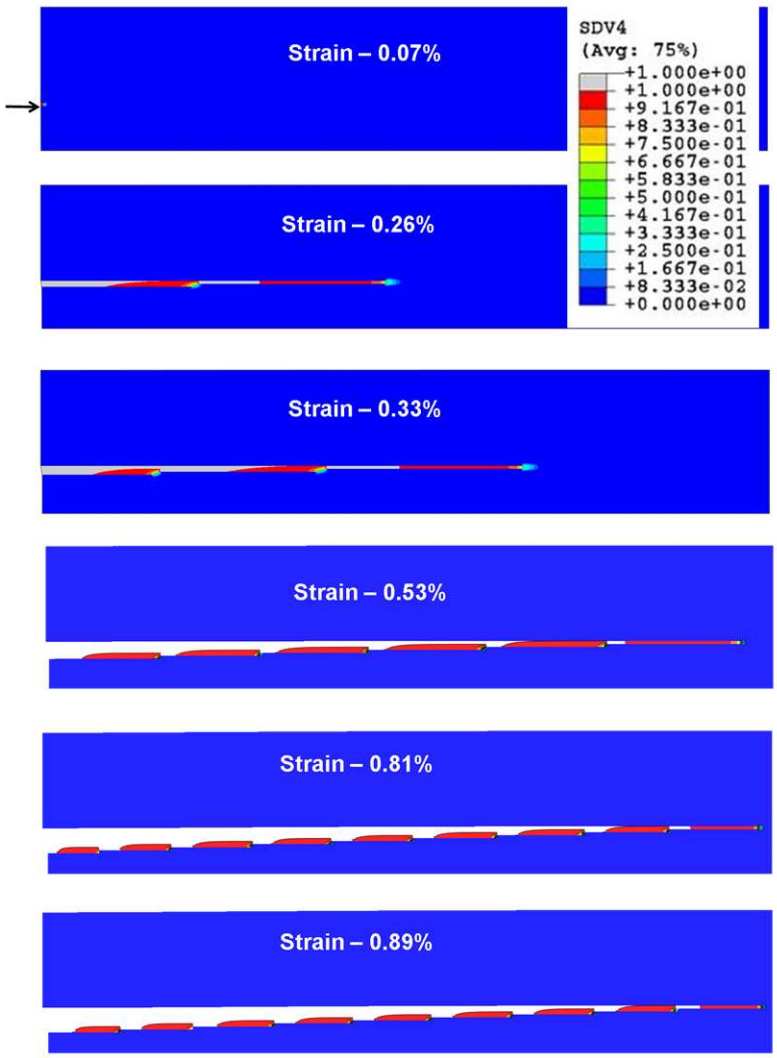

Figure 5.15: Progression of splitting using Linde's model (with SC8R elements).

Figure 5.15. The initiation of splitting, as predicted using Linde's model, occurs at a slightly lower load (0.07% nominal strain) compared to the prediction from Hashin's model (0.09% nominal strain). In this case, multiple splitting cracks appear to be growing next to each other. The *island* in a state of matrix compression within the region of splitting (matrix tension) that was observed (Figure 5.7) earlier using Hashin's model are not observed in the present model. The growth of the splitting crack decreases after approximately 0.6% nominal strain, in a manner consistent with the earlier observations using Hashin's model.

The growth of TPC is not captured well by the present model. Figure 5.16 shows

a contour plot of the damage variable associated with matrix tension in the 0° ply, which signifies the progression of the TPC. The TPC initiates at approximately 0.48% nominal strain, at a slightly lower load compared to earlier results using Hashin's criteria (0.58% nominal strain). Even with further loading, the TPC do not develop to form the repeating pattern of fringes observed earlier from the results of the model using Hashin's criteria. This behavior needs further investigation.

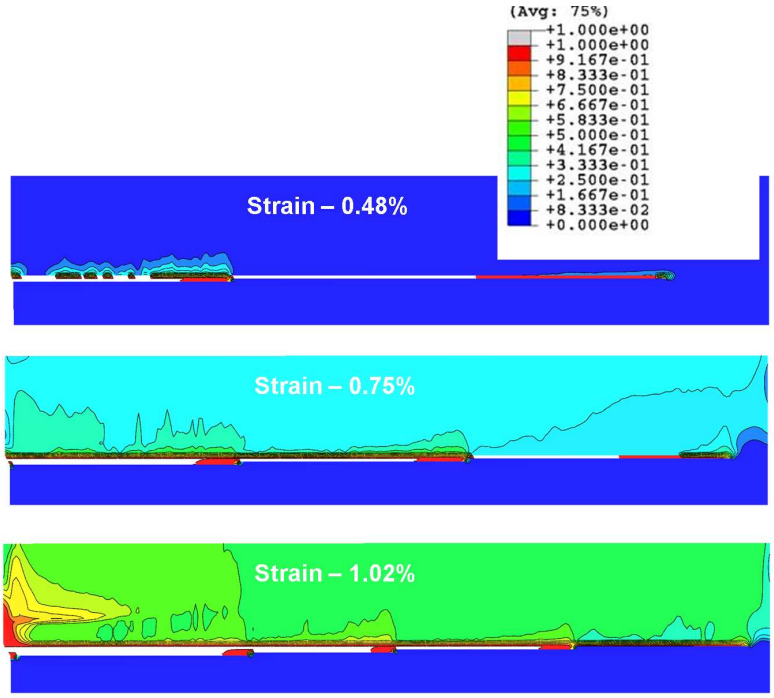

Figure 5.16: Progression of TPC, or lack thereof, using Linde's model.

The following is a summary of the observations based on the results obtained using Linde's model under the assumption that the plies are in a state of plane stress (SC8R elements). Delamination was observed to occur at 0.33% strain (Figure 5.14). At this nominal strain level, splitting had fully developed in the 0° ply (Figure 5.15). This suggests that delamination and the splitting crack develop simultaneously. It was also observed that at 1.02% nominal strain, delamination grows *above the location of the slit*. The fiber damage variable in the 0° ply reaches a value that is very close to 1.0, although it does not precisely reach 1.0. However, from an engineering point of view, we treat values of the damage variable that are in very close proximity to 1.0 (for example, values of 0.999 and higher) to signify full damage. This assumption is

further justified when we observe the sharp drop in the load-displacement response when the fiber damage variable reaches its peak value. At 1.02% nominal strain, we observe that the damage variable for matrix tension (TPC) in the 90° ply (Figure 5.16) is close to 0.999 i.e., not quite reached the assumed final damaged state of 0.999. In the next few paragraphs, we present the results obtained using Linde's model under the assumption of a three-dimensional stress state in the plies.

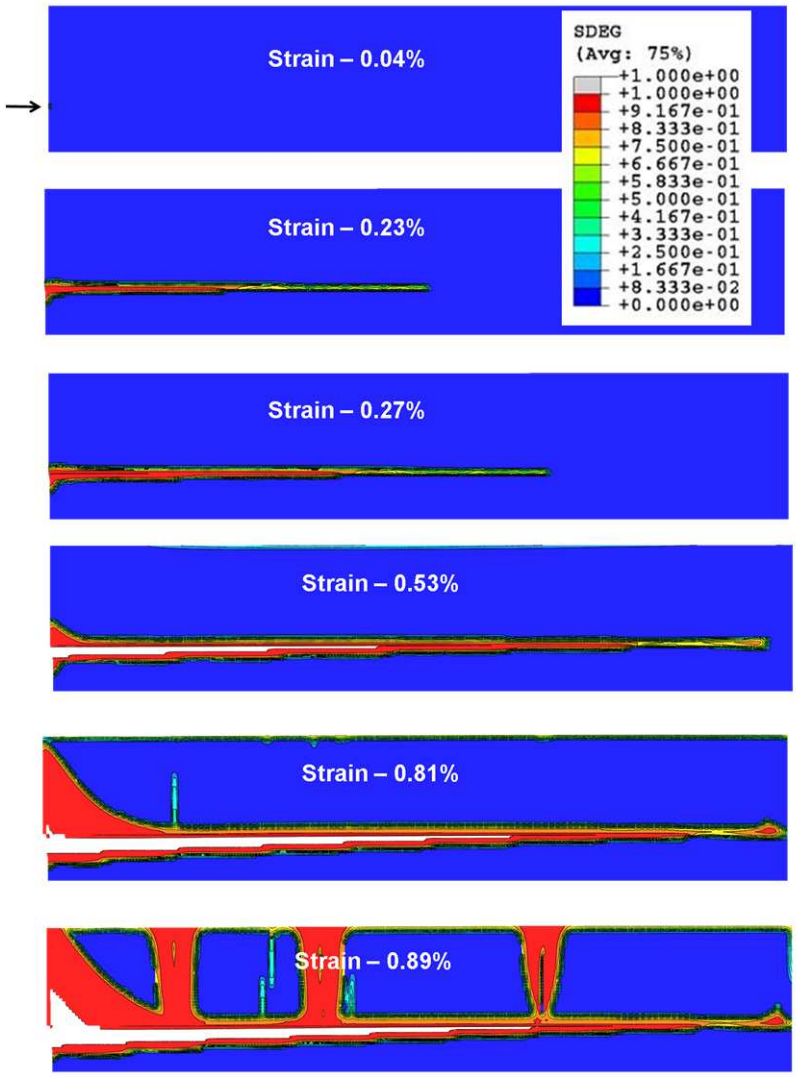

Figure 5.17: Progression of delamination using Linde's model with solid continuum elements (C3D8R).

Figure 5.17 shows the contour plots of the damage variable corresponding to delamination, occurring under the assumption of a fully three-dimensional stress state

in the plies (solid continuum element type, C3D8R, in ABAQUS is used), at various points in the deformation history. At 0.27% nominal strain, the value of the damage variable at all integration points in the element indicated by the arrow in the topmost part of Figure 5.17 is equal to 1.0. The evolution of delamination is similar to the predictions from the model using continuum shell elements. But the rate of delamination growth using solid elements appears to be somewhat higher compared to that using shell elements. At 0.81% strain, delamination begins to develop *above the location of the slit* in the case of solid elements. However, in the case of shell elements such extensive delamination is not observed at the same nominal strain. The profile of delamination at 0.89% nominal strain using solid elements is similar to the profile of delamination at 1.02% nominal strain using shell elements. The delamination angle at 0.53% strain is approximately 3.27°, while at the end of the analysis (i.e., at 0.89% strain), the angle reduced to approximately 3.03°.

The progression of the splitting crack in the simulation with solid elements is shown in Figure 5.18. It is observed that the growth rate and the profile of the splitting crack, predicted using Linde's model and obtained using shell and solid elements, respectively, to model the plies, agree well with each other.

Figure 5.19 shows the progression of the damage variable corresponding to matrix tension in the 90° ply. We used similar plots from our earlier simulations to understand the progression of TPC. The TPC appear to be captured somewhat better using solid elements compared to using shell elements, although the equally spaced fringe pattern observed using Hashin's criteria is not observed here. We note that the evolution of TPC begins at 0.51% strain. A few staggered cracks begin to form at 0.76% strain, but do not quite develop fully. The first fully developed TPC occurs in the vicinity of the slit at approximately 0.89% nominal strain.

In summary, Linde's model when used with solid continuum elements predict the onset and the growth of delamination at a somewhat smaller load compared to corresponding results using shell elements. The growth of delamination *above the location of the slit* is observed using both types of elements. The splitting crack is also captured for all cases, except that the model with solid elements predict the onset of

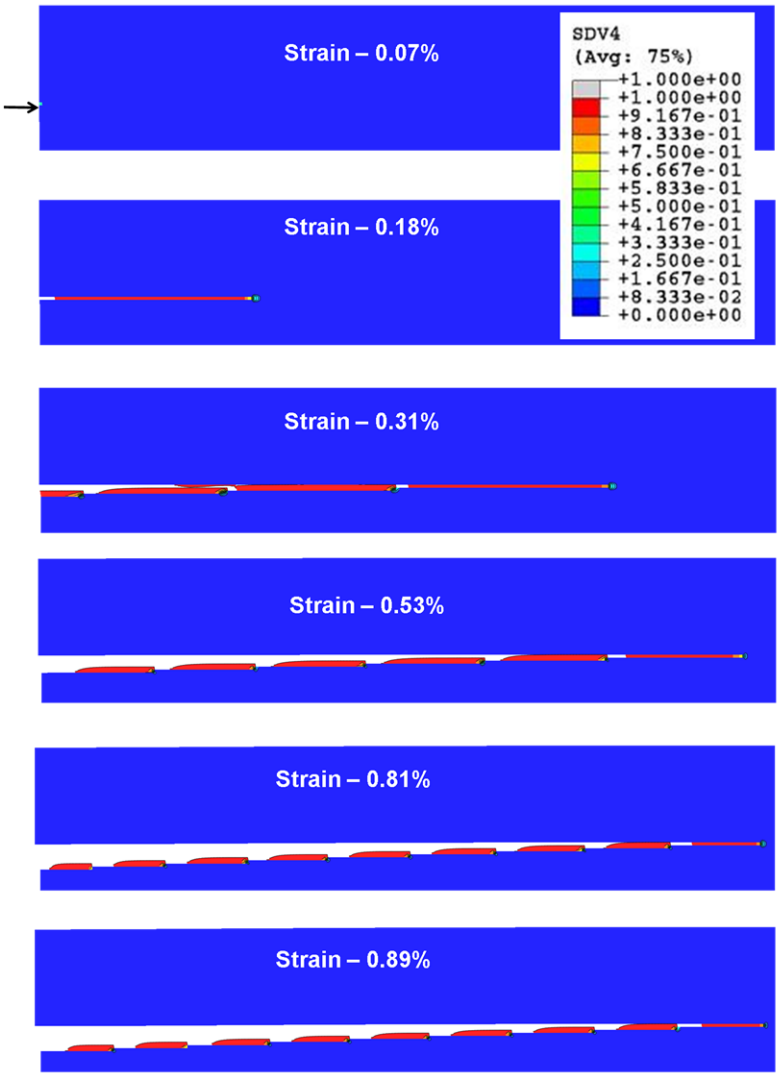

Figure 5.18: Progression of splitting crack using Linde's model and considering solid continuum elements (C3D8R).

splitting at a somewhat smaller load. The equally spaced fringe patterned TPC that were observed using Hashin's model are not observed in the simulations using Linde's model. It is unclear if the growth of delamination *above the location of the slit* (observed in cases using Linde's model), plays a role in suppressing the growth of TPC. In the model using Hashin's criteria, delamination had not developed *above the location of the slit* when TPC was observed. Further detailed investigation must be conducted to understand the relationship between the TPC and delamination.

Figure 5.20 compares the load versus split-length responses obtained using Hashin's criteria with shell elements with the corresponding results using Linde's model with

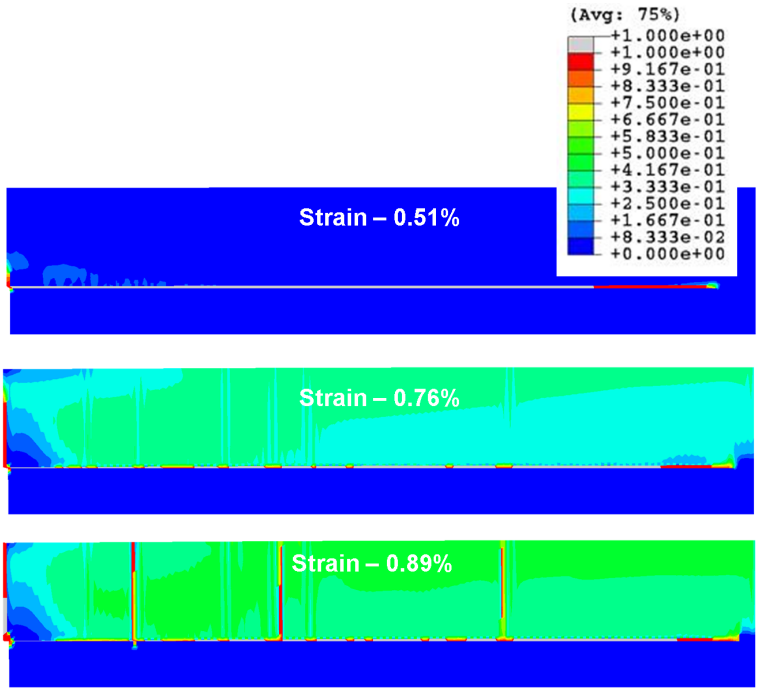

Figure 5.19: Progression of TPC using Linde's model and considering solid continuum elements (C3D8R).

both shell and solid elements. It can be observed that with shell elements, Linde's model predicts the onset of the splitting crack at a higher load compared to Hashin's model. The results from the simulation using solid elements with Linde's model predicts the onset of the splitting crack at a load that is closer to Hashin's criteria.

5.3 Characteristics of Intralaminar and Interlaminar Damage Mechanisms

In this section we look at the results presented earlier from a different point of view. To this end, the stress state in an element before and after the progression of damage is investigated in details. We consider an element close to the slit. The objective of this investigation is to determine the stress component that drives each of the damage mechanisms, and we use the results obtained using the Hashin's model. The stress components and the values of the different damage variables, as output by ABAQUS, are first noted. Using these values in Equation 3.5 (from Chapter 3), the effective stress components are determined. The effective stress components can be compared to the strengths of the ply in the different modes to determine which stress component drives each mode. The stress-state of an element in the 0^0 ply

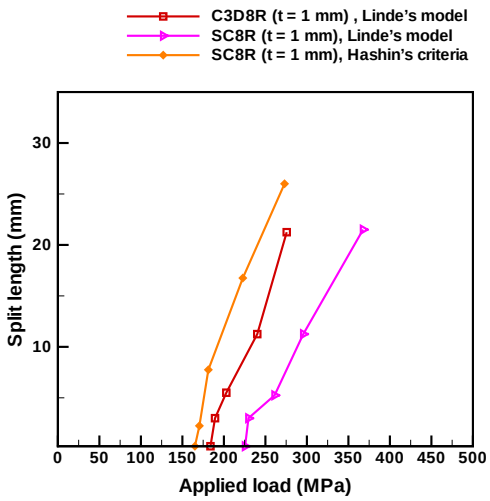

Figure 5.20: Comparison of split length versus applied load for the different element types, using Linde's model and Hashin's criteria.

suggests that the shear component ($\hat{\sigma}_{12}$) is the main contributor to the development and growth of the splitting crack. This observation is consistent with that of Yang and Cox [93]; these authors describe splitting cracks as shear driven as well. On the other hand the stresses in an element in the 90^0 ply suggest that the TPC is driven by the stress component in the local Y-direction ($\hat{\sigma}_{22}$).

In the cohesive region, the first (t_s, corresponds to the global 1-3 shear) and second shear (t_t, corresponds to the global 2-3 shear) components are the dominant stresses (i.e., the stress in the normal direction is negligible). In the model utilizing Hashin's criteria, two of the integration points are dominated by the first shear (t_s) component while the other two are dominated by the second shear (t_t) component. For the simulations using Linde's model, the integration point which fails first is dominated by both the shear components. The magnitudes of these shear stress components are more or less equal. The results generally suggest that combined shear loading is responsible for causing delamination.

Figure 5.21 compares the in-plane stresses in a solid element versus those in a shell element (both using Linde's model) at a nominal strain of 0.06% (corresponds to a load that is just below the load required for the initiation of matrix damage). It can

be observed that the magnitudes of the longitudinal, transverse, and the shear components of the stress are relatively close for both types of elements. The growth and propagation of splitting crack under plane stress conditions (using Linde's model with shell elements) and a fully three-dimensional stress state (using Linde's model with solid elements) are similar both qualitatively and quantitatively. Given the earlier observation that splitting is driven by the in-plane shear stress, it is not surprising that a full three-dimensional stress state (that also considers the out-of-plane stresses) does not appear to affect its growth and propagation. However, the out-of-plane stress state in the solid element could have influenced the early growth and progression of the delamination crack. Figure 5.22 shows contour plots of the 3-3, 1-3, and 2-3 components of the nominal stress tensor at 0.06% nominal strain (just before matrix damage initiates). The magnitude of the 2-3 component appears to be the least, with a maximum value of 0.6 MPa. The strength of the cohesive element in the thickness direction is 50 MPa. The magnitude of 3-3 stress component in the C3D8R element is approximately 9.02 MPa, which is about 18% of the maximum strength of the cohesive element in the normal direction. The only possible effect of the 3D stress state (Linde) could have been in the delamination growth rate which was observed to be higher compared to the plane stress state (Linde). In the next chapter, we present the the conclusions from this study and discuss future related avenues of research.

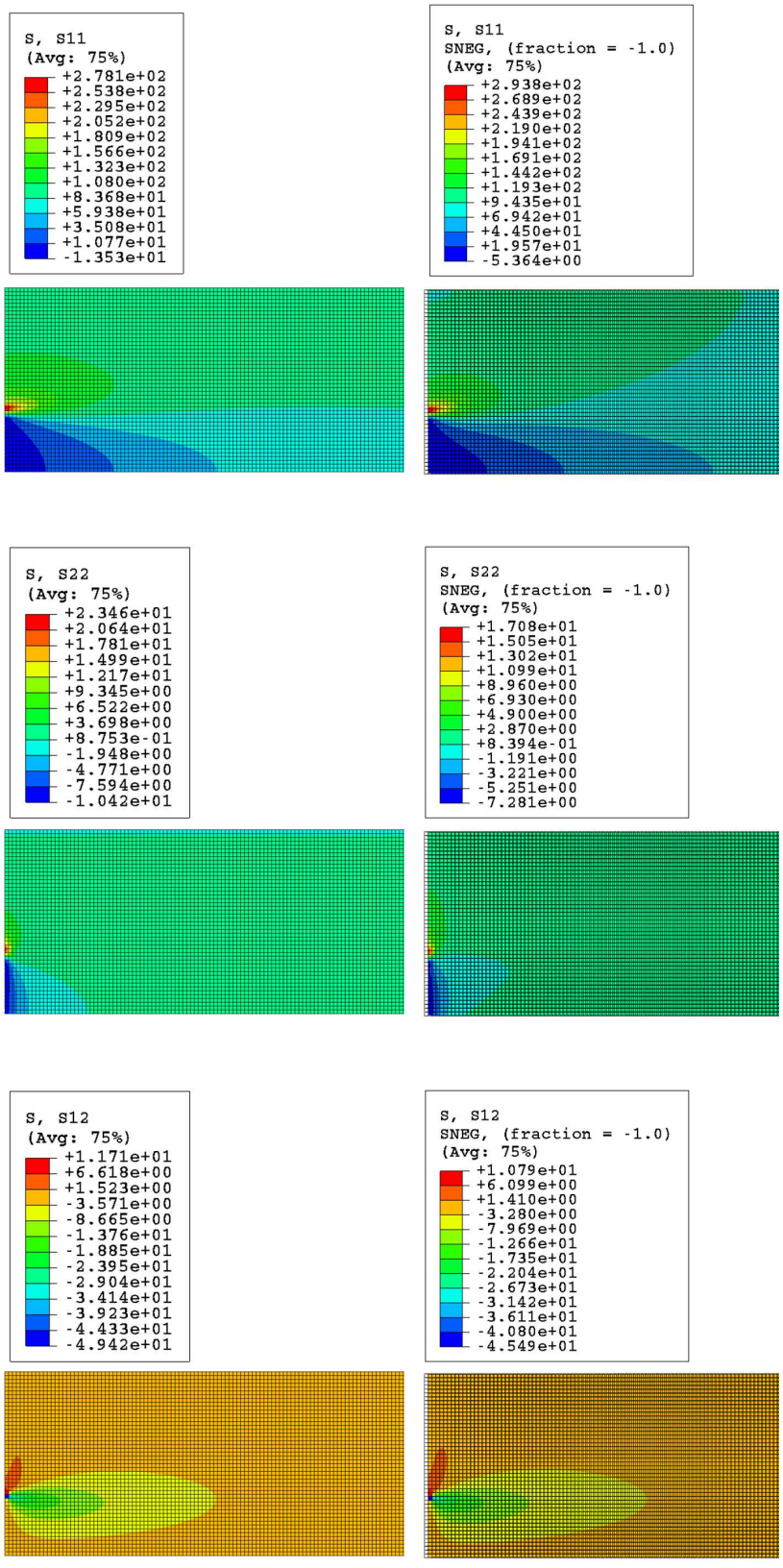

Figure 5.21: Comparison of stress states before damage evolution in models with C3D8R (left) and SC8R (right) elements.

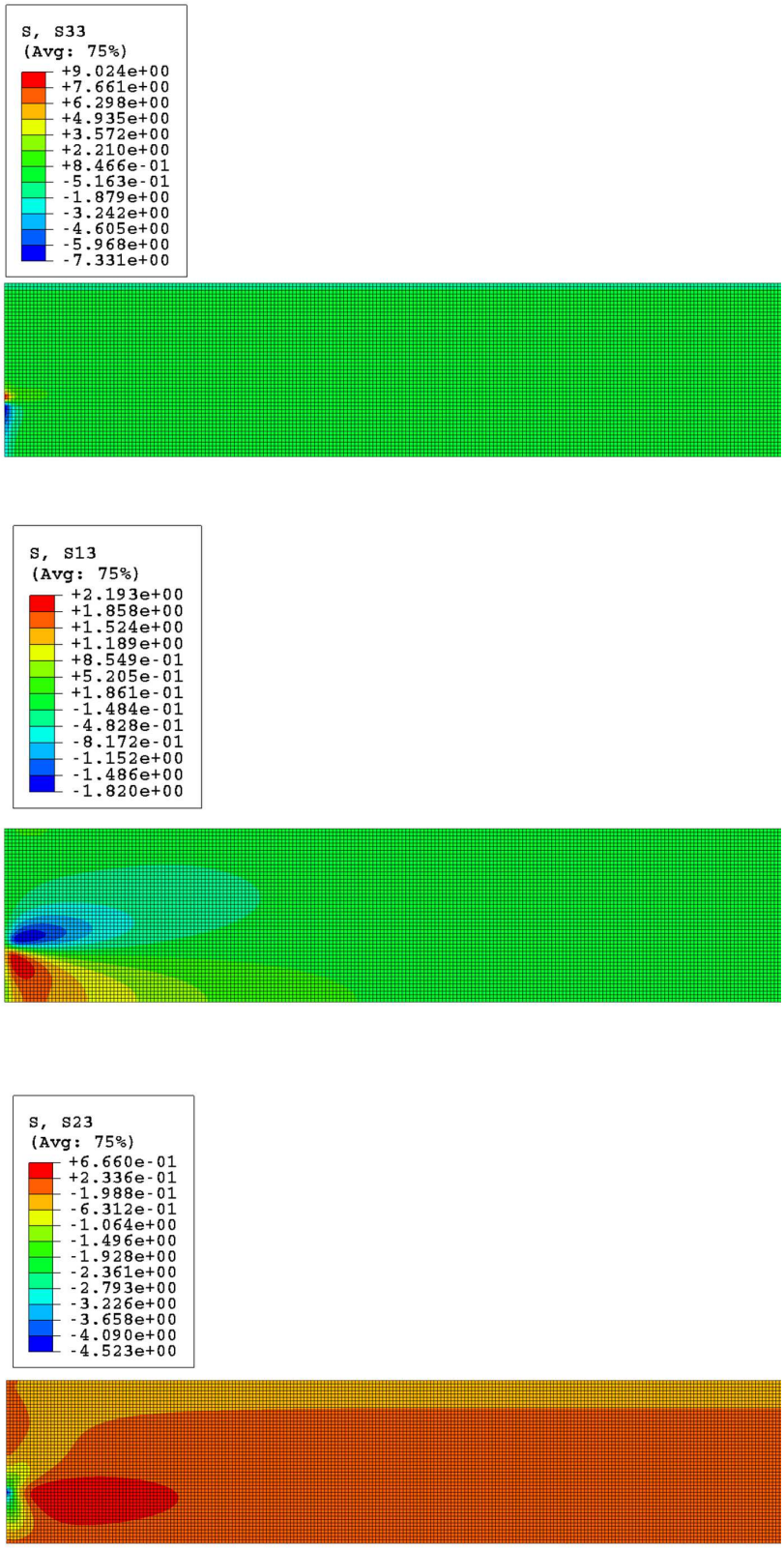

Figure 5.22: Contour plots of the out of plane stress state in the model with C3D8R elements.

CHAPTER 6: CONCLUSIONS AND FUTURE WORK

6.1 Conclusions

In the first part of this dissertation, we have focused on predicting the intralaminar (splitting and transverse ply cracks) and interlaminar (delamination) damage mechanisms in a fiber reinforced laminated composite subjected to a tensile loading. A rectangular laminate with a slit at the center is used for the study, and we have assumed a $[90/0]_s$ ply orientation. We assume transversely isotropic elastic behavior of the plies and model the different failure mechanisms using a progressive damage modeling framework where each individual damage mode is governed by a *damage initiation* criterion and a *progressive damage evolution law*. The criteria used to predict the initiation of damage is largely based on the Hashin's model which is a built-in model in the ABAQUS material library. We also carry out a set of simulations utilizing another set of initiation criteria developed by Linde, which is also available with the commercial release of ABAQUS as a user subroutine. The damage evolution in the plies is governed by the fracture energies and a linear softening response for each damage mode with Hashin's criteria, while Linde's model assumes an exponential softening behavior that is also fracture energy driven. The interface between the plies is modeled using the cohesive element framework in ABAQUS. The constitutive response of cohesive elements is governed by a traction-separation law that is characterized by a peak traction (interfacial strength) and a fracture energy (interfacial fracture toughness). Three-dimensional continuum shell elements (element type SC8R in ABAQUS) are used to discretize the plies. The results from these simulations are also compared with results from additional simulations using three-dimensional solid elements (element type C3D8R in ABAQUS). The results provide valuable insights on the effectiveness of: (i) the modeling methodology, (ii) the different mesh sizes of the ply and interface, (iii) the different damage models utilized in

this study, and (iv) the current overall capabilities of the commercial finite element software package ABAQUS in modeling the different failure mechanisms occurring in a fiber reinforced laminated composite material.

The splitting and delamination modes of failure were observed to occur in conjunction in previous experimental studies [71] and [30]. A number of numerical studies have been conducted by other researchers [41], [91], [30] and [93] to simultaneously capture the splitting and delamination modes of failure. In these studies, splitting was modeled by placing cohesive elements in the plies along the observed paths of splitting cracks from experimental studies. Thus, the location and the path of the splitting crack in each ply is assumed to be known. In situations where the exact path of the splitting crack is not known (perhaps due to lack of experimental data), such a methodology might not be very useful. In addition, modeling the deviation of splitting cracks from a predefined path would require essentially *sugar coating* the boundaries of all structural elements with cohesive elements. In this dissertation, we have modeled the splitting crack using the smeared crack approach inherent in a progressive damage modeling framework, without explicitly placing interface elements along predefined paths. Thus, prior knowledge of the location and path of splitting cracks is not necessary. In the following paragraphs, the primary observations from the present study will be outlined and compared with available experimental results as well as results from previous numerical studies by other research groups.

The results from the present study demonstrate that the initiation and growth of splitting cracks in the 0° ply and through the thickness in the 90° ply can be predicted based on an intralaminar progressive damage modeling framework, without explicitly modeling them by using interface elements. Using Hashin's criteria with shell elements to model the individual plies, we observe that the splitting crack initiates as early as 0.1% nominal strain. The crack initiates near the slit and propagates parallel to the fibers in the 0° ply, an observation that is consistent with experimental results [71]. As also observed in experiments ([71]), the splitting crack extends in the thickness direction through all the plies. The splitting crack grows all the way till about three-quarters of the length of the specimen and subsequently seems to be

arrested. On the other hand, the path of damage in the cohesive elements along the ply interface appears to follow the splitting crack. The damage zone in the interface has the characteristic triangular shape observed in experiments [71]. The interface experiences extensive damage, but does not fail completely for small to moderate loading. Complete failure in an interface cohesive element is observed at a much later stage, at 1.14% nominal strain. We also observe that TPC in the 90° ply originates under moderate loading. Interestingly, the initiation and growth of TPC appears to be associated with the arrest of the splitting cracks. This behavior seems reasonable based on the energy consideration that once the TPC initiate, most of the additional energy supplied at the far field is probably used up for the propagation of the TPC – hence the splitting crack gets arrested. This argument assumes that the propagation of the TPC is energetically more favorable compared to further propagation of the splitting crack. The TPC span the entire length of the specimen forming a fringe pattern of cracked and un-cracked regions; consistent with experimental observations [71]. The fringes are observed to be an element wide typically, and thus their width depend of the discretization and does not otherwise provide any fundamental length scale. The results suggest that Hashin's criteria is able to capture the qualitative behavior of splitting and TPC well. The final damage mechanism that was triggered upon increasing the far-field loading was fiber damage in tension. The fiber failure was associated with a sharp drop in load in the global load-displacement response of the laminate, and resulted in final catastrophic structural failure.

Total delamination (as opposed to partial interfacial damage) was observed at approximately 1.14% strain in the vicinity of fiber failure in the 0° ply and TPC in the 90° ply. Figure 6.1 shows the different failure modes at the end of the analysis. These failure modes are (i) delamination at the interface between the plies, (ii) splitting crack in the 0° ply, (iii) TPC in the 90° ply, and (iv) fiber failure in the 0° ply, respectively. The experimental study by [71] observed clusters of broken fibers over the entire length of the ply. The aforementioned authors also hypothesize that fiber failure may be occurring at locations of stress concentrations resulting from TPC, a hypothesis that could not be confirmed from experiments. Figure 6.1 shows that

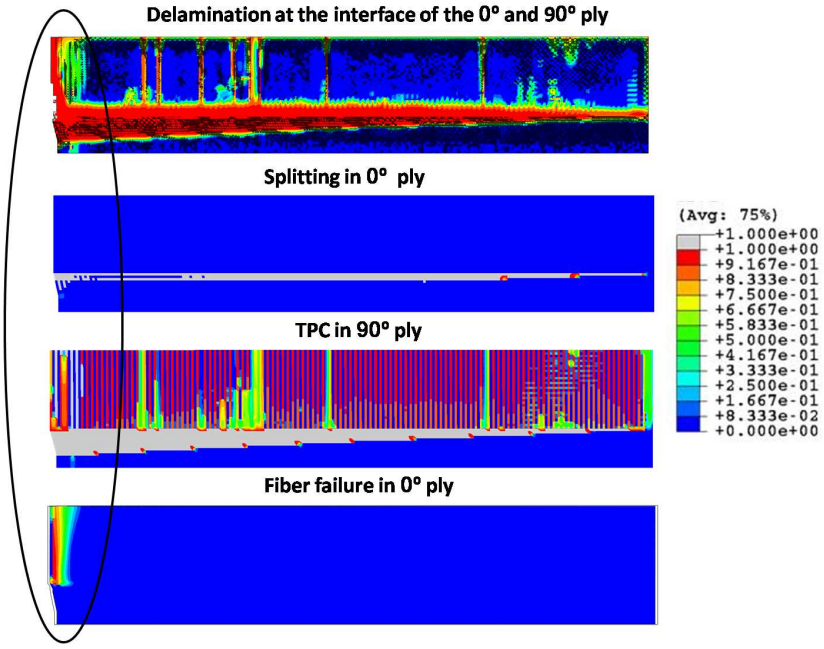

Figure 6.1: The different failure modes in the laminated composite at 1.14% strain.

fiber failure in the 0° ply occur in the vicinity of a completely damaged region of TPC (red vertical strip of heavily damaged region in the 90° ply), thereby providing some evidence in support of the hypothesis. The same behavior was also observed when two elements were used in the thickness direction for each ply. Although the fiber failure appeared at a different location, it was in the vicinity of a fully damaged TPC.

In the next phase of this work, Linde's model was used to model the ply damage behavior. With Linde's model, the plies were modeled using either shell elements (assume a state of plane-stress) or three-dimensional solid elements (assume a three-dimensional stress state). With shell elements the delamination mode of damage develops at an early stage with Linde's model, with total delamination occurring relatively early on as well. Thereafter, delamination grows to form the characteristic triangular shaped zone. Certain characteristics of the triangle-shaped zone such as the delamination angle, as measured from the numerical results (Figure 6.2), agree well with experimental observations. With solid elements delamination occurs even earlier. The results also suggested that the delamination is shear driven. The out-of-plane stress components arising when the plies are modeled using three-dimensional

elements did not appear to affect the delamination.

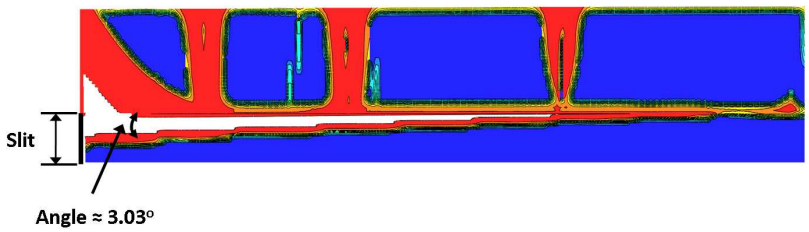

Figure 6.2: Delamination angle using C3D8R elements with Linde's model.

Under the assumption of a state of plane stress for the plies, the onset of the splitting crack occurred at approximately 60% higher nominal strain compared to the load at which splitting was predicted using Hashin's model. However the rate of growth of the splitting predicted by the two damage models appear to be about the same. The TPC fringes that were observed in the simulations using Hashin's model were by and large absent from the results using Linde's model. It is possible that the delamination damage mode, which occurs at a much earlier stage with Linde's model, consumes the available energy resulting in less remaining energy for the evolution of TPC. As with previous models, final failure in the structure occurred due to fiber damage in tension in the 0° ply.

Under the assumption of a three-dimensional stress state for the plies, the splitting mode initiates at a somewhat lower load compared to the plane stress case, and at a load that is much closer to the load predicted from the model using Hashin's criteria. The load interval between the occurrence of splitting and total delamination in some region of the ply was more or less the same under both the stress states. The TPC were captured marginally better with three-dimensional stress states. The rate of growth of delamination was somewhat higher compared to the plane stress state. To the best of our knowledge correlations, if any, between the evolution of TPC and delamination have not been addressed in any of the experimental work cited in this dissertation. This aspect of the problem deserves further investigation.

The splitting crack was captured using both Hashin's and Linde's models, except that the splits initiated at different loads. Significant damage at the interface between the plies generally accompanies splitting, consistent with experimental observations

[71]. However, complete delamination at some location at the interface accompanies fiber failure, i.e., it occurs almost at the end of the deformation history. This general behavior was captured using Linde's model as well, except for a wider gap between the initiation of the splitting and the delamination damage modes. Neither experiments [71] nor previous numerical studies [93] provide any quantitative information for these mechanisms in a $[90/0]_s$ ply. However, a recent numerical study [30], suggests that a matrix crack (splitting) occurs first followed by delamination at a higher load. They also report that the delamination follows the path of the matrix crack and evolves in a triangular shape, as observed in our investigation. However, in the aforementioned study, the ply orientation assumed is different from the one assumed in this study. Therefore, attempting a direct correlation will not be meaningful.

The main objective of this work was to understand the simultaneous initiation and evolution of the splitting and the delamination modes of damage in a laminated fiber-reinforced composite, and the complex interplay between these damage mechanisms. We also studied the initiation and evolution of TPC in the 90° ply, and the fiber tensile damage in the 0° ply that leads to the final/overall failure of the laminate. The results for the TPC with the Hasin's model are in good qualitative agreement with experimental observations. The different failure mechanisms considered in this study are very complex in nature. This area of research is still on going and this work lays out the foundation for future efforts in capturing the failure mechanisms of composites using finite element simulations.

6.2 Future Work

In this study, we modeled the progressive damage initiation and damage evolution of the ply with two different sets of failure criteria. The results obtained using these failure criteria showed some qualitative and quantitative differences in predicting the different damage mechanisms of the ply. The initiation criteria appears to be the same in both the models but the evolution of damage is different. It is worth investigating these differences further for a better understanding of the behavior of damage mechanisms captured using these sets of criteria.

Evidence from both experiments and numerical studies have shown that the final

failure of a composite material occurs due to the fiber failure. But there are other failure mechanisms that evolve and develop at a much lower load before the final failure. It is important to understand the interplay between these mechanisms and the effect of each mechanism on the other. Such an understanding will help an engineer in designing a composite material which is damage resistant.

This study has provides valuable insights, both qualitative and quantitative, on the initiation and evolution of the various failure mechanisms that occur in a fiber-reinforced composite material. But before a further detailed investigation is conducted on the interaction of these complex damage mechanisms, it is important to first validate the global response such as the load-displacement response with experimental results. Thus, more experimental results are required to correlate our results from the numerical simulations.

In this study, we used ABAQUS/Standard to perform the finite element simulations. In some cases, the analysis did not converge. Therefore, in future, ABAQUS /Explicit must be utilized to avoid convergence issues and obtain further insights for the cases that did not converge.

In the current modeling approach, the crack grows along the mesh lines. A better approach would be to let the crack follow an arbitrary path. Modern meshless techniques such as the XFEM could be utilized in such problems. The XFEM technique is now implemented in the most recent version of ABAQUS. Thus, in future, one can explore this technique to capture the different failure mechanisms that occur in a composite material.

CHAPTER 7: INTRODUCTION TO THE HIP IMPLANT

The advent of artificial hip implants has been of tremendous help to mankind in terms of providing mobility, which might otherwise have been lost due to fractures from accidents and various joint diseases. The first total hip replacement (henceforth abbreviated as THR) in the US was conducted in the sixties, and in 2005 approximately 208,600 THR surgeries were performed. It is projected that by the year 2030, about 572,000 THR procedures would be performed [75]. Given this trend, it is imperative that the implant performs as close as possible to the real hip joint. In the past THR was mostly performed in older patients suffering from various joint diseases, but in recent years THR is being performed in younger patients and athletes as a result of injuries or accidents. The post-implant activity levels in the younger group of patients and athletes will be much higher compared to the older generation. Thus, the implant must be capable of withstanding various levels of loading and at the same time must last longer. This has led to advances in understanding both the biological and the mechanistic aspects of hip joints, which in turn has fueled the quest for the perfect design of the implant. As a result, the design of hip implants is still very much evolving, which naturally requires evaluation of new ideas and designs from a durability (among others) point of view. The work presented here can be placed within that broader context.

In the following sections, a detailed background on the hip joint will be presented. This will include discussions related to (i) some of the reasons patients need a total hip replacement, (ii) the components of a typical hip implant, (iii) the general surgical procedure, and (iv) some of the common current THR techniques. This is followed by a summary of some of the previous research conducted on the mechanical aspects of the hip implant. The chapter ends with an outline of the motivation and objectives of this study.

7.1 Hip Joint

This section provides some background information on the hip joint and outlines a few of the major reasons why patients may need a THR.

7.1.1 Background on the hip joint

Figure 7.1 shows a schematic illustration of a hip joint. The femur (thigh bone) terminates in a round ball at its upper end, which is called the femur head (or the femoral ball). The femur head fits into the acetabulum, a socket formed in the pelvic bone. The head is connected to the acetabulum with the help of strong ligaments which allow a controlled motion of the head within the acetabulum. Both the femur head and the acetabulum are covered by a thin layer of cartilage which is very soft and provides a cushioning effect that enables smooth movement between the bones. A tissue called the synovial membrane lines the non-cartilaginous sections of the hip joint, as shown in Figure 7.1 (left), and secretes a fluid know as the synovial fluid which provides further lubrication to the joint.

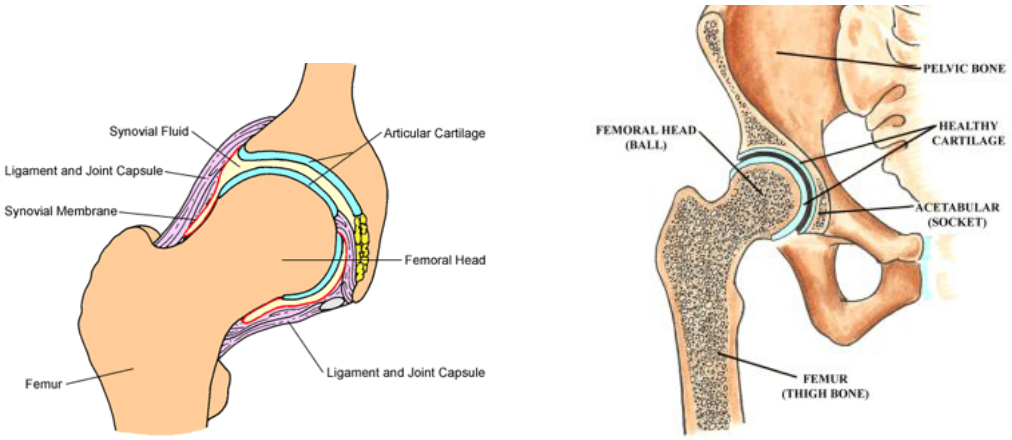

Figure 7.1: A typical hip joint (left-image courtesy of Children's Hospital Boston Web Team), and (right-image courtesy of Hospital for Special Surgery)

The hip joint is similar to the shoulder joint in some respects. The shoulder joint is very shallow while the hip joint is considerably deeper. This makes the hip joint more stable compared to the shoulder joint. This is important because the hip joint is responsible for bearing the weight of the human body. The hip joint is a triaxial joint and has motion in all three planes. Generally, the movement of the different

parts of a human body is characterized using a pre-defined set of three planes and corresponding axes [7]. These planes are: (i) *sagital* or *anteroposterior* plane, (ii) *frontal* or *lateral* plane, and (iii) *horizontal* or *transverse* plane, respectively. These planes are perpendicular to one another and each plane may be thought of as dividing the body into two equal parts.

The *sagital* plane essentially divides the body into two equal parts consisting of what we generally understand to be the left side and the right side of the body [7]. The different movements of the hip in the sagital plane are flexion, extension, and hyperextension [50]. Flexion is the forward movement of the lower limb toward the front side of the upper body. The extension is essentially the return of the flexion. Hyperextension is the backward movement of the lower limb toward the back side of the upper body. In most cases a maximum flexion of 120° and a hyperextension of 15° [50], with respect to the vertical, can be achieved. The *frontal* plane passes from one side of the body to the other, creating a front side and a back side [7]. Abduction and adduction are the movements of the hip in the frontal plane. Abduction is basically the sideways movement of the lower limb away from the center of the body and makes an angle of about 45° [50] with respect to the vertical axis. Adduction is the return from abduction with a maximum angle of 25° in the reverse direction. The horizontal plane splits the body to create a top half and a bottom half. The rotations of the hip in the horizontal plane are termed as lateral and medial rotations. These rotations are also referred to as the external and internal rotations, respectively. A rotation by about 45° can be achieved in each direction [50].

7.1.2 Hip joint diseases

The main cause of the loss of hip mobility is arthritis. Osteoarthritis, rheumatoid arthritis, and osteonecrosis are some of the common forms of this disease. Osteoarthritis is a degenerative disease in which the cartilage wears out and allows the rubbing of bones against each other. This causes swelling and results in severe pain. Figure 7.2 shows a schematic an osteoarthritic femur head from an 80 year old woman. Rheumatoid arthritis is typically the result of swelling of the synovial membrane. The membrane secretes excess fluid which causes inflammation and damage to the

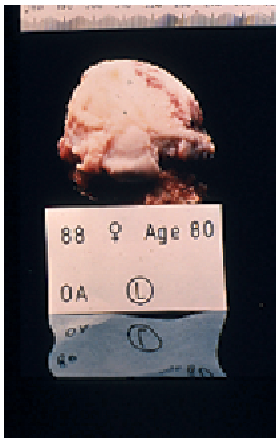

Figure 7.2: An osteoarthritic femur head (image courtesy of Department of Materials at Queen Mary University of London).

cartilage. Osteonecrosis, also known as avascular necrosis, is also a major factor leading to the damage of the femur head. In this form of the disease, the femur head collapses or dies due to a lack of sufficient blood supply. Once the head dies it cannot withstand load, resulting in severe pain and causing immobility. Pain and immobility in the hip joint are also caused by benign and malignant bone tumors, which will eventually have to be treated with surgery. THR is also considered in cases where the hip is fractured due to an accident or a fall. Generally, most of these diseases are initially treated with medications such as anti-inflammatory drugs. But if the pain and discomfort persists, hip replacement might become necessary.

7.1.3 Artifical hip implant

Sir John Charnley, a British orthopedic surgeon and a bio-engineer, invented the artificial hip implant. The artificial hip implant, shown in Figure 7.3 (left), consists of (i) the femoral stem, (ii) the femoral head, (iii) the acetabular cup, and (iv) a liner that plays the role of the cartilage. Titanium and cobalt/chromium alloys are generally used for the stem, head, and the cup. However, studies have shown that the use of ceramics (head) and ultra high molecular weight polyethylene (liner) reduces the amount of wear between the components, which in turn provides a longer implant life.

There are two types of techniques that are commonly used in THR: cemented and cementless techniques. In the cemented technique, a common bone cement known

as polymethylmethacrylate (PMMA) is used to fix the implant as shown in Figure 7.3 (right). The stability of the implant relies on the bond between the cement and the bone. A patient usually takes lesser rehabilitation time using this technique. In the case of a cementless technique, the implant has a surface coating that induces bone growth into the implant. The strength of this implant depends on the rate of

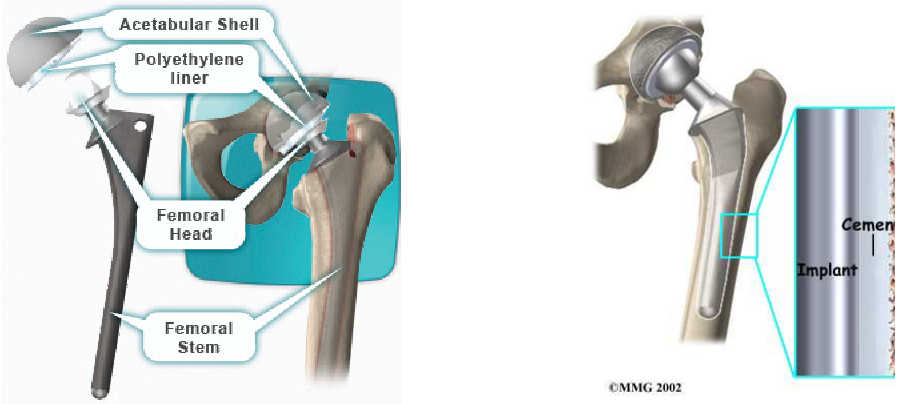

Figure 7.3: An artificial hip implant (left-image courtesy of DePuy Orthopaedics, Inc.) and a cemented implant (right-image courtesy of Medical Multimedia Group LLC).

bone growth and therefore it generally requires a longer healing time. This technique requires that the implant surface be in flush with the inner bone surface, and the gap between the implant and bone is no more than 2 mm.

7.2 Motivation

Recent studies [39] have shown that the United States population will grow by 18% between 2000 and 2020. As a result the population of elderly people will also increase. It is reported that the number of people over the age of 45 will increase by almost 37% from 2005 to 2030. Most hip related problems such as arthritis arise in older patients. With such a high increase in the older generation, it is obvious that hip related issues will become increasingly important. Statistics [39] also suggests that in 1994, 15% of the population in United States reported symptoms related to arthritis. This number is expected to increase to 18.2% by 2020 [39]. Osteoarthritis is very common among obese people, a segment of the population that appears to be showing an increasing trend as well. All the trends discussed above strongly suggest

that the number of health related issues, specifically related to the hip, is bound to increase. As mentioned previously, the number of THR procedures is projected to increase by almost 174% by 2030 [75] . Likewise, the number of revision THR can also be expected to increase significantly. To meet the above demands as well as reduce the number of revision THR surgeries, the implant design and durability must be improved. There are various factors that affect the performance of an implant. Some of these factors are: (i) the durability of the design, (ii) bio-compatibility of the implant material and (iii) the wear characteristics. These design aspects require in-depth studies to improve, over time, the functionality and reliability of the implant. In this dissertation, we focus specifically on durability aspects of artificial hip implants.

Another specific concern that motivated this study was communicated by surgeons [80] at the *OrthoCarolina Hip and Knee center* at Charlotte. They noticed a recent trend of the use of larger sized femoral balls in order to alleviate concerns surrounding dislocations of smaller-sized balls from the socket. It was not clear whether a larger femoral ball could lead to higher stresses in the neck region of the implant, and hence adversely affect the long-term durability of the implant. In this study we investigate the effects of an increase in the femoral ball size on the stresses in the neck region of the stem, with the eventual aim of relating such stresses to the fatigue life of the implant. In the following section, some of the previous research conducted on the mechanical aspects of the hip implant is discussed.

7.3 Previous Work

With the increasing demand of THR, researchers are investigating various aspects of the artificial implant design, such as bio-compatibility of the materials involved [81] and [28], best combination of materials to improve the wear characteristics [13], improvement of implant shape using various optimization methods [44], and the long-term durability of the implant design [8] and [65]. Some of the initial work in this area (Charnley & Halley [16]) focused on the wear of high molecular weight polyethylene sockets. The wear was measured on radiographs over a period of 9-10 years in patients whose age averaged around 73.3 years at the end of the study. The key conclusions from this work were: (i) the average rate of wear was 0.15 mm/year in 68% of patients,

(ii) wear of more than 2.5 mm in 10 years occurred in about 15% of the patients, and (iii) the wear did not have any relationship with the body weight and activity level of the patient. Buford & Goswami [13] reviewed the mechanisms of wear for different implant material combinations like polyethylene on metal, metal on metal and ceramic implants. The review concluded that the wear is a function of variables such as the type of material used, contact stresses, lubricants and clearance, surface hardness and roughness, type of articulation due to motion, number of cycles, solution particle count and distribution, and finally, oxidation of materials. Their study also suggested higher rates of wear in titanium alloys and stainless steels compared to cobalt chromium alloys and ceramics.

Katoozian and Davy [44] carried out FE based 3D shape optimization of cemented and uncemented implants. The optimization system consisted of an implant shape generator, a mesh generator, a constraint and objective function calculation program, the FE code ABAQUS [1], and optimization modules. Two kinds of loading conditions were considered: a physiological loading and a pure bending moment. The study assumed the bone to be an isotropic elastic material, and the interfaces between the bone-implant and the cement-implant to be perfectly bonded. The objective of the optimization procedure was to obtain a smooth distribution of the interfacial stresses. The final optimized design predicted a wedge shaped proximal region (close to the head) and a tapered distal stem. Pyburn & Goswami [64] investigated the stress distribution in hip implants for various cross-sections in the presence of bone cement, utilizing FE simulations on idealized implant assemblies. A comparative analysis of stresses generated in the cement-implant interface for different cross-sections of the implant was performed. Latham & Goswami [48] studied the effect of geometric parameters such as the neck angle, neck diameter, and head diameter on the stress distribution in the stem region. They concluded that larger head sizes lead to lower stresses in the stem region. In their study the ball and stem were considered a single component of the implant. In recent implants, the ball and the stem are manufactured separately and assembled together during surgery. The details of the interaction between the ball and the stem, which could potentially provide insights

on wear mechanisms at the interface, will be investigated in this present work.

An important characteristic of the implant material that ensures its long-term safe usage in human bodies is its fatigue life. Recently, Niinomi [60] carried out a detailed study of the fatigue characteristics of metallic bio-materials such as titanium alloys, cobalt alloys, and stainless steel, used commonly for hip implants, bone plates, and dental implants. Based on data reported in earlier literature, the authors described the fatigue strength, fretting fatigue strength, and fatigue crack propagation rates in these materials in air, a living body, and a simulated body environment. These properties were also related to underlying microstructure of the materials. Hung et al. [36] developed an algorithm that relies on the FE method to predict the fatigue behavior of cemented hip prostheses. The model assumes three different bonding conditions between the cement and the implant stem - firmly bonded, proximal separation, and progressively debonding interfaces. The study suggests that it is important to accurately model the interface to determine the stresses in the cement region for different loading conditions. This algorithm has shown results that are in accord with results observed in clinical studies and other fatigue tests.

7.4 Objectives

The present study examines how the long term durability of hip implants is affected by an increase in the femoral ball size. The latter constitutes one of the more recent trends in the design changes in hip implants, in response to a need for improved stability of the femoral ball within the socket and a larger range of motion. We investigate 2D and a 3D model of the ball-stem assembly of a generic hip implant subjected to a static load. The load corresponds to the so-called single stance phase of gait, which represents the short periods of time during normal walking when only one leg bears the entire body weight. In reality, the head of the femur bone is subjected to a non-uniform distributed load. The assumptions made regarding the loading conditions in this study are explained in detail in the following chapter. Two different femoral ball sizes are considered, and the effects of the ball sizes on the stress distribution in the neck region of the femoral stem are investigated. Previous works [44] and [64] on durability of hip implants using the FE method have modeled only the

stem and ignored the effect of the contact interaction between the ball and the stem. In the present work, this interaction is accounted for by enforcing appropriate contact conditions between these two parts. Within this basic framework, we also investigate the influence of the mesh size on the solutions. All simulations are carried out using three different finite element mesh densities. The latter approach ensures that we rely on the *converged* solution (in the standard sense of the term in the context of discrete approximations to continuous problems) for making predictions regarding long-term durability of the hip implant. In summary, the specific objectives of this work are as follows:

1. Analyze a 2D model of the implant including the femoral ball.
2. Investigate the effect of varying femoral ball size on the stress distribution in the neck region.
3. Investigate the differences between the idealizations of distributed versus concentrated loading on the femoral ball.
4. Develop an analytical model and compare with its predictions with the results from the FE analysis.
5. Investigate the contact interaction between the ball and the stem.
6. Determine the utility of two-dimensional models by comparing the results from two-dimensional simulations with corresponding results from three-dimensional simulations.
7. Estimate the fatigue life of the implant based on the stress distribution in the neck region of the stem.

In the next chapter, the FE modeling assumptions will be presented.

CHAPTER 8: MODELING METHODOLOGY

8.1 Modeling Assumptions

A three-dimensional (henceforth abbreviated 3D) model of the stem and the femoral ball was generated using SolidWorks [69] (Figure 8.1(left)). The dimensions for this model were obtained from measurements taken on an actual implant. Certain simplifying assumptions were made regarding the geometry when creating the 3D model. For example, the out-of-plane thickness of the stem region was assumed to be the same as that of the neck region. In reality, the neck region is bulkier compared to the bottom stem region. Also in reality, the region of the stem on which the ball is fitted has a slightly tapered form which is not considered here. The above model formed the basis of the 3D FE analysis. A center cross-section of this model (Figure 8.1(right)) was utilized to perform a two-dimensional (henceforth abbreviated 2D) FE analysis. The degree of correlation between the 2D and the 3D results is expected to shed light on the applicability of simplified 2D models for making global predictions such as the long-term durability of the implant. All simulations were carried out using the commercial finite element software package ABAQUS [1].

8.2 Material Model

The implant stem and the ball are assumed to be made of the titanium alloy, Ti-6Al-4V. We assume an elastic-plastic material behavior with an isotropic hardening rule. The von Mises yield criterion [1] is used to govern the yielding behavior and is given as,

$$f(\boldsymbol{\sigma}) = \sigma_e - \sigma^{\circ}(\bar{e}^{pl}), \tag{8.1}$$

where, σ_e is the equivalent Mises stress, σ° is the yield strength of the material, and $\bar{e}^{pl}$ is the equivalent plastic strain which is defined as the plastic strain under uniaxial

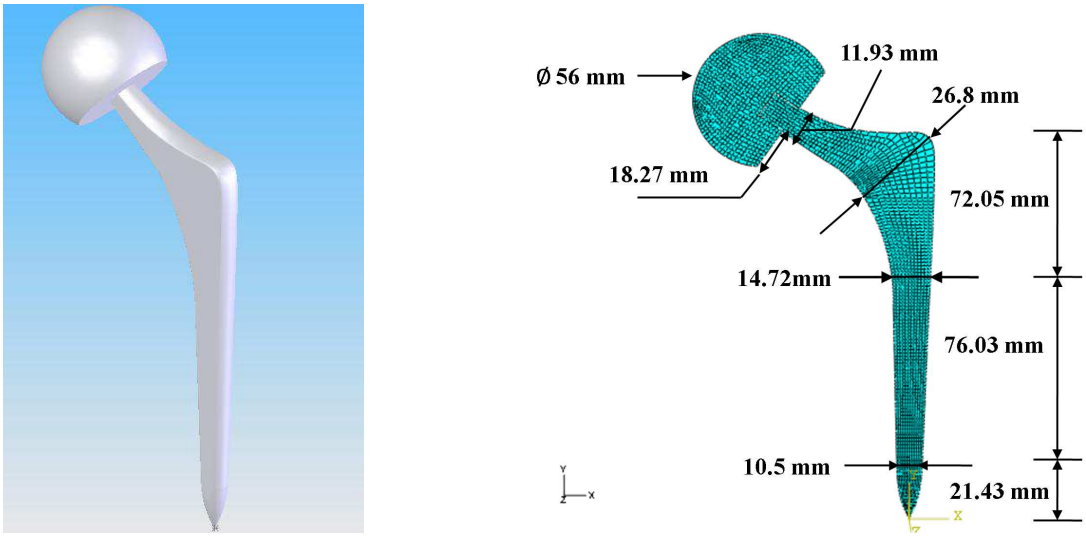

Figure 8.1: A 3D model (left) and a 2D cross-section (right).

loading. The equivalent Mises stress σ_e is given by,

$$\sigma_e = \sqrt{\frac{3}{2}\mathbf{S} : \mathbf{S}}, \tag{8.2}$$

where $\mathbf{S}$ is the deviatoric stress tensor. The flow rule is given by,

$$\dot{\bar{\epsilon}}^{pl} = \dot{\lambda}\frac{\partial f}{\partial \boldsymbol{\sigma}}, \tag{8.3}$$

where $\dot{\bar{\epsilon}}$ is the rate of plastic strain tensor, and $\dot{\lambda}$ is the plastic strain multiplier

Equation 8.1 suggests that if the equivalent Mises stress σ_e is less than the specified yield strength, σ°, then $f(\boldsymbol{\sigma})$ is less than 0, and the material is said to deform elastically. If σ_e is equal to the yield strength σ° then $f(\boldsymbol{\sigma})$ is equal to 0 and the material is said to deform plastically. Figure 8.2 shows the stress-strain behavior of the material. An initial yield stress of 825 *MPa*, and a ultimate stress of 895 *MPa* corresponding to an elongation of 6% were assumed [57] as representative values to quantify the strength of the material.

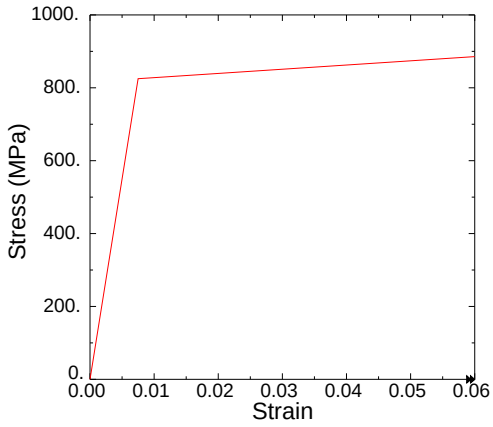

Figure 8.2: Uniaxial stress-strain response of titanium alloy.

8.3 Contact Interaction

In many engineering problems two or more parts often come in contact with one another. To deal with such situations, ABAQUS provides a built-in contact modeling framework. The two surfaces of the two bodies that could potentially come in contact with each other are characterized as *slave* and *master* surfaces, respectively. The contact formulation constrains the slave surface from penetrating the master surface. As a result, contact pressure between the two surfaces is generated when the surfaces contact each other. If the two surfaces are rough, then the tangential interaction between these surfaces would involve frictional forces, which provide resistance to tangential relative motion between the surfaces. The contact constraints are said to be *discontinuous* [1] in the sense that the constraints are applied only when the two bodies touch each other, and no constraints are needed when the bodies are not in contact.

The definition of contact interaction between two surfaces involves a decision regarding the appropriate choices for the slave and master surfaces. Generally the surface that is, in relative terms, more finely discretized is picked as the slave surface. In cases where the meshes on both surfaces are similar, the surface of the softer material is chosen as the slave surface. When both the mesh and the material properties for the two surfaces are similar, the surface belonging to the least stiff body is picked

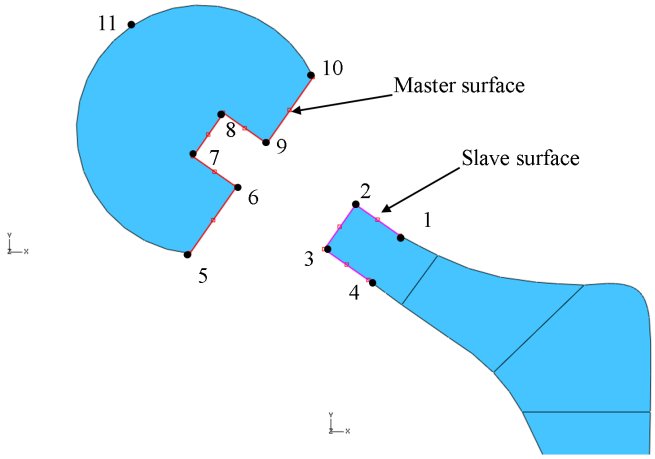

Figure 8.3: Basic ingredients of contact interaction.

as the slave surface [1].

The contact formulations in ABAQUS/Standard are broadly classified into two categories: (i) node to surface contact, and (ii) surface to surface contact. In the node to surface formulation, the contact conditions are enforced at each node on the slave surface. The formulation prevents the penetration of the slave nodes into the master surface. This approach could potentially cause spikes and valleys in the distribution of contact pressure in the contact patch [1]. In the case of surface to surface formulation, the contact conditions are enforced in an average sense over the slave surface. This leads to a more accurate stress and contact pressure distribution over the contact patch [1]. The surface to surface formulation is better suited for contact involving sharp corners [1].

The surface-based master/slave algorithm of ABAQUS is utilized in this study. The surface on the ball is assumed to be the master surface (points 5-6-7-8-9-10 in Figure 8.3), while the surface on the stem (points 1-2-3-4 in Figure 8.3) is assumed to be the slave surface. The slave and master surfaces are chosen based on the stiffness of the ball and the stem of the implant. Finite sliding between the surfaces is assumed. The finite sliding assumption allows arbitrary relative motion between the two surfaces in contact. The surface-normal contact behavior is defined using the default hard contact formulation that enforces the contact constraints by means of

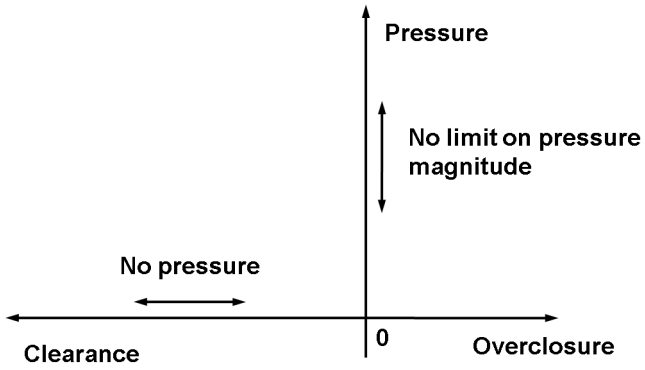

Figure 8.4: Pressure-overclosure relationship for hard contact.

Lagrange multipliers. The hard contact formulation is based on a pressure-overclosure relationship as shown in Figure 8.4. The contact pressure at a slave node is zero when it is not in contact with the master surface. The contact pressure can take on any value when the slave node is in contact with the master surface. With the hard contact behavior, the options of either allowing separation or allowing no separation at a slave node after it comes into contact with the master surface is available, and the implications of these options will be investigated in detail for the hip-implant model.

The surface-tangential behavior in our model assumes a frictional coefficient of 0.35 (titanium-titanium) [57], and is accommodated using the default penalty approach [1]. The tangential motion, also know as *slip*, does not occur until the shear stress exceeds a critical value. The critical value of the shear stress is proportional to the contact pressure and is given by,

$$\tau_c = \mu p, \tag{8.4}$$

where μ is the friction coefficient and p is the contact pressure. The ideal situation of having no slip till the critical shear stress is exceeded is generally difficult to satisfy in practice. Therefore, a penalty formulation that allows for a small amount of slip in this situation is used.

8.4 Boundary Conditions

In practice, the depth of insertion of the stem into the femur bone is not clearly defined. Generally, the entire stem portion of the implant is inserted exposing only

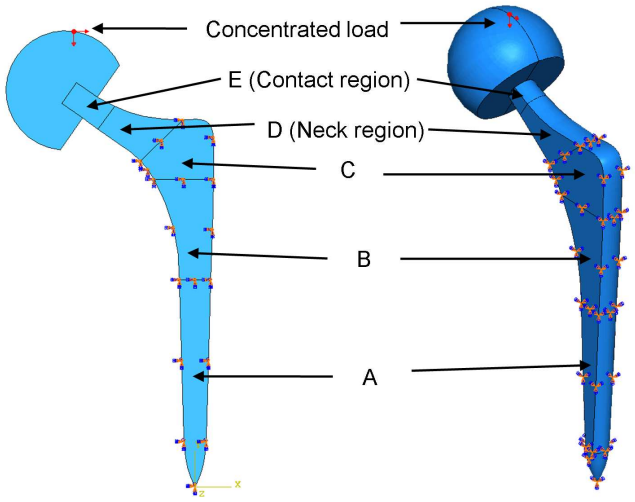

Figure 8.5: Concentrated load and definition of the constrained boundary conditions, 2D model (left) and 3D model (right)

the neck region. Each implant design will have a particular depth up to which it can be inserted. In this study, the stem is partitioned into a number of different regions (Figure 8.5) and two types of constraints are considered (i) fully constrained (FC) boundary conditions for which regions A, B & C are fixed, and (ii) partially constrained (PC) boundary conditions for which regions A & B are fixed. We assume a perfect bond between the stem and the bone.

8.5 Loading Conditions

A patient weighing 200lbs and a loading corresponding to a single stance phase of gait is assumed in this analysis. Using the principles of statics, the force, **F**, acting on the femur head for a single stance phase of gait is computed [27] to be 2.75 times the body weight, and acting at an angle of 69^0 from the horizontal. Also, in vivo studies [9] have shown that the peak hip contact force during slow and fast walking are 255% and 279% of the body weight, respectively. In reality, the load that is being transmitted from the pelvis region onto the femur head is not a concentrated load. This load is distributed and non-uniform in nature. However, in bio-mechanics studies [65], [64] amd [45], the non-uniform distribution of load is normally idealized as a concentrated force. The concentrated load is applied at the top arc of the head as this region (between point 10 and point 11 in Figure 8.3) applies the greatest pressure

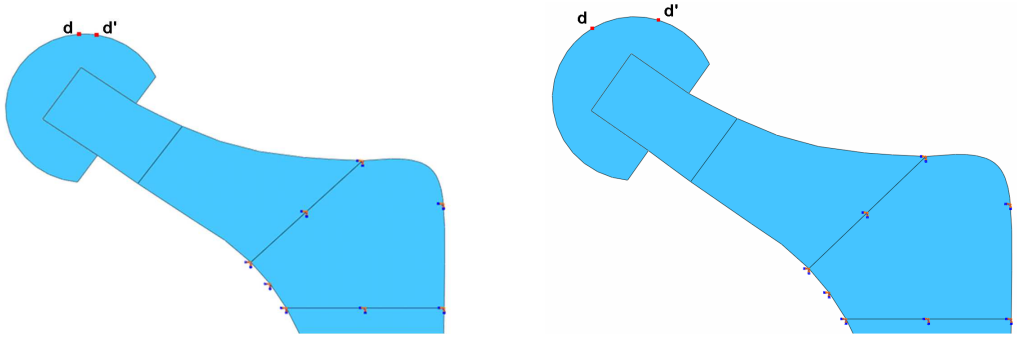

Figure 8.6: Plot showing the region subjected to a distributed load, load area-1 (left) and load area-2 (right)

on the inner cavity of the acetabular socket. Also, a study [94] based on the discrete element analysis technique suggests that the peak contact forces (for slow and normal walking) occur on the top lateral roof of the acetabular socket (region of the socket directly above the region between points 10 & 11 in Figure 8.3). Since the complete assembly of the hip implant, that includes the acetabular cup and the liner, is not considered, the load is directly applied on the femoral ball. The concentrated force is resolved into its vertical and horizontal components as shown in Figure 8.5. In the 3D model the concentrated load is applied at a point along the mid cross-section, that was considered in the 2D model.

The appropriateness of the idealization of a concentrated load is investigated by taking into account distributed loading conditions on the femoral head. The area over which the distributed load is applied is varied and is shown in Figure 8.6. Two cases of distributed loading are considered; (i) load area-1 (Figure 8.6, left), and (ii) load area-2 (Figure 8.6, right). In load area-1, the top arc of the ball is partitioned between points d and d'. The length of this partition is approximately 3 mm. The length of the partition is increased to approximately 11 mm in the case of load area-2. The point at which the concentrated load is applied is taken to be the center point for the partitions created to define the two load areas.

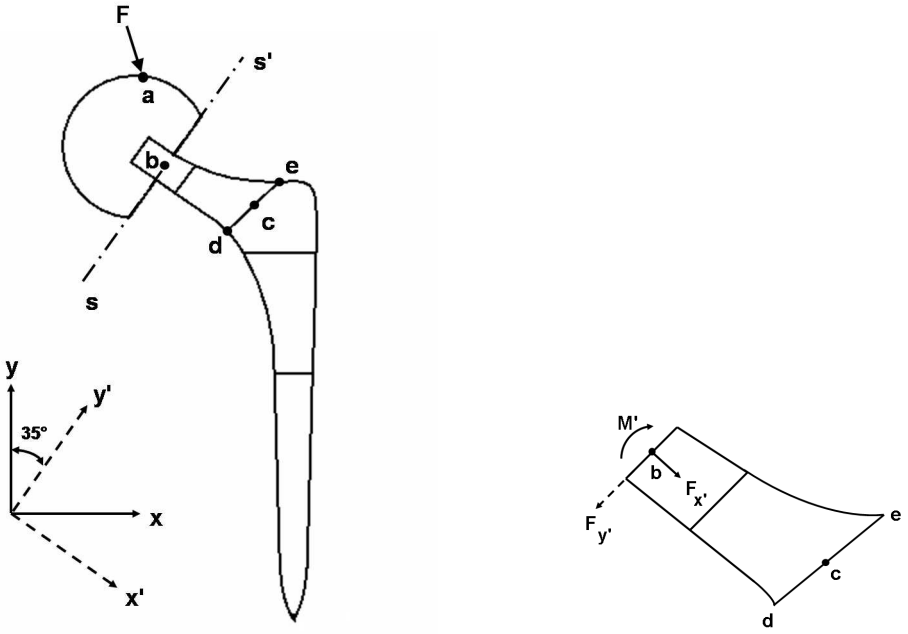

Figure 8.7: Schematic of the implant with a concentrated load (left) and the section considered for the analytical model (right).

8.6 Analytical Model

A simple analytical model based on the concepts of the strength of materials is developed. The objective of developing this model is to get an approximate estimate of the bending stresses in the neck region of the stem. In this model, only the geometry of the neck region will be considered. The following is the methodology used in developing the geometry and loading conditions for the analytical model.

The schematic of the implant with a concentrated load applied on the ball is shown in Figure 8.7 (left). A section line $s - s'$ is assumed to split the stem at point b into 2 halves. The bottom half of stem region, shown in Figure 8.7 (right) is the geometry considered in this analytical model. A new co-ordinate system, x'-y' is assumed such that the x' axis is perpendicular to the edge containing point b (Figure 8.7 (right)). The x'-y' coordinate system makes an angle of 35° with the global x-y coordinate system as shown in Figure 8.7 (left). The components of the force **F** acting at point a in the global x-y coordinate system, are now resolved into the x'-y' system. Using the principles of statics (replacing a force by a force and a couple), the components of the force acting at point a are transferred to point b. The system of forces and

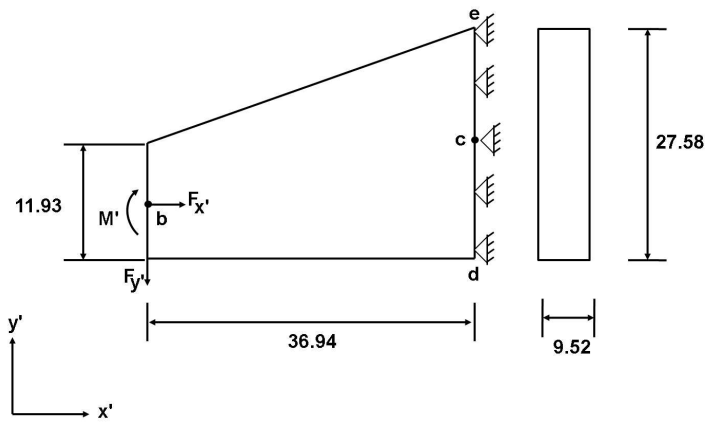

Figure 8.8: Geometry considered for the analytical study.

moments acting on the bottom half of the stem is shown in Figure 8.7 (right).

The magnitudes of the forces do not change upon translation to point b, and are given by: $F_{x'} = 2028.64N$, and $F_{y'} = 1368.34N$. These values are independent of the ball diameter. However, a change in the ball diameter is accounted by for by including (to compensate for translating the forces from point a to point b) a moment acting at point b. The resulting values for the moment, M', computed for the 28 mm and 56 mm ball diameters are 802.16 $N - mm$ and 14059.85 $N - mm$, respectively.

The section of the stem region assumed in the analytical model (Figure 8.7 (right)), is further simplified by replacing the curved boundaries with straight lines. The simplified beam configuration, along with the relevant dimensions, is shown in Figure 8.8. Some of the key features of this geometry are: (i) lack of symmetric in the plane of the paper, (ii) tapered cross-section with a constant out-of-plane thickness, and (iii) ratio of length to height of approximately 1.33. For such a short stubby beam, the Euler-Bernoulli beam theory will not provide accurate results. The Timoshenko beam theory is applicable, but the details can be complicated. Therefore, as an alternative approach, we attempt to relate the features of the cantilevered beam in our model to a gear tooth which is also tapered and which has a relatively small length to height ratio [95]. The schematic of the gear tooth, which may be thought of as a short cantilevered beam with a constant out-of-plane thickness, is shown in Figure 8.9

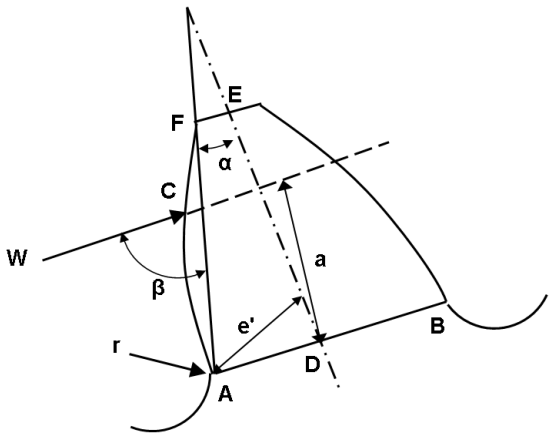

Figure 8.9: Geometry of the gear tooth representing a short cantilever beam [95].

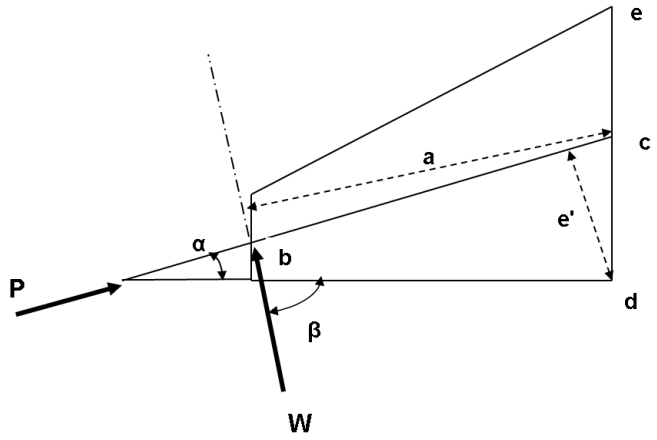

Figure 8.10: Geometry of the cantilevered gear tooth simplified to match the analytical model.

The stress at point A due to the concentrated load W applied on the short cantilever beam (shown in Figure 8.9) is given by [95],

$$\sigma = \frac{W}{t}\left[1 + 0.26\left(\frac{e'}{r}\right)^{0.7}\right]\left[\frac{1.5a}{(e')^2} + \frac{cos\beta}{2e} + \frac{0.45}{(le')^{1/2}}\right], \tag{8.5}$$

where W is the applied concentrated load, t is the out-of-plane thickness of the beam, e' is the perpendicular distance from point A to the beam axis ED, r is the radius of the fillet, a is the distance from the edge AB to the load line, β is the angle between the load line and the edge AF, and l is the (straight-line) distance between points A

and C.

The geometry and the loading conditions shown in Figure 8.9 can be further modified or oriented to match the geometry and loading conditions of our analytical model. The load W acting at point C is translated to point F (Figure 8.9). The radius of the fillet, r, is assumed to be infinity, resulting in a straight edge. The aforementioned modifications, when applied to our analytical model, leads to the configuration shown in Figure 8.10.

The section normal stress at point d (Figure 8.10) is computed using Equation 8.5. The system of forces ($F_{x'}$ and $F_{y'}$) shown in Figure 8.8 are transformed into the quantities W and P (as shown in Figure 8.10) based on the angle α. The bending moment, M', is absorbed within W for determining the bending stress at point d (Figure 8.10). The total stress at point d consists of the bending stress that is computed from equation 8.5, and the axial stress due to the axial load P. The latter is computed by dividing the concentrated load P by the area of cross-section at the right end.

The quantity in the first pair of brackets on the right hand side of Equation 8.5 is the stress-concentration factor of the fillet. This term reduces to unity based on the assumption for the fillet radius. In the second pair of brackets (Equation 8.5), the first term represents the bending moment over the section modulus [95], the second term is the contribution from the component of the load in the direction of the edge AF (Figure 8.9), and the third term represents an adjustment for small length/height ratio [95]. The results for the total normal sectional stress computed based on the above methodology are presented in Chapter 9.

8.7 Fatigue Life Estimation

The implant is generally subjected to a number of repetitive cycles of load during daily life activities such as walking, running, climbing stairs, etc. Among these activities, we have considered only the single stance phase of gait in all our simulations thus far. In this part of the study we utilize the results obtained from the earlier simulations to study the durability of the implant design by means of fatigue life calculations. A stress-life based approach is used to determine the total life of

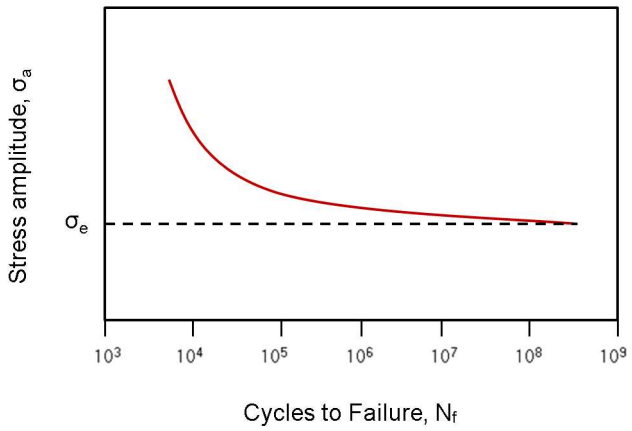

Figure 8.11: Typical S-N curve.

the implant. This approach is generally utilized in situations that are classified as *high-cycle fatigue* [78], with the stress magnitudes well within the elastic limit of the material. The basis of this approach is the so-called S-N curve [78] which is a plot of the stress amplitude σ_a versus the number of cycles to failure N_f. Figure 8.11 shows a typical S-N curve showing the variation of the stress amplitude versus the number of cycles to failure. The quantity, σ_e, shown in the figure is referred to as the *endurance limit* which represents the stress amplitude below which the number of cycles to failure is essentially infinite [78]. Based on the S-N curve, one can estimate the number of cycles to failure for a given stress amplitude and vice versa. There are a number of empirical laws which provide a good fit to the S-N curve. Among the set of available empirical laws, Basquin's law is particularly well known [78] and is expressed as:

$$\sigma_a = (\acute{\sigma_f})(2N_f)^b, \tag{8.6}$$

where σ_a is the stress amplitude or alternating stress, $\acute{\sigma_f}$ is the fatigue strength coefficient (also equals to the true fatigue strength for most metals [78]), b is the fatigue strength exponent and N_f is the number of cycles to failure. The stress amplitude or the alternating stress, σ_a, can be determined from the FE results, following which the above law (Equation 8.6) can be used to find the number of cycles to failure. But this

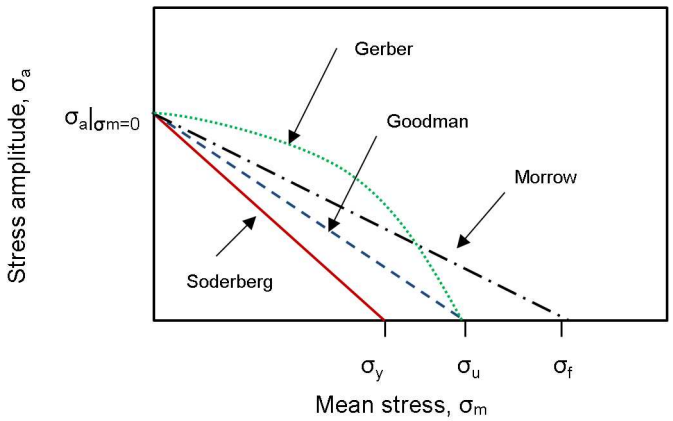

Figure 8.12: Constant-life diagram used to represent effects of mean stress in fatigue.

empirical relationship pertains to a fully reversed stress cycle with a zero mean stress, whereas in our study the loading condition is such that the mean stress is non-zero.

The mean stress effects in fatigue are generally represented by the constant-life diagrams. Figure 8.12 shows a typical constant-life diagram which is a plot relating the mean stress, σ_m to the stress amplitude, σ_a. These diagrams indicate the safe regime of a structure for a combination of stress amplitude, σ_a and mean stress σ_m at a specified life, i.e. number cycles to failure N_f. The regime to the left of the curve (8.12) is considered to be safe while the regime to the right is considered to be unsafe for a particular value of N_f. Some of the well known models that consider the effect of mean stress (shown in Figure 8.12) are Gerber (1874), Goodman (1899), Soderberg (1939) and Morrow (1968), [78]. The forms of each of these empirical models are as follows:

Gerber:

$$\sigma_a = \sigma_a|_{\sigma_m=0}\left[1-\left(\frac{\sigma_m}{\sigma_u}\right)^2\right], \tag{8.7}$$

Goodman:

$$\sigma_a = \sigma_a|_{\sigma_m=0}\left[1-\frac{\sigma_m}{\sigma_u}\right], \tag{8.8}$$

Soderberg:

$$\sigma_a = \sigma_a|_{\sigma_m=0}\left[1-\frac{\sigma_m}{\sigma_y}\right], \tag{8.9}$$

Morrow:

$$\sigma_a = \sigma_a|_{\sigma_m=0}\left[1-\frac{\sigma_m}{\acute{\sigma_f}}\right], \tag{8.10}$$

where $\sigma_a|_{\sigma_m=0}$ is the stress amplitude for a fully reversed loading with zero-mean stress, σ_y is the yield strength of the material, σ_u is the ultimate tensile strength of the material, and $\acute{\sigma_f}$ is the fatigue strength coefficient. The stress amplitude, σ_a, and the mean stress, σ_m, are defined by the equations:

$$\sigma_a = \frac{\sigma_{max}-\sigma_{min}}{2}, \tag{8.11}$$

$$\sigma_m = \frac{\sigma_{max}+\sigma_{min}}{2}. \tag{8.12}$$

The mean stress is also characterized in terms of the ratio of the minimum stress σ_{min} and the maximum stress σ_{max}, and is defined as the load ratio, R. A load ratio, R=-1 would correspond to a completely reversed load cycle, $R = 0$ leads to a zero tension fatigue, and $R = 1$ corresponds to a static load.

All the aforementioned empirical laws that consider the mean stress effect have a similar form. The differences among the laws is that Soderberg's law considers the yield strength, Goodman's and Gerber's laws take into account the ultimate tensile strength, and Morrow's law is expressed in terms of the fatigue strength coefficient. All the laws are governed by a linear relationship between the stress amplitude and mean stress except for Gerber's law. Based on Figure 8.12, the Soderberg line provides a conservative estimate of the fatigue life for most metals [78]. Goodman's law gives a good estimate for brittle metals while this law is considered to be conservative for ductile metals. Gerber's law provides good estimates for ductile metals for a tensile

mean stress [78]. Morrow's law, on the other hand, is a direct modification of the Basquin's law. This law provides a more reasonable estimate of fatigue life for a load ratio $R = 0.1$. In general, this law can be utilized to predict the fatigue life for any combination of σ_m and σ_a [58].

Previous studies ([45],[46], [65], and [58]) have considered all the above mentioned empirical laws (considering the mean stress effect) to determine the fatigue life of the implant. In this study, we assume the implant to be made out of a titanium alloy (Ti-6Al-4V). It is not clear if one of the above laws is better suited for titanium than another one. Therefore, we determine the number of cycles to failure using all of the above laws to determine how the predictions differ from one another.

As mentioned previously the implant is, in general, subjected to loads resulting from different activities. These loads would correspondingly result in different stress amplitudes. In such situations the Palmgren-Miner law, which provides a simple criterion to determine the fatigue life of a structure subjected to loads with varying stress amplitudes, can be utilized. The Palmgren-Miner law is given by:

$$\sum_j \frac{n_j}{N_j} \quad = \quad 1. \tag{8.13}$$

For each stress level j, n_j is the number of cycles of load applied and N_j is the corresponding number of cycles to failure. We consider a single stance phase of gait, hence $j = 1$. In that case the above equation simply states that the $n_j = N_j$ at failure. However, if we were modeling a number of different activities, then the above equation could provide the potential combinations of the different activity cycles that could lead to fatigue failure. It is interesting to note that we determined the number of cycles of single stance gait per day using a pedometer reading that was noted from 3 different people with varying activity levels. This number was found to be approximately 2000 cycles per limb.

In the next section, we outline some of the other assumptions made in this study.

8.8 Other Assumptions

The 2D FE analysis assumed plane stress conditions, and simulations were carried out using fully integrated elements (element type CPS4 in ABAQUS/Standard). For comparison purposes, some simulations were also carried out with plane strain elements (element type CPE4 in ABAQUS/Standard). The issue of mesh convergence of the FE results was explored for all cases. In the following chapters, any comments made on the convergence of stresses should be interpreted as the convergence with respect to the mesh (i.e element size). It turns out that the stresses are very high in the periphery of the regions where the constraints are applied. This is caused by the reaction forces generated as a result of the boundary conditions. This effect fades as one moves away from this constrained region. In order to ignore this boundary effect, we apply fixed constraints on regions A, B & C the PC setup, and examined the stress distribution in the neck region. We justify not considering the high stresses in the vicinity of the constrained region by noting that in reality there is likely to be some flexibility at the implant-bone interface, which we have neglected here.

The 3D model poses difficulties in using hexahedra elements due to the complicated geometry. Tetrahedra elements approximate curved boundaries well and are geometrically versatile. Therefore, the 3D analysis is performed using the modified version of second order tetrahedra elements (element type C3D10M in ABAQUS/Standard). These elements use full integration and the modified version minimizes volumetric locking that is generally observed in fully integrated elements. In the next chapter, the FE results along with a detailed discussion of the key observations made from this study, are presented.

CHAPTER 9: RESULTS AND DISCUSSION

In this chapter, we present detailed results for stresses in the neck and the contact (with the femoral ball) regions in the implant stem. These regions are defined in Figure 8.4 (Chapter 8, partition region D & E, respectively). We will also be referring to the points 1, 2, 3 & 4 defined in Figure 8.3 (Chapter 8) to describe the location of the peak stress, and the spatial distributions of the contact tractions and separations. We will also be referring to Figure 8.10 from Chapter 8 to discuss the results for the bending stress in the neck region of the implant. This chapter is arranged as follows: the results for the two-dimensional simulations under concentrated and distributed loading conditions, respectively, are presented first, along with analytical estimates for the stresses. This is followed by a discussion of the results for the three-dimensional simulations, which in turn is followed by the results from the fatigue life calculations. We end this chapter with a summary of the results.

9.1 Two-dimensional Analysis

9.1.1 Simulations using concentrated load

Figure 9.1 shows the von Mises stress distribution in the stem and femoral ball for the FC case. For the 28 mm diameter ball, the peak stress in the contact region occurs at the right corner tip of the stem, just below the applied load (in the vicinity of point 2). With a 56 mm diameter ball, the peak stress in the contact region occurs at the intersection of the sharp corner in the ball and the stem (around point 1). The sharp corners in the ball (both, 28 mm & 56 mm) leads to high stresses (singularity according to theory of elasticity, page 184 [70]) at the corners in the contact region. This can be observed from the mesh convergence values tabulated in Table 9.1. The stresses in the contact region increase as the mesh is refined, instead of converging to some value for each of the cases. This trend is observed under both the assumptions

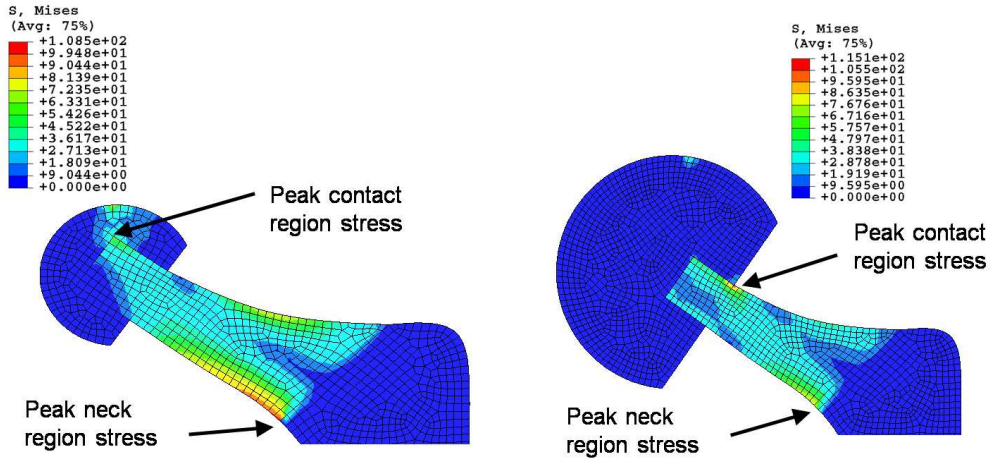

Figure 9.1: von Mises stress distribution for FC boundary conditions and surface to surface contact; 28 *mm* ball (left) and 56 *mm* ball (right)

of separation and no separation for the contact interactions. The magnitudes of the stresses do not appear to converge, suggesting that the stresses may be singular.

Table 9.1: 2D results of von Mises stress values for the FC case.

2.75 x BW=550lbs		28 mm ball diameter		56 mm ball diameter		28 mm ball diameter		56 mm ball diameter	
		CPS4 Stresses in neck region (MPa)	CPS4 Stresses in contact region (MPa)	CPS4 Stresses in neck region (MPa)	CPS4 Stresses in contact region (MPa)	CPE4 Stresses in neck region (MPa)	CPE4 Stresses in contact region (MPa)	CPE4 Stresses in neck region (MPa)	CPE4 Stresses in contact region (MPa)
Surface-Surface (separation)	Coarse	99.23	56.71	80.16	107.10	85.46	42.13	69.11	77.08
	Medium	110.30	71.52	90.84	137.70	98.14	48.69	80.47	96.15
	Fine	128.10	90.71	106.4	178.30	120.30	59.62	99.36	126.20
Surface-Surface (no separation)	Coarse	99.24	49.07	80.62	93.79	85.47	34.50	69.13	71.25
	Medium	110.30	60.20	90.86	117.10	98.14	38.56	80.48	87.06
	Fine	128.10	74.76	106.40	148.90	120.30	45.58	99.38	110.60

In the case of a 28 *mm* ball, the singularity is comparable to the clamped-clamped case of an elastic wedge problem, while for the 56 *mm* ball it can be compared to the clamped-free case of an elastic wedge problem [70]. Also, the stresses in the contact region increase with an increase in femoral ball diameter. This suggests that wear of the material might be a concern in the contact region.

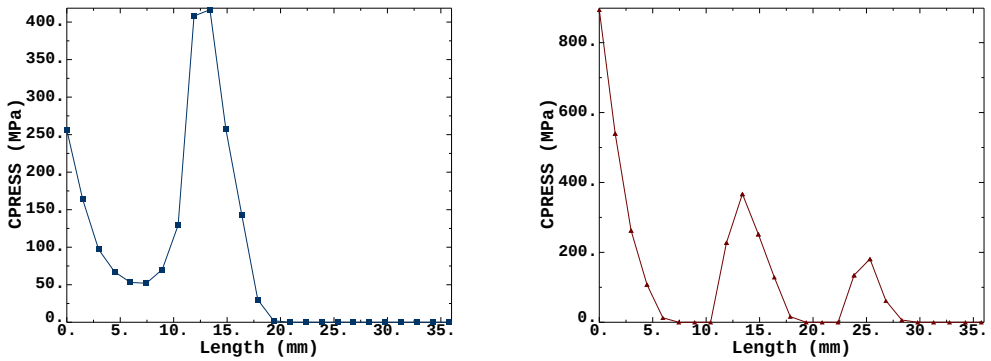

Figure 9.2: Contact pressure distribution under FC boundary condition and for surface to surface contact allowing separation; 28 mm ball (left) and 56 mm ball (right)

Figure 9.2 shows a plot of the contact pressure (output variable CPRESS in ABAQUS/Standard) over the length of the slave surface (path starting at point 1 and ending at point 4) for surface to surface contact interaction that also allows potential separation. It can be observed that the pressure peaks near point 2 for the 28 mm ball, and point 1 for the 56 mm ball diameter. The magnitude of the peak contact pressure for the 56 mm ball is higher than the peak contact pressure for the 28 mm ball. Figure 9.3 shows a plot of the frictional (contact) shear stress (output variable CSHEAR in ABAQUS/Standard) along the same path. The shear stress peaks near point 1 for both ball diameters.

Figure 9.4 shows plots for the magnitude of opening/overclosure (output variable COPEN in ABAQUS/Standard) of slave surface nodes over the length of the slave surface. At a slave node a positive value of COPEN corresponds to separation of the node away from the master surface, while a negative value of COPEN corresponds to penetration of the node into the master surface. It can be observed that there is a small amount of penetration of the slave nodes in the master surface for both cases. This behavior is due to the surface to surface contact formulation, which is enforced in an average sense [1]. It is not surprising that the locations of peak penetrations correspond to the locations of peak contact pressures as well (Figures 9.2 & 9.4). Also, a positive value of COPEN corresponds to zero pressure at a slave node as the node is not in contact with the master surface.

The difference in the predictions between the (surface to surface) contact formulations allowing separation versus no separation can be observed by comparing Figures 9.2 & 9.5, specifically in the vicinity of point 4 (approximately at 35 *mm* along the length of the path). The magnitudes of contact pressure and frictional shear stress are lower in the no separation case compared to the separation case at point 2 for 28 *mm* ball and point 1 for the 56 *mm* ball (corresponding to points of peak stresses in the contact region). This leads to lower von-Mises stress magnitudes that are tabulated in Table 9.1 & 9.2 (FC and PC cases). The contact opening/overclosure plot (Figure 9.7) for the no separation case, shows a small amount of opening (an artifact of the surface to surface formulation) near points 3 & 4 for the 28 *mm* ball and near points 2, 3, & 4 for the 56 *mm* ball. The openings in Figure 9.4 (close to point 4,

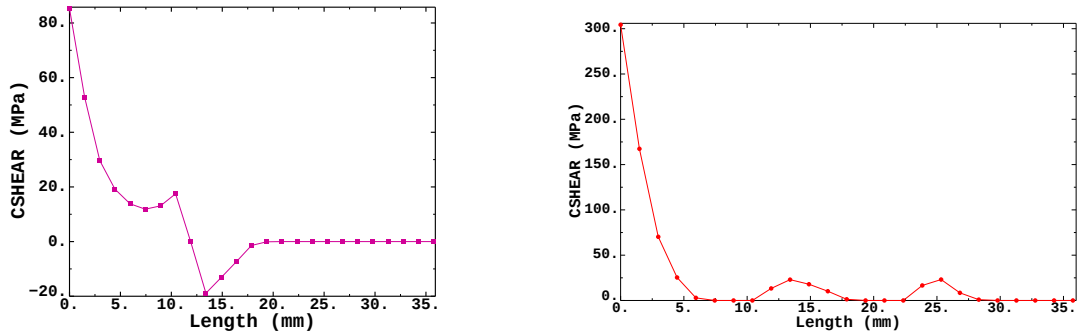

Figure 9.3: Frictional shear stress surface-surface separation case (FC boundary condition), 28 *mm* ball (left) and 56 *mm* ball (right)

surface to surface allowing possible separation) indicate that the surfaces are not in contact, resulting in zero pressure at these points. It is interesting to note that the corresponding results (Figure 9.5) for the surface to surface contact model that allows no separation shows that negative contact pressure develops in this region, suggesting that the surfaces have a tendency to separate, and are prevented from doing so by the *no separation* restriction.

Another region of the hip implant model that is of interest with respect to the stress distribution is its neck region. The magnitudes of the von Mises stress from the different simulations for the FC case are tabulated in Table 9.1. It can be observed that the values of the peak stress in the neck region, as obtained from the simulations

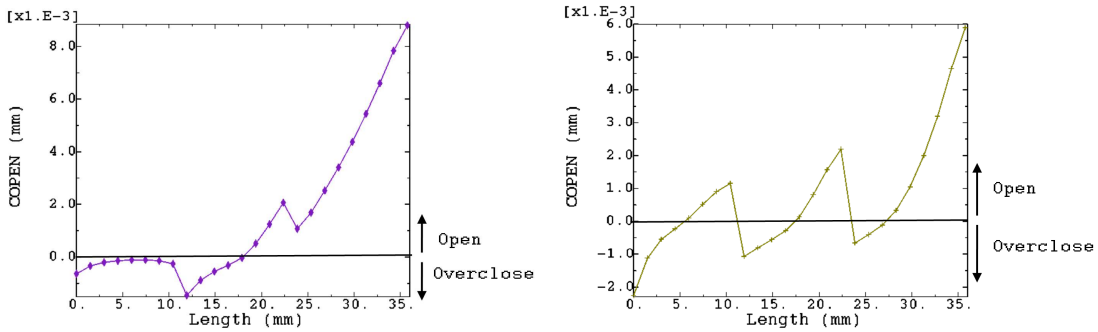

Figure 9.4: Contact opening surface-surface separation case (FC boundary condition), 28 *mm* ball (left) and 56 *mm* ball (right)

Table 9.2: 2D results of von Mises stress values for the PC case.

2.75 x BW=550lbs		28 mm ball diameter		56 mm ball diameter		28 mm ball diameter		56 mm ball diameter	
		CPS4 Stresses in neck region (MPa)	CPS4 Stresses in contact region (MPa)	CPS4 Stresses in neck region (MPa)	CPS4 Stresses in contact region (MPa)	CPE4 Stresses in neck region (MPa)	CPE4 Stresses in contact region (MPa)	CPE4 Stresses in neck region (MPa)	CPE4 Stresses in contact region (MPa)
Surface-Surface (separation)	Coarse	93.67	56.65	68.61	106.80	81.16	42.05	59.40	76.89
	Medium	96.65	71.42	70.76	137.40	84.27	48.57	61.73	95.94
	Fine	97.84	90.58	71.89	177.90	85.71	59.48	63.00	125.90
Surface-Surface (no separation)	Coarse	93.67	49.03	68.64	93.54	81.17	34.45	59.42	71.07
	Medium	96.65	60.28	70.78	116.90	84.27	38.50	61.74	86.86
	Fine	97.84	74.70	71.91	148.60	85.71	45.52	63.02	110.40

utilizing progressively finer meshes, do not converge well. This observation holds true under the assumptions of both separation and no-separation at the contact surfaces. In all the simulations, the peak stresses are generally observed adjacent to the fixed boundary constraints. The stresses are usually more uniform a few element lengths away from the boundary constraints. We observed based on the results of our simulations that, by considering the PC boundary conditions the stresses in the neck region converged well (Table 9.2). However, by modifying the boundary conditions from FC to PC, the stress distribution in the contact region did not change substantially. The results from the two-dimensional analysis suggest that the stresses in the neck region

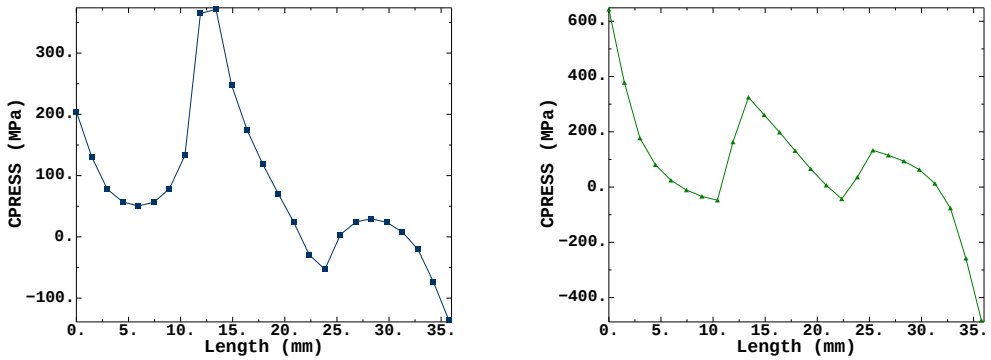

Figure 9.5: Contact pressure surface-surface no separation case (FC boundary condition), 28 mm ball (left) and 56 mm ball (right)

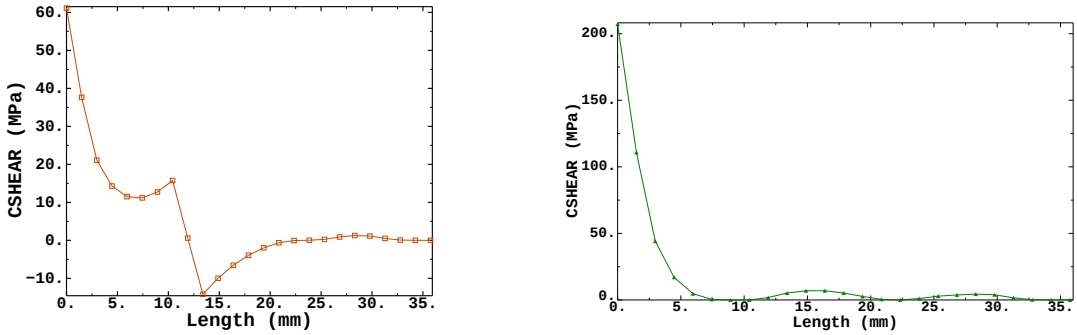

Figure 9.6: Contact shear pressure surface-surface no separation case (FC boundary condition), 28 mm ball (left) and 56 mm ball (right)

reduce with an increasing femoral ball size.

For the next set of simulations, the sharp corners in the ball and the stem from the earlier simulations (recall the earlier discussion on the elastic wedge and the associated singularity in stresses) are smoothed out by creating a fillet. We assume a fillet radius of 1 mm for the corners in both the ball and the stem. The contact model of surface to surface interaction that allows separation is assumed for all the simulations with a fillet. Figure 9.8 shows the contour plot of the von Mises stress distribution for the simulation with a 28 mm ball diameter. It can be observed that the location of the peak stress in the contact region occurs near point 2, which was also the location of the peak stress in the case without a fillet. We also note from Figure 9.8 that the fillet is discretized with one element for the simulations with the coarse and the

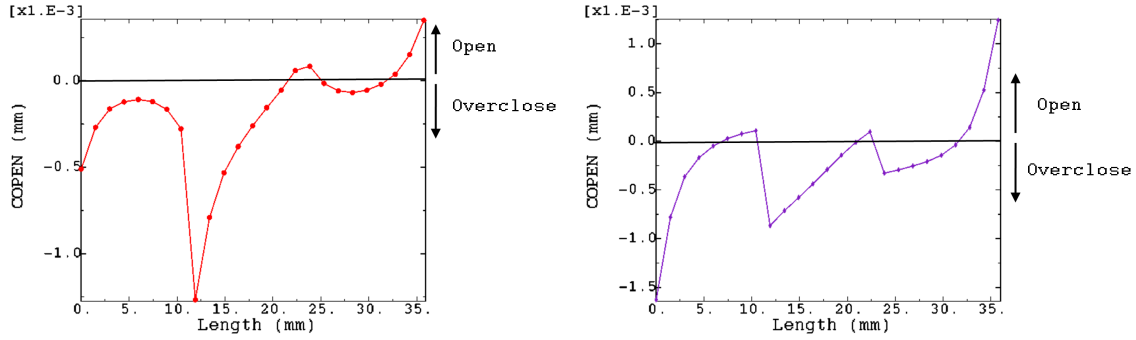

Figure 9.7: Contact opening surface-surface no separation case (FC boundary condition), 28 *mm* ball (left) and 56 *mm* ball (right)

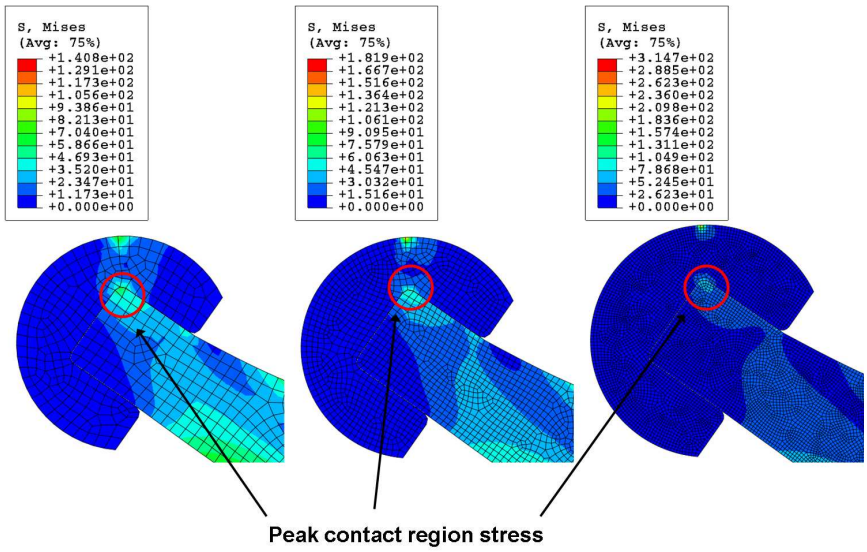

Figure 9.8: von Mises stress distribution with FC boundary condition and surface to surface contact allowing separation, with fillets at the sharp corners in the ball and stem; 28 *mm* ball

medium mesh. On the other hand, for the simulations with a fine mesh, the fillet is discretized with three elements. Thus, the stresses in the contact region seem to converge well as we transition from a relatively coarse to a fine mesh for both the FC and PC boundary conditions (numerical results are tabulated in Table 9.3).

For the simulation with a 56 *mm* diameter ball, the location of peak contact stress remained the same as for the case without the fillet (point 1 in both cases). However, even with the addition of a fillet, stresses for this case did not converge.

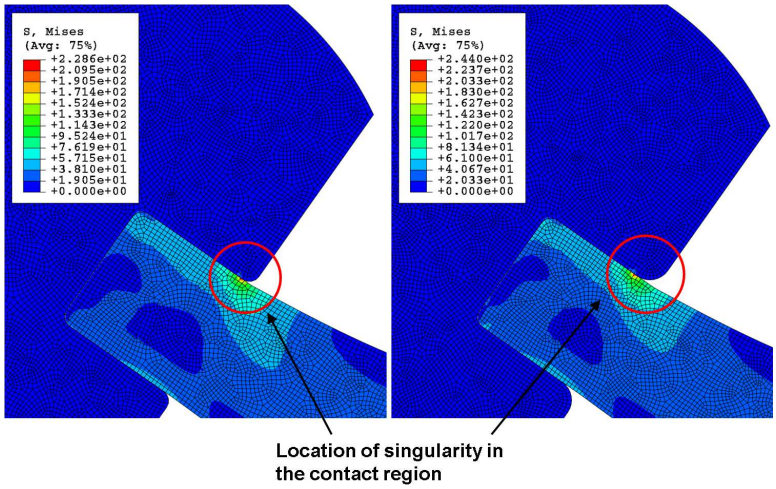

Figure 9.9: von Mises stress distribution with FC boundary condition and surface to surface contact allowing separation for a 56 mm ball diameter; effects of increasing the fillet radius.

The singularity was still observed as the mesh was refined, unlike in the 28 mm ball diameter case where the stresses appeared to have converged. Additional simulations, with an increased fillet radius of 2 mm, were also carried out. Figure 9.9 compares the stress distribution in the contact region for the simulations with 1 mm and 2 mm fillet radius, respectively. It can be observed (highlighted in the figure with a red circle) that the peak stress in the stem occurs in the vicinity of the point where the fillet curve of the femoral ball begins. The results with two different fillet radii suggest that an increase in the fillet radius only leads to a change in the location of peak stress, but the actual values of the stress do not converge.

Figure 9.10 shows the plot of the contact pressure (left) and the shear stress (right) on the stem between points 1 and 2. The contact pressure increases sharply in the vicinity of the point in the ball where the curve associated with the fillet begins. The shear stress is relatively lower compared to the contact pressure, but experiences a sharp increase approximately at the same location as the contact pressure. The sharp increase in the contact tractions in the aforementioned locations are not surprising in view of the results for the stresses in the underlying material which also experiences singular behavior in the same region. Table 9.3 provides the values of the von Mises

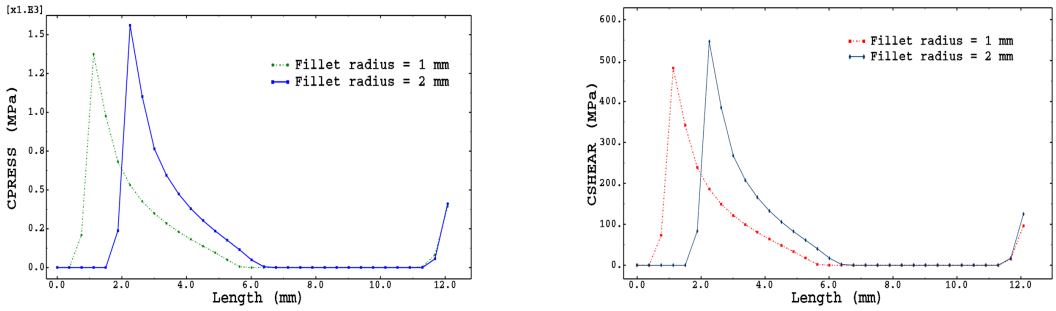

Figure 9.10: Contact pressure (left) and frictional shear stress (right) results comparing the effects of increasing the fillet radius (56 mm ball diameter with refined mesh)

stress for the simulations using fillets. We have only considered plane stress elements (element type CPS4 in ABAQUS) to present the results.

Table 9.3: von Mises stress for two-dimensional simulations with fillets.

2.75 x BW=550lbs surface-surface (separation)		28 mm ball diameter		56 mm ball diameter	
		CPS4 Stresses in neck region (MPa)	CPS4 Stresses in contact region (MPa)	CPS4 Stresses in neck region (MPa)	CPS4 Stresses in contact region (MPa)
FC	Coarse	95.86	59.20	77.87	142.50
	Medium	105.5	67.43	86.48	180.60
	Fine	124.8	73.16	103.5	236.30
PC	Coarse	92.85	59.19	66.46	142.1
	Medium	95.55	67.36	68.43	180.20
	Fine	96.84	73.07	69.14	235.90

We also carry out a simulation in which the ball is modeled as a rigid body, and a very refined mesh (element size of 0.005 mm) is used in the contact region where the stress singularity generally occurs. Figure 9.11 shows the von Mises stress distribution for the above simulation. We observe that the peak stress in the contact region increases to a magnitude of 657 MPa, which is relatively high, suggesting a stress singularity. Analytical solution [42] (page 111) for the case of a blunt wedge

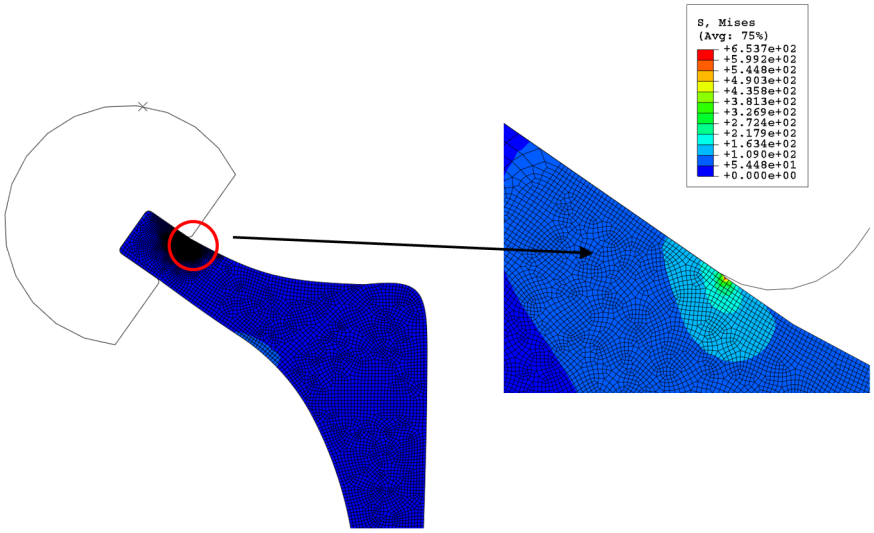

Figure 9.11: von Mises stress distribution for FC boundary conditions with surface to surface contact allowing separation and a 56 mm diameter ball; the ball is modeled as an analytical rigid body.

or a cone in contact with a flat surface suggests that a logarithmic singularity exits at the apex of the wedge or the cone. The loading on the ball (56 mm diameter) creates a situation in which the corner of the ball is indenting on the flat surface of the stem. A sharp corner may be thought of as a wedge, while a corner with a fillet may be thought of as a cone. The present problem may be thought of as the wedge or the cone indenting on a flat surface, resulting in a stress singularity.

9.1.2 Simulations using distributed load

All the simulations with distributed loading use a contact model with surface to surface interaction allowing separation. The distributed load is applied on the femoral ball by partitioning the top arc of the ball between points d and d' as described in Chapter 8, Figure 8.6. Thus, two areas, load area-1 and load area-2 that differ in the partition length, are created (see Chapter 8 for details) to apply the distributed load. The von Mises stress distributions for load area-1 and load area-2 for both the ball diameters are shown in Figure 9.12 and Figure 9.13, respectively. The location of peak stresses in the neck region and contact region for the simulations with distributed loads are approximately the same as the corresponding locations observed earlier for

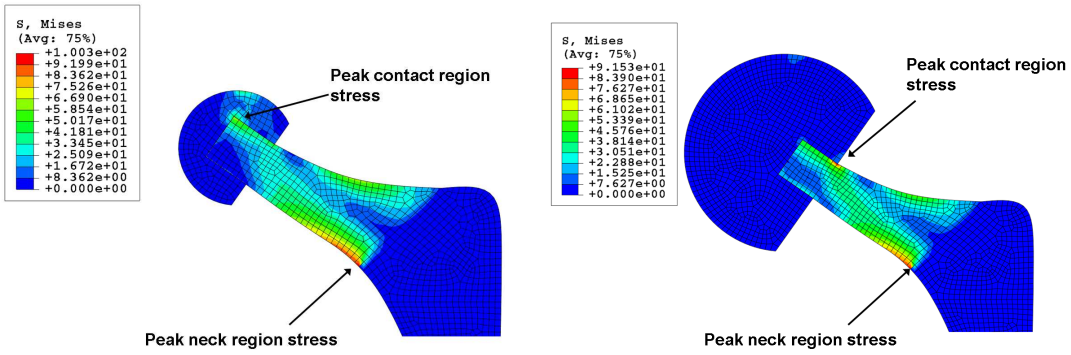

Figure 9.12: von Mises stress distribution for the distributed load area-1 with FC boundary condition; 28 *mm* ball (left) and 56 *mm* ball (right).

the simulations with a concentrated load.

Table 9.4: von Mises stress from two-dimensional simulations with distributed load area-1.

2.75 x BW=550lbs surface-surface (separation)		28 mm ball diameter		56 mm ball diameter		28 mm ball diameter		56 mm ball diameter	
		CPS4 Stresses in neck region (MPa)	CPS4 Stresses in contact region (MPa)	CPS4 Stresses in neck region (MPa)	CPS4 Stresses in contact region (MPa)	CPE4 Stresses in neck region (MPa)	CPE4 Stresses in contact region (MPa)	CPE4 Stresses in neck region (MPa)	CPE4 Stresses in contact region (MPa)
FC	Coarse	91.61	61.19	83.04	83.89	78.85	50.89	71.30	60.21
	Medium	102.10	78.30	93.19	112.00	90.84	60.25	82.66	76.63
	Fine	118.90	98.66	108.90	145.30	111.5	72.11	101.80	101.40
PC	Coarse	84.21	61.19	72.60	83.89	73.03	50.89	62.86	60.21
	Medium	86.91	78.30	74.71	112.00	75.83	60.25	65.21	76.63
	Fine	87.95	98.66	75.86	145.30	77.10	72.11	66.50	101.40

The magnitudes of the von Mises stress for the simulations with load area-1 are tabulated in Table 9.4. The stress magnitudes for the 28 *mm* diameter ball are approximately 10% lower in the neck region, when compared to the cases with a concentrated load. This trend is observed from both the plane-strain and the plane-stress simulations. On the other hand, the stresses in the contact region increased by

approximately 8%. All of the above observations hold for both FC and PC boundary conditions. For the 56 *mm* diameter ball, the stress magnitudes increased approximately 5% in the neck region, while in the contact region they reduced approximately 22% compared to the cases with a concentrated load. These observations hold for both plane-strain and plane-stress simulations and for both FC and PC boundary conditions.

In the second set of simulations with distributed loading (load area-2), the stress in the neck region for a 28 *mm* ball are approximately 4% higher compared to the cases with a concentrated load, while in the contact region the stress is approximately 26% lower. For the 56 *mm* diameter ball on the other hand, the stresses reduce by approximately 8% and increase by approximately 13%, in the neck and the contact region, respectively. These observations hold for both plane-strain and plane-stress simulations and for both FC and PC boundary conditions. The von Mises stress magnitudes for simulations corresponding to load area-2 are tabulated in Table 9.5.

Table 9.5: von Mises stress from two-dimensional simulations with distributed load area-2.

2.75 x BW=550lbs surface-surface (separation)		28 mm ball diameter		56 mm ball diameter		28 mm ball diameter		56 mm ball diameter	
		CPS4 Stresses in neck region (MPa)	CPS4 Stresses in contact region (MPa)	CPS4 Stresses in neck region (MPa)	CPS4 Stresses in contact region (MPa)	CPE4 Stresses in neck region (MPa)	CPE4 Stresses in contact region (MPa)	CPE4 Stresses in neck region (MPa)	CPE4 Stresses in contact region (MPa)
FC	Coarse	101.90	47.21	74.64	121.50	87.89	32.14	63.89	88.36
	Medium	113.10	56.75	84.42	154.30	100.80	35.36	74.66	108.90
	Fine	131.30	69.68	99.11	199.50	123.30	42.36	92.37	142.00
PC	Coarse	97.56	47.21	62.00	121.50	84.57	32.14	53.62	88.36
	Medium	100.80	56.75	63.94	154.30	87.95	35.36	55.68	108.90
	Fine	102.00	69.68	64.82	199.50	89.46	42.36	56.79	142.00

9.1.3 Analytical model

In this section we present the results from the analytical model of the neck region of the stem, that was presented in Chapter 8. The objective of this part of the work

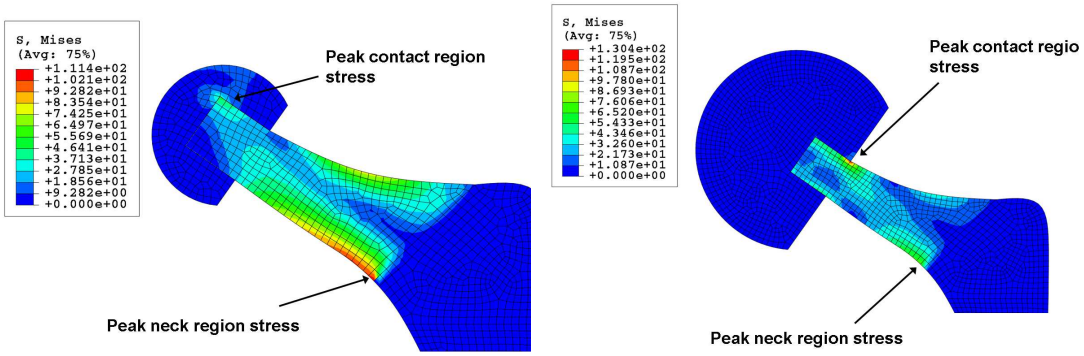

Figure 9.13: von Mises stress distribution for the load area-2 case (FC boundary condition), 28 mm ball (left) and 56 mm ball (right)

is to obtain an *approximate* estimate for the bending stresses in the neck region and correlate these values with the corresponding results from the FE simulations. We recall that the simplified geometry for the neck region consists of a stubby cantilever beam subjected to a combination of bending and axial end loads. In Chapter 8, we discussed similarities between the present model and that of a gear tooth subjected to a concentrated load.

Table 9.6: Comparison of bending stresses between the analytical model and FE simulations.

Ball size (mm)	2D implant FEA $\sigma_{11}(MPa)$	Analytical $\sigma_{11}(MPa)$
28	-85.20	-72.11
56	-66.80	-58.88

The bending stresses obtained at point d (Figure 8.10, Chapter 8) are tabulated in Table 9.6. The stresses obtained from a plane stress FE analysis are compared with the stresses computed from the analytical model. The plane-stress FE results predict that the stress reduces by 21.5% with an increase in the femoral ball size from 28 mm to 56 mm. The negative sign indicates that the point d is in compression The corresponding analytical calculations predict a 18.3% reduction in stress with a similar increase in the size of the femoral ball. The results obtained from the analytical

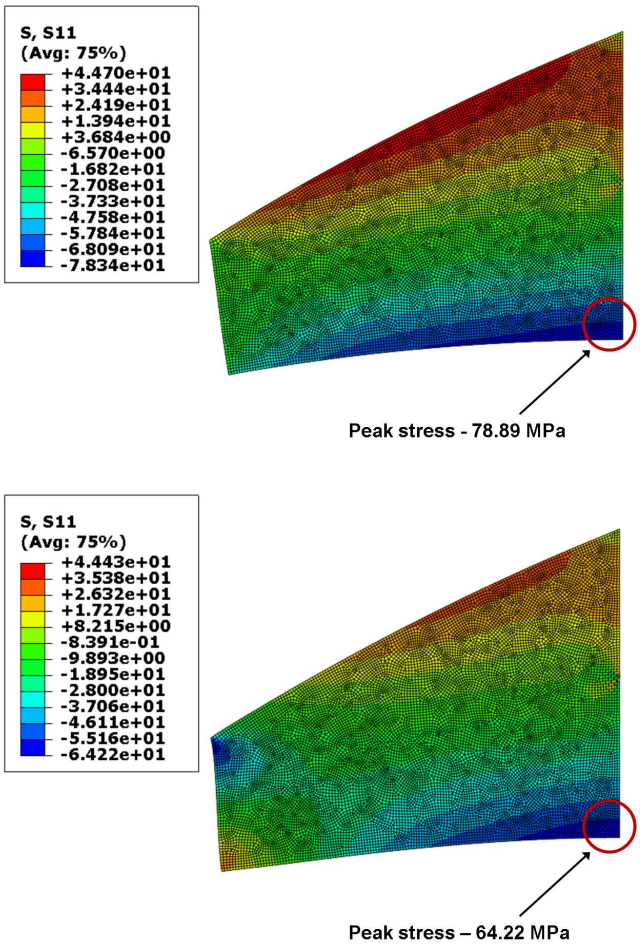

Figure 9.14: Axial stress plot showing the peak magnitude obtained using FEA for the geometry used for the analytical model, 28 *mm* ball (top) and 56 *mm* ball (bottom).

model were also cross-checked by performing a FE analysis of the simplified geometry (used for the analytical model).

Figure 9.14 shows the stress contours obtained from the FE analysis of the simplified geometry used in the analytical model. This analysis was performed under the assumption of plane-stress conditions in the implant. The reduction in stress with an increasing ball diameter, as predicted by the results of the aforementioned FE analysis, is approximately 18.5%. This trend matches very well with the analytical solution. Table 9.7 compares the results from the plane-stress FE analysis of the actual implant with the analytical solution and the results from an FE analysis of the simplified geometry.

Table 9.7: Comparison of bending stresses obtained based on (i) plane-stress FE analysis of implant, (ii) analytical model, and (iii) FE analysis on the simplified geometry.

Ball size (mm)	2D implant FEA $\sigma_{11}(MPa)$	Analytical $\sigma_{11}(MPa)$	FEA simplified geometry $\sigma_{11}(MPa)$
28	-85.20	-72.11	-78.89
56	-66.80	-58.88	-64.22

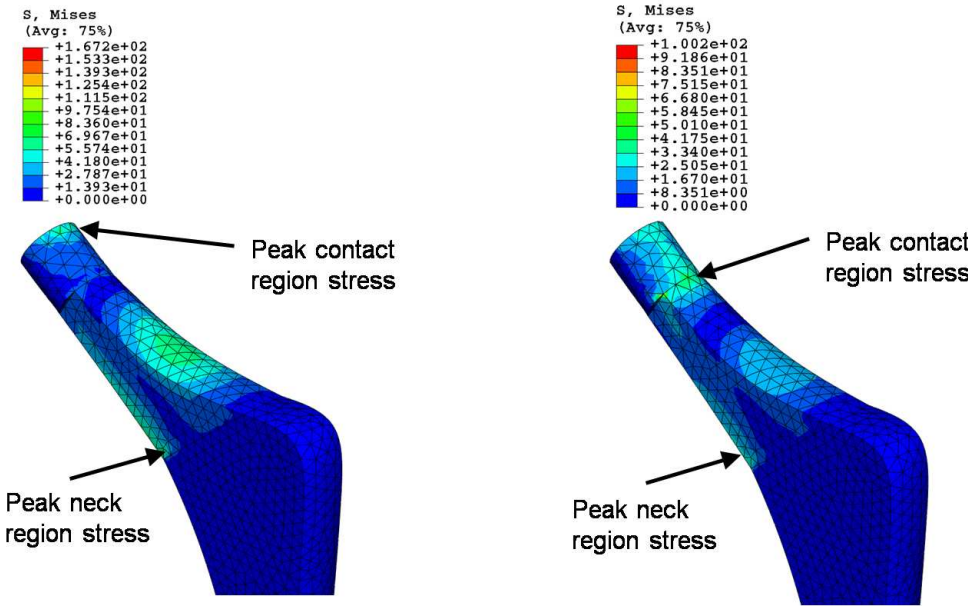

Figure 9.15: von Mises stress distribution surface-surface separation case (FC boundary condition), 28 mm ball (left) and 56 mm ball (right)

9.2 Three-dimensional Analysis

In this section we discuss the results from simulations based on a three-dimensional model of the hip implant. For reasons to be discussed later, the contact model used for these simulations assume surface to surface interaction with the possibility of separation. We note that the three-dimensional model of the ball-implant assembly eliminates the wedge geometry and the associated stress singularity. As a result we observe good convergence of stress values in the contact region (Table 9.7).

The location of peak stresses is consistent with the observations from the two-dimensional analysis. As observed in the two-dimensional analysis, the stresses in

the contact region increase with increasing femoral ball size. The magnitudes of the stresses in the neck region are about 12-15% higher (Table 9.8) than the predictions of the two-dimensional analysis. We comment on the possible origin of this difference in the discussion section. However, the general trend of non-convergence in the values of the stress in the neck region for FC boundary condition, and good convergence for PC boundary condition that were observed in the two-dimensional analysis appear to carry over to the three-dimensional analysis as well. Additionally, the reduction in the stresses in the neck region due to an increased femoral ball size observed in the two-dimensional analysis is confirmed by the results of the present three-dimensional study.

Table 9.8: von Mises stress from three-dimensional simulations under both FC and PC boundary conditions.

2.75 x BW=550lbs		28 mm ball diameter		56 mm ball diameter	
		C3D10M Stresses in neck region (MPa)	C3D10M Stresses in contact region (MPa)	C3D10M Stresses in neck region (MPa)	C3D10M Stresses in contact region (MPa)
Surface-Surface (separation) FC case	Coarse	117.6	90.6	95.65	97.41
	Medium	124.7	89.80	102.1	125.0
	Fine	128.7	95.73	106.1	124.2
Surface-Surface (separation) PC case	Coarse	108.7	90.78	80.28	97.41
	Medium	109.8	89.68	80.56	124.5
	Fine	109.8	95.62	80.87	123.7

9.3 Fatigue Life Prediction

Fatigue failure of hip implants is another important aspect to consider in considering various design alternatives. The loading on the implant due to body weight leads to a non-zero average mean stress level. A detailed description of the empirical laws, that (phenomenologically) take into account the effects of mean stress, was presented in Chapter 8. In this part of the study, we compute the number of cycles to failure (of the implant), N_f, based on the Soderberg, Goodman, Gerber, and Morrow's laws.

To determine the number of cycles to failure, we make use of the values of the von Mises stress from the neck region in the three-dimensional analysis of a hip implant with a 28 mm diameter femoral ball. We pick the smaller ball diameter because the results presented in the earlier section suggested that the stresses in the neck region decrease with an increase in the size of the femoral ball.

The stress amplitude, σ_a, is computed based on the values of the maximum and the minimum von Mises stress in the neck region of the stem. The maximum von Mises stress, σ_{max}, for a single stance phase of gait, as obtained from the three-dimensional analysis, is 109.8 MPa. The minimum von Mises stress, σ_{min}, is assumed to be 0 MPa. The relevant material parameters for the titanium alloy, Ti-6Al-4V, are tabulated in Table 9.9.

Table 9.9: Ti-6Al-4V material properties, ([57] and [78]).

Material	Yield strength σ_y (MPa)	Ultimate strength σ_u (MPa)	Fatigue strength coefficient $\acute{\sigma_f}$ (MPa)	Fatigue strength exponent b
Ti-6AL-4V	825.0	895.0	2030.0	-0.104

The number of cycles to failure computed using the Soderberg, Goodman, Gerber, and Morrow's laws all resulted in a value that corresponds to essentially an infinite fatigue life of the implant. It should also be noted that the stress amplitude, σ_a, is 54.9 MPa and well below the *endurance limit* for the titanium alloy. Figure 9.16 shows the S-N curve for Ti-6Al-4V alloy, and clearly suggests that for a stress amplitude of 54.9 MPa the number of cycles to failure is infinite. Previous studies ([65] and [46]) have generally assumed a fatigue life that is greater than 10^9 cycles to be infinite life. In an another study [8], the fatigue life for different designs of the implant were computed, by considering the number of steps taken for walking, running and stair climbing. The study [8] predicted a total life varying between 9.8 years to 100 years for the different implant designs.

9.4 Discussion

In this study we carry out a detailed stress analysis of an artificial hip implant. Specifically, we investigate the effects of varying the size of the femoral ball on the

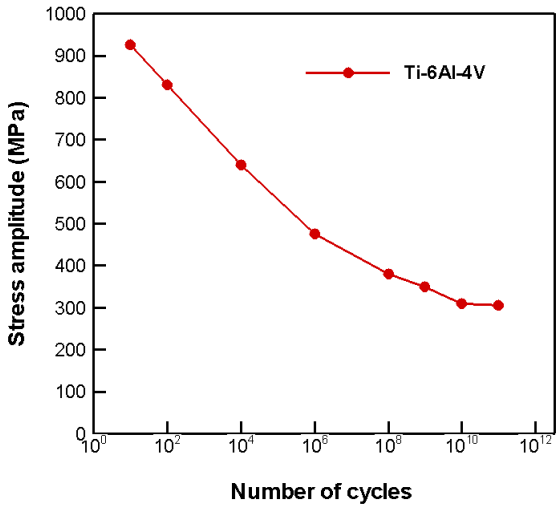

Figure 9.16: S-N curve for Ti-6Al-4V [46].

stress distribution in the stem of the implant. A study of this nature is expected to provide valuable information on whether the current trend of using a larger femoral ball, that is beneficial in some respects, negatively impacts the long term durability of the implant. A two-dimensional model of the implant is first investigated because it is simpler in terms of finite element meshing and mesh-refinement, as compared to a more realistic three-dimensional model. Mesh refinement allows us to perform mesh convergence studies. The present study also investigates the interaction between the femoral ball and the implant stem. It is important to understand this interaction because it can potentially provide input to models of wear mechanisms at the stem-ball interface. We follow up the two-dimensional study with an analysis of a more realistic three-dimensional model of the hip implant. In the following paragraphs we discuss the results of this study with special emphasis on (i) comparisons between the results with a concentrated load versus those with a distributed load, (ii) results from a simple analytical model, (iii) comparisons between results from two-dimensional and three-dimensional simulations, (iv) the contact conditions between the ball and the stem, and (v) the long term durability based on the stress distribution in the neck region.

Generally, the femoral ball experiences a non-uniformly distributed load from the

pelvic region. But this non-uniform load has often been idealized as a concentrated load in earlier studies of hip implants. The results from the two different kinds of loading suggest that the locations of the peak stress in the contact and the neck regions do not depend on whether we use the concentrated or the distributed idealization for the load. The magnitude of the stresses from the concentrated load turns out to be approximately the average of the predictions based on the two different kinds of distributions assumed for the load. While the area chosen to apply the distributed load is in the vicinity of the concentrated load, this region might not be symmetric about the point at which the concentrated load is applied, which is what we have assumed in this study. (We have tried to get a distribution from a resultant; generally one carries out the converse operation in Statics.) This could explain the variations in the stress magnitudes observed between the distributed and the concentrated loading cases.

The geometry utilized for the analytical calculations was based on the neck region of the implant. With further simplifications (without the curved outer boundaries and the fillets), we were able to relate this geometry to that of a gear tooth. This allowed us to utilize an analytical expression available in the literature for the bending stresses in the gear tooth. Based on this approach, the reduction in stresses with increasing femoral ball size was computed to be approximately 3% less compared with the percentage reduction in stresses from the FE simulations of the implant. This is a fairly good match given the amount of simplifications made in the analytical model. To further validate the solution obtained from the analytical model, we performed an FE analysis of the simplified geometry assuming plane stress conditions. The percentage reduction in stress (with increasing ball size) from the simplified FE analysis is off by approximately 0.3% when compared with the analytical calculations. This suggests that the methodology utilized in computing the bending stresses from the analytical model was reasonable.

The results obtained using a plane stress formulation and a plane strain formulation are about 12-14% and 24-28% lower, respectively, compared to the predictions from the three-dimensional model. Firstly, it turns out that the volume of material

in the two-dimensional model is about 27% higher compared to the volume for the three-dimensional model. This difference in volume is due to the constant out-of-plane thickness for the plane problems. This results in the two-dimensional model being effectively (and in a structural sense) stiffer compared to the three-dimensional model, thereby leading to lower displacements and stresses. This accounts for the 12-14% difference in stress magnitudes between the plane stress and the three-dimensional simulations. The plane-strain formulation is similar to a plane-stress formulation except for the use of the so-called plane-strain modulus. The original modulus is reduced by a factor of (1-ν^2) to yield the plane-strain modulus and this results in an additional 13% reduction in stress values for the plane-strain case compared to the three-dimensional results. Thus, the difference in stresses between the plane-strain and the three-dimensional results is due the combined effects of increased material volume in the model and the Poisson's effect associated with the plane-strain constraint.

The peak value of stress in the neck region decreases with an increase in the femoral ball size. Latham & Goswami [48] made similar observations from their studies of hip implants. However, an increase in the size of the femoral ball leads to an increase in the stresses in the contact region. This observation is important because of its potential implications for material wear in this region. During assembly of the implant, the femoral ball is slipped on top of the femoral stem. It is possible (though unlikely) for the ball to slide and tilt by a small amount depending on the nature of the loading. The simulations that can potentially lead to separation after contact allow a clearance (of the order of microns) to develop between the ball the stem (positive values of contact clearance in Figure 9.3). On the other hand, the simulations that model contact with no separation force the slave surface to remain attached to the master surface once they come in contact. The latter may not be an accurate reflection of the physics at the interface between the stem and the femoral ball. In the above sense, a contact formulation that allows potential separation probably simulates the reality more accurately. Based on such considerations we only assumed contact with potential separation for all the three-dimensional simulations.

As discussed earlier, the stresses in the neck region of the implant reduced with an increasing ball size. Therefore, we use the stresses obtained with a 28 mm size ball in the fatigue life calculations. The results suggest that the total fatigue life for a single stance phase of gait is infinite. However, the prediction might lead to a finite value for the fatigue life if one considered the effects of other daily life activities.

CHAPTER 10: CONCLUSIONS AND FUTURE WORK

10.1 Conclusions

In this study, the mechanical response of an artificial hip implant under a single stance phase of gait is investigated. In particular, we investigate the effects of using a larger size femoral ball on the stress distribution in the stem of the implant. A two-dimensional model of the implant including the femoral ball was analyzed initially. We determined the applicability of the results from the two-dimensional model by comparing these results with the corresponding results from a fully three-dimensional analysis of the implant. The modern implant is designed such that the femoral ball and the stem are separate components, and these components are assembled during surgery. Therefore, it is essential to model the appropriate contact interaction between the femoral ball and the stem, and this aspect is investigated in details. Within this basic framework, we also investigate the influence of the mesh size on the solutions, thereby ensuring that we rely on a converged solution for making predictions for the long term durability of the implant. An analytical model for the neck region of the stem is developed with the aim of getting a quick and an approximate estimate for the bending stress in the neck region of the stem. This study also examines how the long term durability of hip implants is affected by an increase in the femoral ball size. In the following paragraphs, we summarize some of the key observations made from the results of this study.

One of the main objectives of this work is to determine the effects of an increasing ball size on the stress distribution in the neck region of the implant. The results suggest that as the femoral ball size is increased, the stresses reduce in the neck region but in turn increase in the region of contact between the stem and the ball. Although the stress magnitudes for both ball sizes are well within the yield limit, the higher stresses due to the larger ball size could lead to wear implications in the

contact region. These observations are consistent in both the two-dimensional and the three-dimensional models of the implant.

The two-dimensional model was analyzed using both the assumptions of plane stress and plane strain deformations. If the implant is assumed to have made a strong bond within the femur without any leverage for movement, then the strain in the third direction can be considered to be zero. In such a case the plane strain condition would be more appropriate. In a situation where the implant does not form a solid bond with the bone, allowing the implant to expand freely in the thickness direction, the stress in the third direction can be assumed to be zero. This would result in a plane stress condition. Therefore, assuming that the real situation is somewhere in between these two extremes, we obtain results for both these limiting cases. The magnitude of the bending stress predicted under the plane strain assumption is approximately 13% lower compared to the magnitude obtained using the plane stress assumption.

The two-dimensional model was also utilized to investigate the contact interaction between the ball and the stem. A contact formulation that is based on surface to surface interaction (as opposed to node to surface interaction) with the possibility of separation between the slave and master surface appeared to be the proper choice for simulating the ball and stem interaction.

The results obtained using the idealization of a concentrated force are compared to the results obtained with distributed loading. Based on the results it appears that the idealization of a concentrated load, that is generally used in most hip implant simulations, is reasonable.

An analytical model was developed to obtain approximate estimates for the bending stresses in the neck region. The stress magnitudes predicted using the analytical model were approximately 15% lower compared to the stress magnitudes estimated with the two-dimensional analysis of the implant. The analytical model also predicted the percentage reduction in stresses for an increasing ball size to within (approximately) 5% of the two-dimensional analysis of the implant.

The long term durability (fatigue life) for this particular design of the implant was determined in this study. The fatigue life calculations suggest that the implant has

an infinite life (with respect to the average human life) under a single stance phase of gait loading condition. However, fatigue life might lead to a finite value if we consider the effects of other daily life activities.

10.2 Future Work

This area of research has a lot of scope for future work. The current work has laid out a good foundation on some of the assumptions that can be made while determining the durability of a hip implant. The following are some of the possible areas of future work.

1. The issue of wear in the contact region for a larger sized ball must be investigated further.

2. A better design for the implant can be developed to avoid the indentation of the ball on the stem, that appears to be leading to singular stresses.

3. In this study, a single stance phase of gait loading was considered. The other types of loading that an implant is generally subjected to during daily life activities must be considered. This would provide a better estimate of the fatigue life for a particular choice of an implant design.

4. The consideration of forces acting on the implant due to the surrounding muscles and ligaments would be another refinement that can be made to this current study.

[1] ABAQUS V6.7. 2007. *User's manual.* Dassault Systèmes Simulia, Providence RI, USA.

[2] Abboud JA and SK Abboud. 2008. *No more joint pain.* Yale University Press, New Haven, London, UK.

[3] Argyris JH and S Kelsey. 1954 and 1955. Energy theorems and structural analysis. *Aircraft Engineering* **26, 27**.

[4] Bathe KJ. 2002. *Finite element procedures.* Prentice-Hall, Inc, Englewood Cliffs, NJ, USA.

[5] Barenblatt GI. 1959. The formation of equilibrium cracksduring brittle fracture, general ideas and hypothesis, axially symmetric cracks. *Prikl. Mat. Mekh.* **23**: 434-444.

[6] Barua A, and K Bose. 2007. On the optimum choices of cohesive-zone parameters describing initiation and propagation of cracks. *2007 ECCOMAS Thematic Conference on Mechanical Response of Composites.*

[7] Behnke RS. 2006. *Kinetic anatomy.* Human Kinetics, Inc. Champaign, IL, USA.

[8] Bennett D and T Goswami. 2007. Finite element analysis of hip stem designs. *Materials and Design* **29**: 45-60

[9] Bergmann G, G Deuretzbacher, M Heller, F Graichen, A Rohlmann, J Strauss and GN Duda. 2001. Hip contact forces and gait patterns from routine activities *Journal of Biomechanics* **34**: 859–871.

[10] Bogetti TA, CPR Hoppel, VM Harik, JF Newill and BP Burns. 2004. Predicting the nonlinear response and progressive failure of composite laminates. *Composites Science and Technology.* **64**: 329-342.

[11] Bogetti TA, CPR Hoppel, VM Harik, JF Newill and BP Burns. 2004. Predicting the nonlinear response and progressive failure of composite laminates: correlation with experimental results. *Composites Science and Technology.* **64**: 477-485.

[12] Borst RD. 2006. Modern domain-based discretization methods for damage and fracture. *International Journal of Fracture.* **138**: 241-261.

[13] Buford A. and T Goswami. 2004. Review of wear mechanisms in hip implants: Paper I - General. *Materials and Design* **25**: 385-393.

[14] Chang FK and MH Chen. 1987. The in-situ ply shear strength distributions in graphite/epoxy laminated composites. *Journal of Composite Materials.* **21**: 708-733.

[15] Chang KY, S Liu, FK Chang. 1991. Damage tolerance of laminated composites containing an open hole and subjected to tensile loadings. *Journal of COmposite Materials* **25**: 274-301.

[16] Charnley J and DK Halley. 1975. Rate of wear in total hip replacement. *Clinical Orthopedics and Related Research* **112**: 170-179.

[17] Clough RW. 1960. The finite element methodin plane stress analysis. *Proceedings, Second ASCE Conference on Electronic Computation*, Pittsburgh, PA: 345-378.

[18] Courant R. 1943. Variational methods for the solution of problems of equilibrium and vibrations. *Bulletin of the American Mathematical Society* **49**: 1-23.

[19] Cox B and Q Yang. 2006. In quest of virtual tests for structural composites. *Science* **314**: 1102-1107.

[20] Cuntze RG and A Freund. 2004. The predictive capability of failure mode concept-based strength criteria for multi-directional laminates. *Composites Science and Technology.* **64**: 343-377.

[21] Cuntze RG and A Freund. 2004. The predictive capability of failure mode concept-based strength criteria for multi-directional laminates: part B. *Composites Science and Technology.* **64**: 487-516.

[22] Daniel IM and O Ishai. 1994 *Engineering Mechanics of Composite Materials.* Oxford University Press.

[23] Davila CG, PP Camanho, and CA Rose. 2005. Failure criteria for FRP laminates. *Journal of Composite Materials* **39**: 323-345.

[24] Dugdale DS. 1960. Yielding of steel sheets containing slits. *Journal of Mechanics and Physics of Solids* **8**: 100-108.

[25] Fish J and T Belytschko. 2007. *A first course in finite elements.* John Wiley & Sons Ltd, Southern Gate, Chichester, West Sussex PO19 8SQ, England.

[26] Found MS and SB Kanyanga. 1996. The influence of two-stage loading on the longitudinal splitting of unidirectional carbon/epoxy laminates. *Fatigue and Fracture of Engineering Materials and Structures* **19**: 65-74.

[27] Frankel VH and AH Burstein. 1970. *Orthopaedic biomechanics.* Lea & Febiger, Philadelphia, USA.

[28] Grill A. 2003 Diamond-like carbon coatings as biocompatible materials-an overview. *Diamond and related Materials* **12**: 166–170.

[29] Hallet SR and MR Wisnom. 2005 Numerical investigation of progressive damage and the effect of layup in notched tensile tests. *Journal of Composite Materials.* **40**: 1229-1245.

[30] Hallet SR, WG Jiang, B Khan, MR Wisnom. 2008 Modelling the interaction between matrix cracks and delamination damage in scaled quasi-isotropic specimens. *Composites Science and Technology.* **68** 80-89.

[31] Hashin, Z. and A Rotem. 1973. A Fatigue Failure criterion for fiber reinforced materials. *Journal of Composite Materials.* **7**: 448-464.

[32] Hashin Z. 1980. Failure criteria for unidirectional fiber composites. *Journal of Applied Mechanics.* **47**: 329-334.

[33] Hashin Z. 1981. Fatigue Failure criteria for unidirectional fiber composites. *Journal of Applied Mechanics.* **48**: 846-852.

[34] Herakovich CT. 1998. *Mechanics of fibrous composites.* John Wiley & Sons, Inc.

[35] Hinton MJ, AS Kaddour and PD Soden. 2004. A further assessment of the predictive capabilities of current failure theories for composite laminates: comparison with experimental evidence. *Composites Science and Technology.* **64**: 549-588.

[36] Hung J-P, J-H Chen, H-L Chiang, and J S-S Wu. 2004. Computer simulation on fatigue behavior of cemented hip prostheses: a physiological model. *Computer Methods and Programs in Biomedicine* **76**: 103-113.

[37] Hull D and TW Clyne. 1996 *An introduction to composite materials.* Cambridge University Press.

[38] Hutchinson JW and Z Suo. 1992. Mixed mode cracking in layered materials. *Advances in Applied Mechanics.* **29**: 63-191.

[39] Iorio R, WJ Robb, WL Healy, DJ Berry, WJ Hozack, RF Kyle, DG Lewallen, RT Trousdale, WA Jiranek, VP Stamos and BS Parsley. 2008. Orthopaedic surgeon workforce and volume assessment for total hip and knee replacement in the United States: preparing for an epidemic. *The Journal of Bone & Joint Surgery* **90**: 1598-1605.

[40] Jamison RD. 1985. The role of microdamage in tensile failure of graphite/epoxy laminates. *Composites Science and Technology.* **24**: 83-89.

[41] Jiang WG, SR Hallet, BG Green and M Wisnom. 2006. A concise interface constitutive law for analysis of delamination and splitting in composite materials and its application to scaled notched tensile specimens. *International Journal for Numerical Methods in Engineering* **69**: 1982-1995.

[42] Johnson KL. 1985. *Contact Mechanics*, Cambridge University Press, New York, NY, USA.

[43] Kachanov LM. 1958. Time of the rupture process under creep conditions, *Izv. Akad. Nauk. USSR. Otd. Tekhn. Nauk.* **8**: 2631.

[44] Katoozian H.and DT Davy. 2000. Effects of loading conditions and objective function on three-dimensional shape optimization of femoral components of hip endoprostheses. *Medical Engineering & Physics* **22**: 243–251.

[45] Kayabasi O and F Erzincanli. 2006. Finite element modelling and analysis of a new cemented hip prosthesis. *Advances in Engineering Software* **37**: 477–483.

[46] Kayabasi O and B ekici. 2006. The effects of static, dynamic and fatigue behavior on three-dimensional shape optimization of hip prosthesis by finite element method. *Materials and Design* **28**: 2269-2277.

[47] Kuraishi A, SW Tsai and K-S Liu. 2002. A progressive quadratic failure criterion, Part B. *Composites Science and Technology.* **62**: 1682-1696.

[48] Latham B and T Goswami. 2004. Effect of geometric parameters in the design of hip implants paper IV. *Materials & Design* **25**: 715-722.

[49] Linde P, J Pleitner, HD Boer, and C Carmone. 2004. Modelling and simulation of fibre metal laminates. *2004 ABAQUS User's Conference.*

[50] Lippert LS. 2006. *Clinical kinesiology and anatomy.* F.A.Davis Company, Philadelphia, PA, USA.

[51] Liu K-S and SW Tsai. 1998. A progressive quadratic failure criterion of a laminate. *Composites Science and Technology.* **58**: 1023-1032.

[52] LS-DYNA. 2007. *Commerical finite element software.* Livermore Software Technology Corp., Livermore CA, USA.

[53] Maimi P, PP Camnaho, JA Mayugo, and CG Davila. 2006. A thermodynamically consistent damage model for advanced composites. *NASA/TM-2006-214282.*

[54] Maimi P, PP Camnaho, JA Mayugo, and CG Davila. 2007. A continuum damage model for composite laminates: Part II - Computational implementation and validation. *Mechanics of Materials.* **39**: 909-919.

[55] Murakami S and N Ohno. 1980. A Continuum Theory of Creep and Creep Damage, In: Ponter, A.R. S. and Hayhurst, D.R. (eds), *Creep in Structures, 3rd IUTAM Symposium on Creep in Structures* Berlin, Springer: 422-444.

[56] Nairn JA. 1989. The strain energy release rate of composite microcracking: a variational approach. *Journal of Composite Materials* **23**: 1106-1129.

[57] Niinomi M. 1998. Mechanical properties of biomedical titanium alloys. *Material Science and Engineering.* **A243**: 231-236.

[58] Nalla RK, JH Kinney, SJ Marshall and RO Ritchie. 2004. On the in vitro Fatigue Behavior of Human Dentin: Effect of Mean Stress. *Journal of Dental Research* **83**: 211-215.

[59] Parvizi A, K Garrett, and J Bailey. 1978. Constrained cracking in glass fibre-reinforced epoxy xross-ply laminates. *Journal of Material Science.* **13**: 195-201.

[60] Niinomi M. 2007. Fatigue characteristics of metallic biomaterials. *International Journal of Fatigue* **29**: 992–1000.

[61] Pinho ST, CG Davila, PP Camanho,and L Iannucci. 2005. Failure models and criteria for FRP under in-plane or three-dimensional stress states including shear non-linearity. *NASA/TM-2005-213530.*

[62] Puck A and H Schürmann. 1998. Failure analysis of FRP laminates by means of physically based phenomenological models. *Composites Science and Technology* **58**: 1045-1068.

[63] Puck A and H Schürmann. 2002. Failure analysis of FRP laminates by means of physically based phenomenological models - Part B. *Composites Science and Technology* **62**: 11633-11672.

[64] Pyburn E and T Goswami. 2004. Finite element analysis of femoral components paper III - hip joints. *Materials & Design* **25**: 705–713.

[65] Senalp AZ, O Kayabasi and H Kurtaran. 2007 Static, dynamic and fatigue behavior of newly designed stem shapes for hip prosthesis using finite element analysis. *Materials and Design* **28**: 1577–1583.

[66] Seng CT. 1991. A progressive failure model for composite laminates containing openings. *Journal of Composite Materials* **25**: 556-577.

[67] Shahid I and FK Chang. 1995. An accumulative damage model for tensile and shear failures of laminated composite plates. *Journal of Composite Materials.* **29**: 926-981.

[68] Soden PD, AS Kaddour and MJ Hinton. 2004. Recommendations for designers and researchers resulting from the world-wide failure exercise. *Composites Science and Technology.* **64**: 589-604.

[69] SolidWorks: *Three-dimensional CAD software*, Dassault Systèmes, Concord MA, USA.

[70] Southas-Little RW. 1999. *Elasticity*, Dover Publications, INC., Mineola, NY, USA.

[71] Spearing SM and PWR Beaumont. 1992. Fatigue damage mechanics of composite materials. I: Experimental measurement of damage and post-fatigue properties. *Composites Science and Technology.* **44**: 159-168.

[72] Spearing SM and PWR Beaumont. 1992 Fatigue damage mechanics of composite materials. II: A damage growth model. *Composites Science and Technology.* **44**: 169-177.

[73] Spearing SM and PWR Beaumont. 1992 Fatigue damage mechanics of composite materials. IV: Prediction of post-fatigue stiffness. *Composites Science and Technology.* **44**: 309-377.

[74] Springer GS. 1981. Environmental effects on composite materials. *Technomic Publishing Company, Inc., Westport, USA.*

[75] Steven K, O Kevin, L Edmund, M Fionna and H Michael. 2007. Projections of primary and revision hip and knee arthroplasty in the united states from 2005 to 2030. *The Journal of Bone & Joint Surgery* **89**: 780–785.

[76] Stuart ML, 1990 *International encyclopedia of composites.* VCH Publishers.

[77] Sun CT, BJ Quinn and DW Oplinger. 1996. Comparative evaluation of failure analysis methods for composites laminates. *DOT/FAA/AR-95/109.*

[78] Suresh S. 2003. *Fatigue of materials*, Cambridge University Press, INC., New York, NY, USA.

[79] Synge JL. 1957. *The hypercircle in mathematical physics.* Cambridge University press, London.

[80] Thomas KF. 2006. *Private communications.* OrthoCarolina Hip and Knee Center, Charlotte, NC.

[81] Tianinen VM. 2001 Amorphous carbon as a bio-mechanical coating - mechanical properties and biological applications *Diamond and related Materials* **10**: 153–160.

[82] Tohgo K, ASD Wang, and TW Chou. 1993. A criterion for splitting crack initiation in unidirectional fiber-reinforced composites. *Journal of Composite Materials* **27**: 1054-1076.

[83] Tsai SW and EM Wu. 1971. A general theory of strength for anisotropic materials. *Journal of Composite Materials.* **5**: 58-80.

[84] Turner MJ, RW Clough, HC Martin and LJ Topp. 1956. Stiffness and deflection analysis of complex structures. *Journal of Aeronautical Sciences* **23**: 805-823.

[85] Turon A, CG Davila, PP Camanho, and J Costa. 2006. An engineering solution for mesh size effects in the simulation of delamination using cohesive zone models. *Engineering Fracture Mechanics* **74**: 1665-1682.

[86] Varna J and LA Berglund. 1991. Multiple transverse cracking and stiffness reduction in cross-ply laminates. *Journal of Composites Technology and Research* **13**: 97-106.

[87] Varna J and LA Berglund. 1992. A model for prediction of the transverse cracking strain in cross-ply laminates. *Journal of Reinforced Plastics and Composites* **11**: 708-728.

[88] Voyiadjis GZ and PI Kattan. 2005. *Damage mechanics*. Taylor & Francis group, LLC.

[89] Wang JS and Z Suo. 1990. Experimental determination of interfacial toughness using brazil-nut sandwich. *Acta Metallurgica.* **38**: 1279-1290.

[90] Wells GN, RD Borst and LJ Sluys. 2002 A consistent geometrically non-linear approach for delamination. *International Journal For Numerical Methods in Engineering.* **54** 1333-1355.

[91] Wisnom MR and FK Chang. 2000 Modelling of splitting and delamination in notched cross-ply laminates. *Composites Science and Technology.* **60**: 2849-2856.

[92] Yan Y, W-D Wen, F-K Chang and P Shyprykevich. 1999. Experimental study on clamping effects on the tensile strength of composite plates with a bolt-filled hole. *Composites* **30**: 1215-1229.

[93] Yang Q and B Cox. 2005. Cohesive models for damage evolution in laminated composites. *International Journal of Fracture.* **133**: 107-137.

[94] Yoshida H, A Faust, J Wilckens, M Kitagawa, J Fetto, YS Edmund and Chao. 2006. Three-dimensional dynamic hip contact area and pressure distribution during activities of daily living. *Journal of Biomechanics* **39**: 1996–2004.

[95] Young WC. 1989. *Roark's formulas for stress and strain*. McGraw-Hill Book Company.

[96] Zinoviv P, SV Grigoriev, OV Labedeva and LR Tairova. 1998. Strength of multilayered composites under plane stress state. *Composites Science and Technology.* **58**: 1225-1254.

[97] Zinoviv P, OV Labedeva and LR Tairova. 2002. Coupled analysis of experimental and theoretical results on the deformation and failure of laminated composites under a plane state of stress. *Composites Science and Technology.* **62**: 11711-11724.